universität wien

DISSERTATION

Titel der Dissertation

„Magnetism in 1D Metallic Clusters Grown Inside Single-Walled Carbon Nanotubes“

verfasst von

Juan Antonio Briones León

angestrebter akademischer Grad

Doktor der Naturwissenschaften (Dr. rer. nat.)

Wien, 2013

Studienkennzahl lt. Studienblatt:	A 791 411
Dissertationsgebiet lt. Studienblatt:	Physik
Betreuer:	Univ.-Prof. Mag. Dr. Thomas Pichler

Acknowledgements

First, I would like to thank Prof. Thomas Pichler for accepting me as a PhD student and supervise this PhD thesis in the Group of Electronic Properties of Materials of the Faculty of Physics at the University of Vienna.

This work would not be possible without the help and support of the members of the group and friends, special thanks to Prof. Hans Kuzmany, Prof. Paola Ayala, Dr. Christian Kramberger, Dr. Alexander Grüneis and Dr. Hide Shiozawa for their valuable inputs in physics, writing and presentations and also out of the academia.

Thanks to the technical staff, Stefan Loyer, Andreas Stangl and specially to the secretary of the group, Mrs. Eva Deutsch, their work is essential to keep everything working in optimal conditions.

Thanks to my colleagues and friends that make the life easier during the long working journeys. Special thanks to my fellow PhD students, Georgina Ruiz-Soria, Julio Chacon, Philip Rohringer, Markus Sauer and Lei Shi for sharing the stress during these years and for the nice talks during the lunch times.

The results reported here were possible thanks to the high quality samples provided and the characterization measurements of several collaborators. Thanks to Prof. Takeshi Saito, Prof. Hiromichi Kataura (AIST, Tsukuba) and Prof. Kazuhiro Yanagi (Tokyo Metropolitan University) for providing the high quality carbon nanotube samples. Thanks to Dr. Andreas Berger and Olatz Idigoras for providing the multilayer catalysts used in this work.

I am gratuful to Dr. Eugene Weschke and Dr. Enrico Schierle for sharing their extensive knowledge and for the technical assistance during the beamtimes at BESSY II. Thanks to Dr. Michael Eisterer and colleagues at the Atominstitut (TU Vienna) for their support during the use of SQUID magnetometer. TEM from Dr. Hua Jiang at the Nanomaterials group (Aalto University) is also highly appreciated. Thanks to Prof. Herwig Peterlik for the XRD measurements and helping in the analysis of the data.

I want to thank the financial supports from the Austrian Science Funds (FWF) and the 7th European Community's Framework Programme.

Finally, I will be always grateful with Alejandra Carranza and my two kids: Antonio Briones and Adriana Briones for the infinite support and patience along these years.

Kurzfassung

Kohlenstoffnanoröhren sind vielversprechende Bausteine für elektronische und magnetische Anwendungen in der Bio- und Materialtechnologie oder auch Spintronik. Eines der Herstellungsverfahren für Nanomagnete ist ausgerichtete einwandige Kohlenstoffnanoröhren (EWKNR) mit magnetischen Materialen zu befüllen.

Die vorliegende Arbeit vereint zu diesem Zweck zwei komplementäre Ansätze. Der eine behandelt die punkt genaue Herstellung von EWKNR durch lasergestützte chemische Gasphasenabscheidung (L-CGA). Der andere die magnetischen Eigenschaften von in EWKNR eingeschlossenen länglichen metallischen Nanopartikeln.

Im ersten Teil wurde Laserbestrahlung sowohl für die Herstellung von Kohlenstoffnanoröhren (KNR) als auch die Umwandlung von metallorganischen Verbindungen zu metallischen Nanopartikeln im Innern von EWKNR eingesetzt. Der Vergleich der verschiedenen eingesetzten Trägermaterialien und Katalysatorbeschichtungen zeigt deutlich den Einfluss der thermischen Leitfähigkeit auf die Wachstumszonen für amorphen Kohlestoff, mehrwandigen und einwandigen KNR. Das punktgenaue Wachsen von beliebigen Mustern aus KNR auf flachen Trägermaterialien ist eine Schlüsseltechnologie für die Realisierung von KNR Anwendungen. Dieser Ansatz zeigt auf, dass sehr schnelles und scharf begrenztes Wachstum von KNR mit Laserheizen realisierbar ist. Überdies sollte dieses Verfahren mit einer verfeinerten Parameteroptimierung auch für senkrecht stehende EWKNR anwendbar sein.

Im zweiten Teil wird der Magnetismus der länglichen metallischen Nanopartikel im Inneren von EWKNR mithilfe von zirkularen Röntgendichroismus (ZRC) und der supraleitenden Quanten-interferenzmethode (SQUIM) untersucht. Halbleitende oder metallische bzw. gemischte EWKNR wurden mit diversen metallorganischen Molekülen gefüllt. Durch Ausheizen wurden diese nanochemisch in innere KNR und längliche metallische Nanopartikel übergeführt.

Feldstärkeabhängige ZRC Messungen belegen dass sich der Magnetismus des eingeschlossenen Materials mit der Herausbildung der metallischen Nanopartikel grundlegend ändert. Magnetische Bahn und Spinmomente sind beide deutlich stärker in halbleitenden und schwächer in metallischen EWKNR. Dieser Effekt ist auf die unterschiedliche magnetische Suszeptibilität im Inneren von halbleiten und metallischen EWKNR zurück zu führen. Die Körnung der eingeschlossenen metallischen Nanopartikel wurde mittels klein Winkel Röntgen-streuung (kWRS) bestimmt. ZRC Messungen zeigen eine klare Korrelation zwischen Korngröße und dem magnetischen 3d Moment.

Diese Arbeit zeigt die Möglichkeiten die magnetischen Eigenschaften von länglichen metallischen Nanopartikeln im Inneren von EWKNR über den Füllgrad und die Ausheiz-bedingungen zu kontrollieren auf. Der Vergleich von lokalem Eisen 3d Magnetismus (ZRC) und dem makroskopischen Magnetismus (SQUIM) belegt das die magnetischen Eigenschaften der eingeschlossenen Metallpartikel von delokalisierten Beiträgen bestimmt sind.

Die gegenständliche Dissertation behandelt grundlegende Aspekte für das ferne Ziel der gezielten Herstellung von exakt definierten metallischen Nanopartikeln im Inneren von EWKNR.

Abstract

Carbon nanotubes have been proposed as building blocks to produce electronic and magnetic nanodevices for applications in bio- and material-technologies and spintronics. One approach to fabricate nanomagnets, is the controlled encapsulation of magnetic materials into aligned single-walled carbon nanotubes (SWCNTs).

For this purpose, two different studies have been done in this work. One involves the study of the synthesis of SWCNTs on predefined substrates by the laser-assisted chemical vapor deposition (LA-CVD) method. The other is the study of the magnetic properties of low-dimensional metallic clusters encapsulated in SWCNTs.

In the first part, continuous-wave (CW) laser irradiation has been used for both, the synthesis of carbon nanotubes (CNTs) and the transformation of organometallic compounds encapsulated in SWCNT to metallic clusters. Different catalysts and substrates have been used for the synthesis of CNTs by LA-CVD. The threshold between the growth of amorphous carbon, multi-walled carbon nanotubes (MWCNT) and SWCNT has been found to be very sensitive to the thermal conductivity of the chosen support or substrate. The local growth of patterned films of CNTs in flat substrates can facilitate the fabrication of CNT based devices. The proposed approach shows that the rapid and local synthesis of CNTs can be done by using a CW laser as heating source. However, further optimization of both the LA-CVD process and the multilayer catalyst conformation is needed to grow aligned SWCNTs.

In the second part, the magnetic properties of low-dimensional metallic clusters inside SWCNTs have been studied by means of x-ray magnetic circular dichroism (XMCD) and superconducting quantum interference device (SQUID). Metallicity sorted and mixed SWCNT samples have been filled with different organometallic compounds. Nanochemical reactions between the encapsulated molecules are induced by thermal annealing in vacuum to form inner tubes and metallic clusters.

Field dependant XMCD measurements reveal that the magnetic properties of the encapsulated compounds are altered drastically as the transformation to the 1D clusters takes place. The orbital and spin magnetic moments are both found to be larger in filled semiconducting nanotubes than in the metallic sample. This can be explained by the fact that the magnetic polarization of the encapsulated material depends on the metallicity of the tubes. The cluster size of the encapsulated materials has been determined by x-ray diffraction (XRD) measurements. The XMCD shows a relationship between the cluster size and the 3d magnetic moments.

This study shows a potential to tune the magnetic properties of low-dimensional metallic clusters encapsulated in SWCNTs by controlling the filling ratio and the annealing temperature. From a comparison between the iron 3d magnetic moments and the bulk magnetism measured by SQUID, it was concluded that the delocalized magnetism dictates the magnetic properties of these 1D hybrid nanostructures.

This work covers fundamental aspects for the long term goal of controlled growth of 1D metallic clusters inside aligned SWCNTs.

Contents

List of Figures

Motivation

Carbon nanotubes have exceptional structural and electronic properties. The application of carbon nanotube based nanodevices has been evinced in bio- and material-technologies as well as in spintronics. In order to use efficiently the carbon nanotube properties in future applications, a better understanding on the growth and functionalization of these hybrid materials is needed.

On one hand, the synthesis and structural manipulation of these nanostructures is still a challenge. Methods such as photolithography and laser assisted chemical vapor deposition have emerged as fair possibilities to grow nanostructures in a rapid and localized way. Specifically, laser assisted chemical vapor deposition, allows to directly write patterns of carbon nanotubes on flat surfaces, that could be used in the fabrication of nanotube based transistors or electrodes.

On the other hand, the functionalization of carbon nanotubes allows to modify the electronic and magnetic properties of these hybrid nanostructures in a controllable way. The intrinsic diamagnetism shown by pure carbon nanotubes can be changed to paramagnetism or superparamagnetism by controlling the particle size of metallic clusters encapsulated in the tubes. With this, two main goals emerge for this work. The first goal is to get a better understanding of the continuous-wave (CW) laser annealing process for both, the local growth of carbon nanostructures on predefined substrates, and for the local transformation of organometallic compounds encapsulated in single-walled carbon nanotubes.

The second goal is to understand the local magnetisms of encapsulated molecules inside single-walled carbon nanotubes. Organometallic compounds can be transformed to 1D metallic clusters encapsulated in the nanotubes, offering a way to control the magnetic properties of these hybrids.

The endohedral functionalization of patterned SWCNTs encapsulating metallic clusters emerge as a fair approach to build nanodevices in the near future.

Chapter 1

Introduction

1.1 Carbon nanotubes

Carbon is the base element of all organic materials. It has the unique property to form allotropes derived from three possible hybridizations: sp^3, sp^2 and sp. In compounds with sp^2 hybridization the electronic properties are mainly defined by the π electrons, while the mechanical properties are determined by the strong binding of the σ bonds. In 1985, fullerenes were discovered by Kroto et al. [1] followed with the first observations of carbon nanotubes (CNTs) by Iijima [2, 3]. With the discovery of these two low-dimensional allotropes of carbon, fascinating physical studies on these materials emerged and continue providing interesting possibilities for diverse applications.

Carbon nanotubes can be divided in two kind of structures. Multi-walled carbon nanotubes (MWCNT) are formed by concentric cylinders of graphene layers, with an interlayer spacing about 3.4 and diameters of the order of 5-20 nm [2]. The other type are single-walled carbon nanotubes (SWCNTs) considered as one-dimensional (1D) systems due to their high length/diameter ratio, with diameters in the order of 0.7-2.0 nm and lengths up to 4 cm [4].

In terms of mechanical properties, carbon nanotubes are predicted to be the strongest 1D structures that can be made [5, 6]. MWCNTs and SWCNTs have a very low weight and a very high elastic modulus. The Young's modulus of a SWCNT was determined experimentally to be about 1.25 TPa [7]. In contrast to other carbon fibers, carbon nanotubes are remarkably resilient to extreme strain with the ability to buckle in a reversible manner [8].

The electronic properties of carbon nanotubes are also remarkable. A SWCNT can behave as semiconductor or metal, depending on its diameter and chirality [9, 10]. Moreover, the energy gap in the semiconducting nanotubes can be changed by varying the nanotube diameter. These extraordinary nanostructures has been predicted as building blocks of electronic nanodevices [11]. In order to design such devices, a detailed knowledge of the electronic properties and the ability to modify them in a controlled way is crucial. In the case of SWCNT, the doping of the tubes to modify their electronic properties can be achieved by different means [12, 13].

The unique properties of carbon nanotubes have attracted the attention of many research groups in different fields. Theoretical and experimental studies has been focussing in the study of the relation between the nanotube structure and their electronic properties, as well as electron-electron and electron-phonon interactions [14, 15]. An extensive effort has been made in the understanding of these properties

and in exploring potential applications for these carbon nanostructures [16, 17].

In this chapter, a brief introduction to the structural, electronic and magnetic properties of carbon nanotubes is presented. A description of the functionalization of carbon nanotubes to modify their magnetic properties is also introduced. Some fragments of this introduction were extracted from the book of Saito, 2001 [18], the PhD thesis of Liu, 2003 [19] and the papers published in PSSB and PRB [20–22].

1.2 Structural and electronic properties of SWCNT

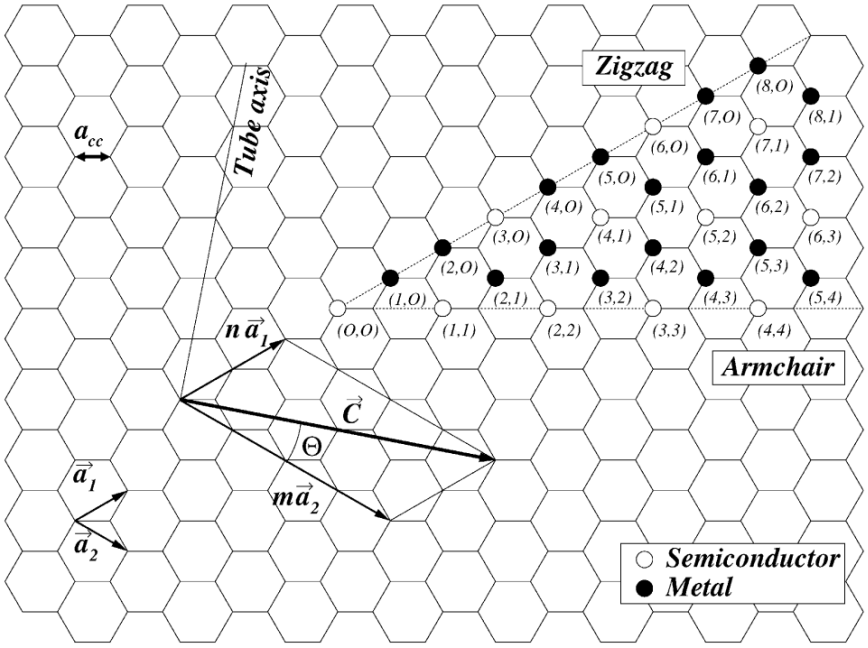

Figure 1.1: Carbon nanotubes are formed by rolling graphene sheets following a chiral vector **C** [23].

SWCNT are built as a rolled sheet of graphene into a seamless cylinder as is shown in figure 1.1. The wrapping vector or chiral vector **C** is defined as:

$$\mathbf{C} = n\mathbf{a_1} + m\mathbf{a_2} \tag{1.1}$$

where n and m are integers. The vectors $\mathbf{a_1}$ and $\mathbf{a_2}$ define the unit cell of the two dimensional graphene lattice. The vector perpendicular to the chiral vector **C** is the nanotube axis and is called translation vector **T**. The symbol a_{CC} is the nearest-neighbour C-C distance. The tubes are called "armchair" when $n = m$ and "zigzag" when $m = 0$. All the other tubes are called "chiral". The chiral angle θ corresponds to the angle between the chiral vector **C** and the zigzag axis.

The diameter of a (n, m) nanotube d_t is given by

$$d_t = |\mathbf{C}|/\pi = \sqrt{3}a_{CC}\left(n^2 + m^2 + nm\right)^{1/2}/\pi \tag{1.2}$$

The electronic properties of carbon nanotubes are derived from those for the rolled graphene sheet. In figure 1.2, the hexagonal lattice of a graphene sheet and its corresponding reciprocal lattice are shown.

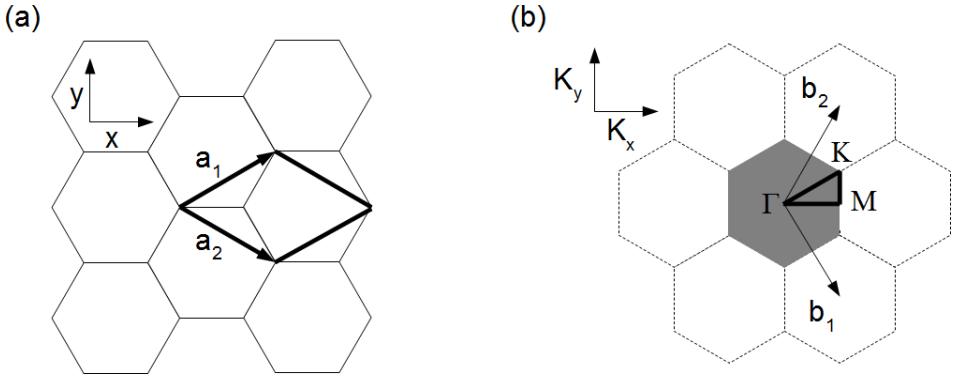

Figure 1.2: (a) Hexagonal lattice of a graphene sheet. The unit cell is defined by $\mathbf{a_1}$ and $\mathbf{a_2}$. (b) Reciprocal lattice with lattice vectors $\mathbf{b_1}$ and $\mathbf{b_2}$. The first Brillouin zone is indicated by the gray hexagon. The high symmetry points ΓKM are indicated by the black triangle.

The unit cell is defined by the rhombus formed by the vectors $\mathbf{a_1}$ and $\mathbf{a_2}$ in figure 1.2(a). The first Brillouin zone of a graphene sheet is shown as a grey hexagon in figure 1.2(b). The vectors $\mathbf{b_1}$ and $\mathbf{b_2}$ are the reciprocal lattice vectors. In the real space basis, vectors can be expressed as:

$$\mathbf{a_1} = \left(\sqrt{3}a/2, a/2\right) \quad \mathbf{a_2} = \left(\sqrt{3}a/2, -a/2\right) \tag{1.3}$$

The corresponding basis vector in the reciprocal lattice are given by:

$$\mathbf{b_1} = \left(2\pi\sqrt{3}a, 2\pi/a\right) \quad \mathbf{b_2} = \left(2\pi\sqrt{3}a, -2\pi/a\right) \tag{1.4}$$

with a lattice constant of $4\pi/\sqrt{3}a$ in reciprocal space. Three high symmetry points Γ, K and M, can be defined from the first Brillouin zone in the center, the corner and the center of the edge, respectively. The reciprocal vectors $\mathbf{K_1}$ and $\mathbf{K_2}$ correspond to the vectors $\mathbf{T}$ along the nanotube axis and $\mathbf{C}$ in the circumferential directions, respectively. The expressions for these vectors can be obtained from the relation $\mathbf{R_i} \cdot \mathbf{K_j} = 2\pi\delta_{ij}$, with $\mathbf{R_i}$ and $\mathbf{K_j}$ being the lattice vectors in the real and reciprocal space, respectively. As SWCNT are electronically a 1D structure, only $\mathbf{K_2}$ is the reciprocal lattice vector with a continuous value. The vector $\mathbf{K_1}$ gives discrete values in the direction of $\mathbf{C}$ due to the periodical boundary conditions. Therefore, the relations can be expressed as:

$$\mathbf{C} \cdot \mathbf{K_1} = 2\pi, \quad \mathbf{T} \cdot \mathbf{K_1} = 0; \quad \mathbf{C} \cdot \mathbf{K_2} = 0, \quad \mathbf{T} \cdot \mathbf{K_2} = 2\pi; \tag{1.5}$$

The expressions for $\mathbf{K_1}$ and $\mathbf{K_2}$ are obtained as followed:

$$\mathbf{K_1} = \left(-t_2\mathbf{b_1} + t_1\mathbf{b_2}\right)/N, \quad \mathbf{K_2} = \left(m\mathbf{b_1} - n\mathbf{b_2}\right)/N \tag{1.6}$$

The first Brillouin zone of an armchair tube (n, n) and a zigzag tube $(n, 0)$ are depicted in figure 1.3. The length of the segment lines is $\mathbf{K_2} = 2\pi/|\mathbf{T}|$, which is the length of the first Brillouin one. In the case of the armchair tube (n, n), figure 1.3(a), the length of all the parallel segment lines is $2\pi/a$, with $n + 1$ black lines in the shaded region. For the zigzag tube $(n, 0)$, figure 1.3(b), the 1D Brillouin zone consists of $n + 1$ black lines rotated by 30° with a length of $2\pi/\left(\sqrt{3}a\right)$. The separation of the segment lines is equal to $\mathbf{K_1}$.

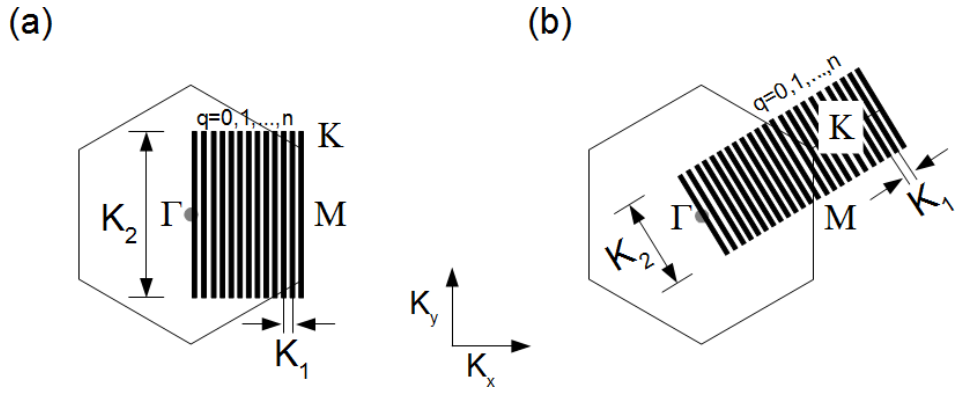

Figure 1.3: First Brillouin zone for (a) an armchair tube (n, n) and (b) a zigzag tube $(n, 0)$. The reciprocal lattice vectors $\mathbf{K_1}$ and $\mathbf{K_2}$ corresponding to the real space unit cell of these tubes as defined by $\mathbf{C}$ and $\mathbf{T}$, respectively. The periodic boundary conditions along the circumference of the tube results in the allowed $\mathbf{K_1}$ values as indicated vertical lines from $q = 0$ to n.

The electronic structure of carbon nanotubes can be calculated by a simple tight-binding approximation of the band structure of a graphene sheet. The number of states in the first Brilluin zone is given by $\left(|\mathbf{b_1} \times \mathbf{b_2}|\right)/(2\pi)^2 = 1/A_{cell}$, where A_{cell} is the area of the unit cell in real space. Each unit cell in the graphene sheet contains two carbon atoms and each carbon atom has four valence electrons. Three of these electrons form σ bonds with neighbouring atoms with a strong covalent interaction, the other forms the π-electron system which is related to the electron transport properties. From the tight-binding model, the dispersion of the π band of 2D graphite can be expressed as [15]:

$$E^{\pm}_{g2D}(k) = \frac{\varepsilon_{2p} \pm \gamma_0\omega(k)}{1 \pm s\omega(k)} \tag{1.7}$$

where γ_0 is the hopping integral, ε_{2p} is the site energy of the $2p$ atomic orbital and s denotes the overlap of the electronic wave function on adjacent sites. The $\pm$ signs in the numerator and denominator account for the anti-bonding π^* energy

band and the bonding π band, respectively. The wave function $\omega(k)$ is given by:

$$\omega(k) = \left\{ 1 + 4cos\left(\frac{\sqrt{3}k_x a}{2}\right) cos\left(\frac{k_y a}{2}\right) + 4cos^2\left(\frac{k_y a}{2}\right) \right\}^{1/2} \tag{1.8}$$

The energy dispersion relations of a 2D graphene are plotted as solid lines through the whole Brillouin zone in figure 1.4. In the right panel, the energy dispersion relation along the high symmetry axis along the perimeter of the triangle ΓKM are shown [24].

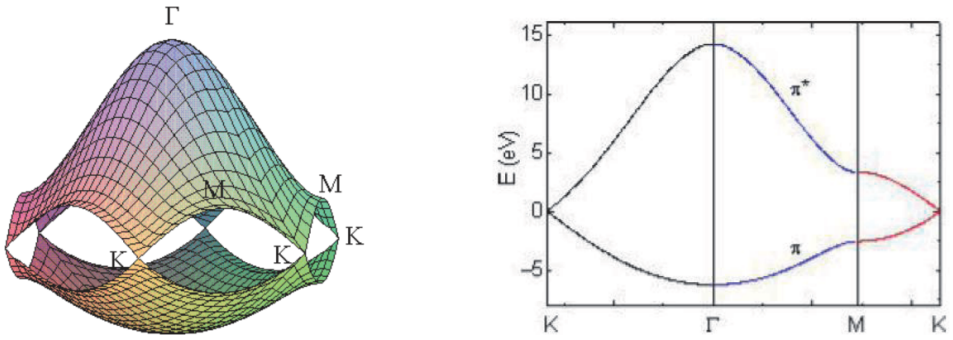

Figure 1.4: Energy dispersion relation of 2D graphene in the whole region of the Brillouin zone. The right panel shows the energy dispersion along the high symmetry directions of the triangle ΓMK [24].

The electronic structure of SWCNT is derived then from that of graphene, it is obtained that the reciprocal lattice is the parallel line along the tube axis separated by the defined value from the circumference. Then the energy bands consist of a set of 1D energy dispersion relations which are cross sections of those for a graphene sheet. Considering the reciprocal vector of a SWCNT and substituting into the energy dispersion of the graphite π band (equation 1.7) one obtains

$$E^{\pm}_{1D}(\mathbf{K}) = E^{\pm}_{g2D}\left(k\frac{\mathbf{K_2}}{|\mathbf{K_2}|} + \mu\mathbf{K_1}\right) \tag{1.9}$$

with $(\mu = 1, \ldots, N-1)$, and $\left(-\frac{\pi}{|\mathbf{T}|} < k < \frac{\pi}{|\mathbf{T}|}\right)$. Rewriting the equation above in terms of the x,y coordinate system, the obtained energy dispersion relation for a SWCNT is

$$E^{\pm}_{1D}(k) = \pm\gamma_0 \left\{ 1 + 4cos\left[\frac{\sqrt{3}a_0}{2}\left(k\frac{K_{2x}}{|\mathbf{K_2}|} + \mu K_{1x}\right)\right] cos\left[\frac{a_0}{2}\left(k\frac{K_{2y}}{|\mathbf{K_2}|} + \mu K_{1y}\right)\right] + 4cos^2\left[\frac{a_0}{2}\left(k\frac{K_{2y}}{|\mathbf{K_2}|} + \mu K_{1y}\right)\right] \right\}^{1/2} \tag{1.10}$$

Hence, the band structure of SWCNTs can be obtained from equation 1.10, considering the relation between the chirality (n, m) and the reciprocal vector $\mathbf{K}$.

The 1D density of states (DOS) in units of states/C-atom/eV can be then calculated as

$$D(E) = \frac{T}{2\pi N} \sum_{\pm} \sum_{\mu=1}^{N} \int \frac{1}{\left| \frac{dE_{\mu}^{\pm}(k)}{dk} \right|} \delta \left(E_{\mu}^{\pm}(k) - E \right) dE \tag{1.11}$$

where the summation is taken for the N conduction (+) and valence (-) 1D bands [18].

The calculated dispersion relation and DOS for an armchair (10,10) and a zigzag (17,0) nanotube is shown in figure 1.5. The metallic character of the armchair tubes is evident. When a cutting line passes through a K point of the 2D Brillouin zone the 1D energy bands have a zero-energy gap. In the case that the cutting line does not pass through a K point, then the SWCNT is semiconducting with a finite energy gap, that is the case of the zigzag (17,0) tube. Theoretical calculations have shown that all the armchair tubes have electronic bands crossing the Fermi level and are therefore metallic. In the case of the zigzag and the chiral tubes, exist two possibilities. When $n - m = 3l$ with l is an integer, the tubes are also metallic. If $n - m \neq 3l$ then the tubes are semiconducting with an energy gap inversely proportional to the nanotube diameter d_t [15].

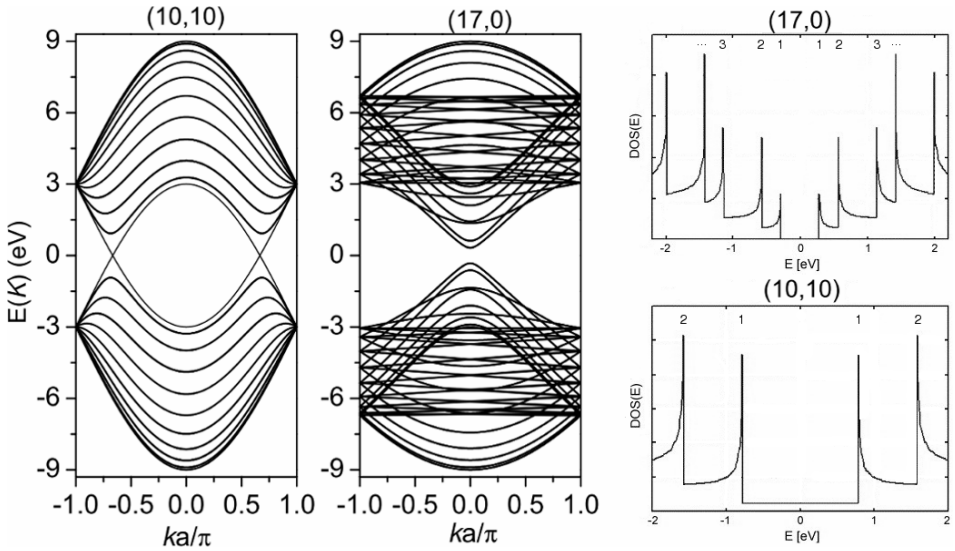

Figure 1.5: Dispersion relation (left) and DOS (right) for an armchair (10,10) and a zigzag (17,0) nanotubes. The numbers in the DOS indicate the van Hove singularities of the corresponding sub-bands [19].

The DOS of SWCNTs exhibits the typical van Hove singularities (vHs) of one dimensional systems, figure 1.5 right panel. When the band-structure on a cutting line pass through a local maximum or minimum, the denominator in the equation 1.11 vanishes and a spike occurs in the DOS. The energy differences $E_{11}^{M}(d_t)$ and

$E_{11}^{S}(d_t)$ for metallic and semiconducting nanotubes between the highest-lying valence band singularity and the lowest-lying conduction band singularity in the 1D electronic DOS can be expressed as follows [18]:

$$E_{11}^{M}(d_t) = 6a_C C\gamma_0/d_t \qquad E_{11}^{S}(d_t) = 2a_C C\gamma_0/d_t \tag{1.12}$$

Optical transitions are excitonic, where electron-hole interactions dominate. The transitions $E_{pp'}$ from the p-th valence band to the p'-th conduction band occurs in accordance with the selection rules of $\delta p = 0$ and $\delta p = \pm 1$ for parallel and perpendicular polarizations of the electric field with respect to the nanotube axis, respectively, where the number p=1,2,... denotes the order of the valence π and conduction π^* energy bands symmetrically located with respect to the Fermi energy. The same excitonic optical transitions are responsible for the very sensitive resonance Raman effect.

1.3 Synthesis of SWCNT

Real applications of carbon nanotubes require high yield and quality of the material produced. In this context, one of the most challenging topics regarding carbon nanotubes is the optimization of the production methods. Up to now, single-walled carbon nanotubes are produced by three main synthesis methods.

Arc discharge

In 1993, two independent research groups synthesize single-walled carbon nanotubes in an arc-discharge apparatus by co-evaporating of iron and cobalt metal catalysts in a methane atmosphere [3, 25]. Two graphitic electrods were used as electrodes, one of them containing traces of iron or cobalt that work as catalyst for the single-walled nanotubes. The majority of the SWCNT produced is bound together by van der Waals interaction and forms bundles of nanotubes. A later optimization of SWCNT growth by arc-discharge was achieved using a carbon anode containing 1.0 at.% of yttrium and 4.2 at.% of nickel as catalyst [26]. A maximal yield of about 50 wt % in the soot containing SWCNT can be obtained by this technique. The range of nanotube diameters produced by the arch-discharge method lies between 0.75 and 1.2 nm.

Laser ablation

The laser ablation method uses a laser to vaporize a graphitic rod mixed with a small amount of catalytic particles like Co or Ni in a high temperature furnace under an inert atmosphere. The soot produced deposits onto a water-cooled copper collector.

This method makes possible the production of 1 to 10 gram per day of high quality SWCNTs [27, 28]. The growth conditions are well controlled by the laser ablation technique, hence a variation of SWCNTs diameters can be reached by changing parameter as the furnace temperature, the gas carrier and the gas flow

rate. A maximal SWCNT yield up to 70 wt% could be achieved [29]. In this technique, the produced SWCNT are also self-organized into bundles of nanotubes with mean diameter and diameter distribution of about 1.2 ± 0.2 nm. The controlled growth of SWCNTs (diameter and chirality) by laser annealing has been achieved by using metal oxides as catalyst even at room temperatures [30].

Chemical vapor deposition (CVD)

The most popular synthesis method is the catalytic growth of carbon nanotubes by chemical vapor deposition (CVD) developed in 1993 [31]. The CVD techniques can provide the growth of both MWCNTs [32–34] and SWCNTs [35–39] individually. The CVD process involves passing a hydrocarbon vapor through a tubular reactor in which a catalyst material is present and heated at sufficiently temperature (600-1200°C) to decompose the hydrocarbon. A typical CVD set-up is depicted in figure 1.6.

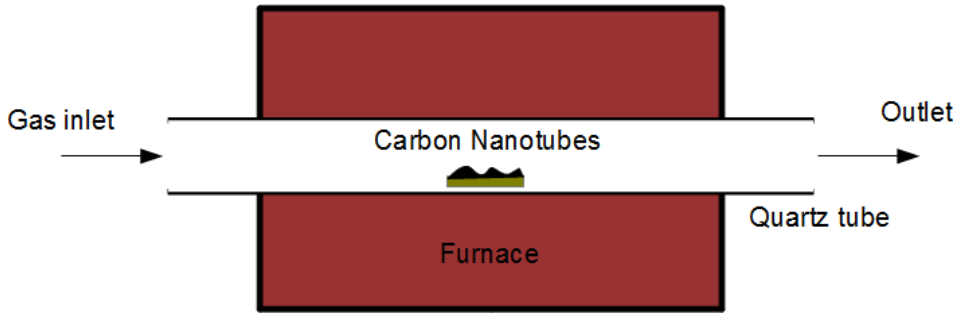

Figure 1.6: Schematic setup of the CVD technique.

The CVD technique provides a controllable medium to grow aligned and ordered nanotube structures on different surfaces. On the other side, changing any of these parameters leads to dramatic effects on the material produced. The temperature, the pressure, the gas-flow rate, the carbon source, the catalyst and the catalyst support are the key parameters to be controlled in order to enhance the synthesis of CNTs [40, 41]. An appropriate catalyst would preferentially grow single- rather than multi-walled carbon nanotubes [42]. Different carbon sources have been used in the CVD synthesis of carbon nanotubes: Carbon Monoxide (CO) [35, 43, 44], Methane (CH_4) [45], Ethylene (C_2H_4) [46], Acetylene (C_2H_2) [45, 47], Benzene (C_6H_6) [48], Toluene (C_7,H_8), Ethanol (C_2H_5OH) [49] and Methanol (CH_3OH). Each of these precursors has a specific decomposition temperature, therefore the nanotube growth temperature is different in the range of 650-900°C.

The use of alcohol as carbon source has been performed to grow high-purity SWCNTs at low temperatures (550°C) [50, 51]. The high-vacuum CVD (HV-CVD) has been used also to grow B-doped SWCNTs by using only one liquid precursor as source for both boron and carbon [52].

The pressure and the feed rate of the precursor during the CVD process also play an important role in the control of the material produced. The high pressure CO growth process (HiPCO) is a well known example of how the high pressure achieves a high yield of SWCNT with a very low amount of amorphous carbon [35]. A dependency of the catalytic particle size and the precursor feed rate has been studied in [53], where different carbon species were produced using different carbon carrier gas flow rates. A recent work, shows that the diameter distribution of SWCNTs can be selectively tuned by controlling the flow rate of a second carbon source during the synthesis procedure in the enhanced direct injection pyrolytic synthesis (eDIPS) process [54].

As catalysts, nanoparticles of Fe, Co, Mo, Ni, Cu, Au among others have been used either in pure metallic form or as alloys [55, 56]. The combination of the carbon source with the catalyst in a form of organometallic compounds (ferrocene or nickelocene) to grow CNTs has also been studied [57]. Another way of supported catalyst commonly used in CVD synthesis is by depositing thin metal films into a substrate via sputtering or thermal evaporation [58, 59]. By using these predefined substrates, the area of carbon nanotubes growth is limited to the surface where the catalyst has been deposited in the substrate. The use of thin layers of catalysts deposited in substrates has been extensively studied to grow vertically aligned CNTs [56, 58, 60, 61] controlling the diameter distribution [62] and the density of growth [63–66].

A strong dependency between the diameter distribution and the single- or multi-walled character of CNTs and the supporting material was proved for various substrates in [67]. The CVD synthesis using thin films of Al/Fe/Mo deposited on silicon has shown that SWCNT start to grow at 800°C [58]. In other work long length and high density of vertically aligned CNTs was achieved by using thin layers of Al/Fe deposited in SiO_2 [63]. The use of Ti as an adhesion promotion layer allowed the growth of CNT in various substrates improving the adhesion of the nanotubes to the substrate [65]. A direct comparison between CNTs growth in a Co layer and a multilayer catalyst (Co/Cr/Al) by CVD was reported in [68]. The yield, length and alignment of the nanotubes is dramatically improved by the use of multilayer catalyst by choosing the appropriate substrate.

Aligned SWCNT with a very good quality are synthesized in multilayer catalyst by choosing the right substrate, catalysts and temperature conditions [69–72]. Even at low temperatures (350°C) SWCNT can be synthesized by pre-treating in NH_3 or H_2 the multilayer catalyst to improve their catalytic activity [73]. A detailed study of the influence of the catalyst hydrogen pre-treatment in the synthesis of carbon nanotubes was shown in [74]. Other methods as the water-assisted synthesis of SWCNT has been reported to enhance the quality and the length of the grown nanotubes [46].

During the growth of carbon nanotubes, carbon diffuses towards the supported catalyst, in one of the two proposed growth mechanisms: base-growth or tip-growth mechanism [75]. In the case of the tip-growth model, figure 1.7, the interaction of the catalytic particle and the substrate is weak, so the carbon diffuses down

through the metal. The first steps depicted in figure 1.7(a-d) show the carbon diffusion precipitating in the form of CNT to the bottom later on (see figure 1.7(e-h)) pushing the catalytic particle off the substrate. Once the metal is covered with carbon, the catalytic activity stops and so the growth of the CNT.

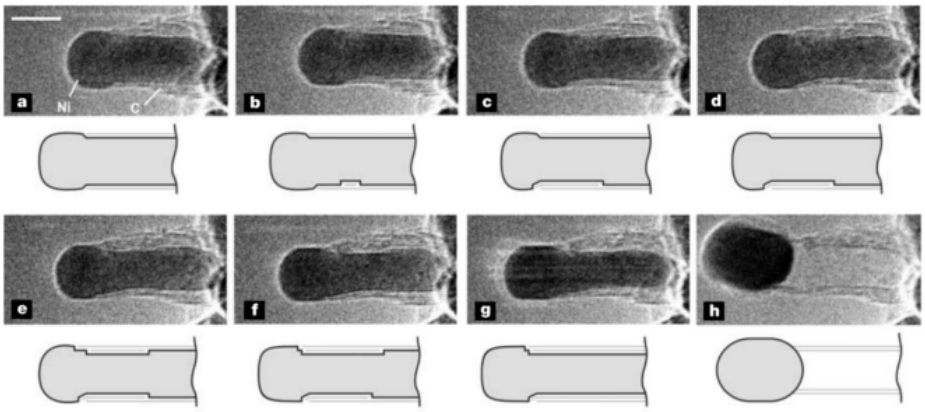

Figure 1.7: Schematic and TEM observations of the tip-growth model of SWCNTs [76]. The evolution of the growth process is labelled with the letters a-h.

When the interaction between catalyst and substrate is strong (more metal surface in contact with the substrate) figure 1.8(a), the precipitation of the carbon to the bottom fails to push the catalytic particle, so the precipitation emerge from the metal particle upwards in form of a spherical structure figure 1.8(b). The precipitation continues in a form of a cylinder to form the CNT, figure 1.8(c). This model is called base-growth model.

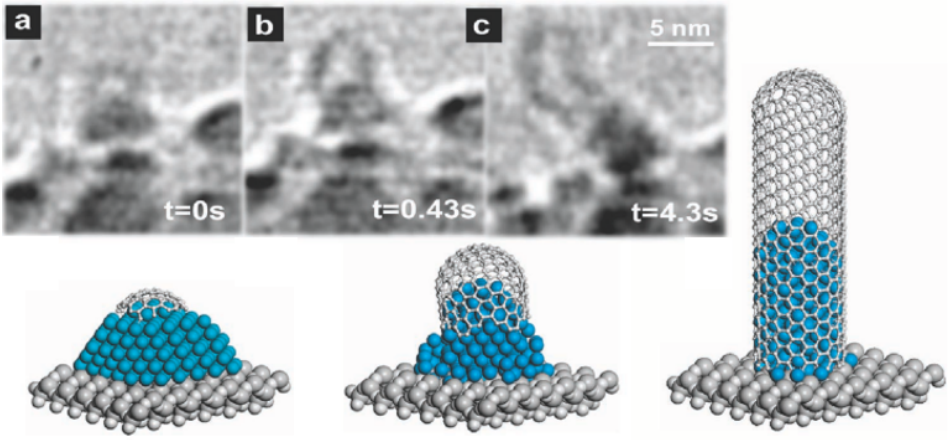

Figure 1.8: Schematic and TEM observations of the base-growth model of SWCNTs [77]. The evolution of the growth process is labeled with the letters a-c.

Both mechanisms have been observed during the synthesis of SWCNTs by transmission electron microscopy (TEM) [76–79] and have been confirmed by theoretical calculations [77, 78, 80].

1.4 Purification and metallicity separation of SWCNT

In the synthesis methods mentioned above, the produced carbon soot contains large amount of impurities, such as amorphous carbon, multi-shell carbon nanocapsules, graphite nanoparticles and metal catalyst particles. To remove this impurities, several purification methods of SWCNTs have been developed focussing in maintain the nanotube structure free of defects [81–84].

As was described above, the electronic and optical properties of carbon nanotubes depend on their diameter and chirality. Hence, their use is influenced by the possibility to separate them by metallicity or even more, by chirality.

In recent years great progress have been made to separate carbon nanotubes by diameter, bandgap and metallicity by different methods. The most prominent is density-gradient ultracentrifugation since 2006 [85]. Recent investigations, have shown upscaling possibilities using the efficiency of the gel-based techniques to separate SWCNTs in their metallic and semiconducting fractions [86]. The simple gel chromatography method was recently successfully applied to even separate SWCNTs in the single-chirality limit on a bulk scale [87].

1.5 Patterned growth of carbon nanotubes

Some attempts to use as-grown carbon nanotubes in electronic devices or as field emitters have been done by synthesizing pillars of SWCNT by the CVD method [33, 37, 89]. The preparation of the catalyst on the substrate for organized growth of CNTs is commonly done by photo-lithography, that combines several steps in a sequence. A photolithography process to grow CNT pillars on a substrate is shown in figure 1.9(a). First, a photo-resin pattern is deposited in the substrate, then a thin gold layer is deposited on the top. The photo-resin is removed by heating leaving circular areas of the substrate uncovered. The CNTs do not grow in the gold sites but in the uncovered substrate areas. Finally a CVD process in the substrate is performed to obtain the CNT pillars shown in figure 1.9(b).

Alternatively to photolithography, the use of a laser to localized heat the catalyst/substrate allows the synthesis of microscopic spots of CNTs [90–92] and even the direct writing of CNTs patterns as is shown in figure 1.10(c) [93, 94]. The use of the laser as heating source allows a fast and localized growth, where the nanotubes can grow in less than 10 seconds in spots smaller than 5 μm [93].

The first work of homogeneous films of MWCNT grown on a substrate using a CO_2 laser for local heating was reported in 2002 [90]. Later on, the synthesis of SWCNTs at a controlled position on a flat surface by the LA-CVD method was reported [93]. The use of an energy-confining layer in the composition of the multi-

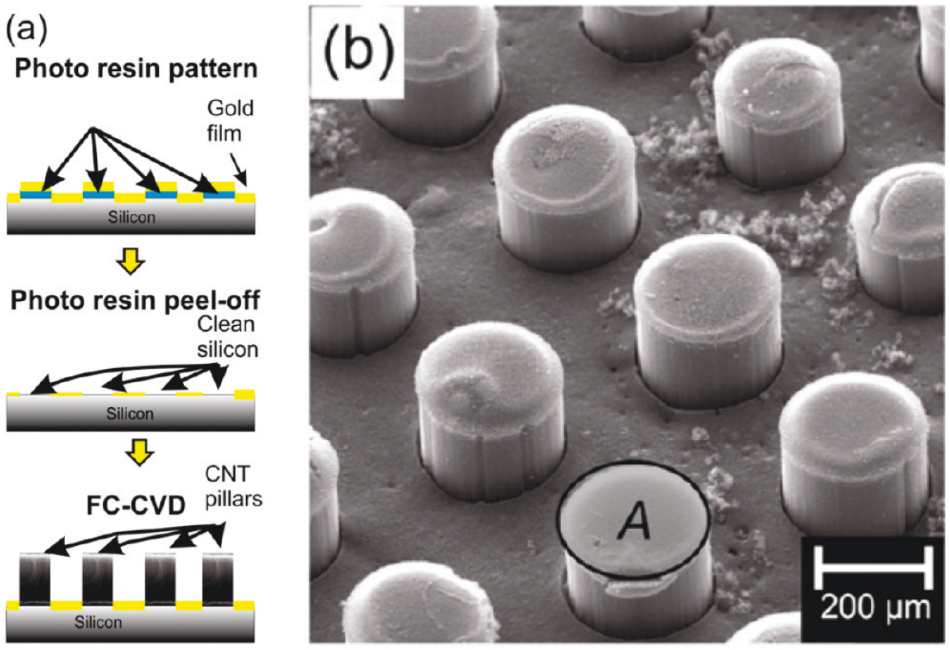

Figure 1.9: Schematic of the photolithography process (a) and SEM image (b) of pillars of CNTs. Adapted from [88].

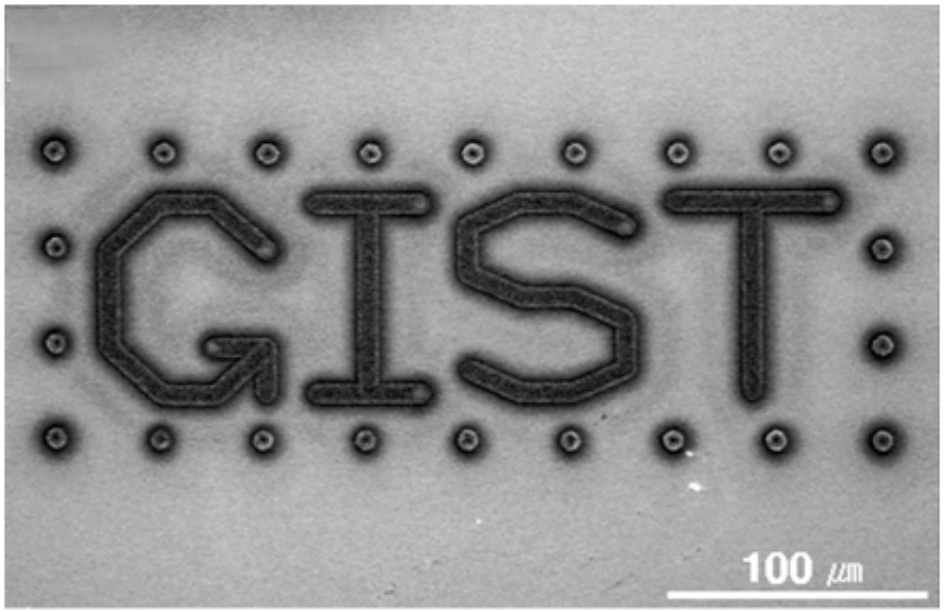

Figure 1.10: Direct writing of CNTs on flat surfaces. Adapted from [94].

layer catalyst avoids the dissipation of heating in the substrate. This improvement in the multilayer catalyst allows to directly write SWCNTs on a flat surface. In a better controlled process the direct writing of MWCNTs on a substrate has been reported [94]. In a recent work, *in-situ* Raman and reflection spectroscopy have been applied to study the growth phases of CNTs by LA-CVD [91].

A more sophisticated method was used recently to control the growth of SWCNT in a multilayer substrate [92]. A closed-loop control has been implemented by measuring the reflected laser light and the thermal radiation from the substrate during the synthesis process. The local growth of CNTs by LA-CVD gives the possibility for the fabrication of nanodevices based on carbon nanostructures [95].

1.6 Functionalization and nanochemical reactions inside SWCNT

As was introduced above, carbon nanotubes have unique structural and electronic properties, reason to consider them as promising building blocks for molecular electronics [96]. The future application of these 1D nanostructures depend largely on the ability to modify their intrinsic properties by manipulating their electronic structure. In order to change these properties in a controlled way, CNTs can be functionalized by adding molecules or compounds in different ways [97–102].

The functionalization of SWCNTs can be generally classified in two: chemical and physical functionalization [97, 102]. Chemical functionalization methods are based on the covalent linkage of functional groups on the surface of the SWCNTs. This is the case of the sidewall functionalization and the defect sidewall functionalization, figure 1.11(a) and (b), respectively [98, 101, 103–105]. In the physical functionalization methods non-covalent interactions are formed between the molecules and the SWCNT. These methods include the wrapping of polymer around CNTs [106, 107], the physical adsorption of surfactants and the endohedral functionalization [108, 109], figure 1.11(c), (d) and (e), respectively.

Endohedral functionalization or filling of carbon nanostructures with molecules (figure 1.11b) has become promising in order to change or even control the electronic and magnetic properties of these hybrid nanostructures [109]. Since the first observation of peapods, i.e., SWCNT accommodating buckminster fullerenes [108], various molecules and compounds including metallocenes and salts have been encapsulated in the hollow core of CNTs [110–120]. Encapsulated in CNTs, the filling material is protected against oxidation by the rolled up graphene layer. Suggested applications of such materials are magneto recording devices [121] and nanoscale thermometer for biological purposes [122].

In recent years, metallocene filled and especially ferrocene ($FeCp_2$) filled carbon nanotubes ($FeCp_2$@SWCNT) have been widely studied. Two filling methods have been proposed. First, the vapor phase method, which gets a better filling ratio than the second: a solvent-based method. However, the solvent-based method is faster and enables a quick analysis of this material [123].

The electronic properties of carbon nanotubes can be modified via filling followed by the transformation of the molecules inside into inner tubes and metal clusters [117, 124] utilizing a nanochemical reaction. By the decomposition of the $FeCp_2$ inside the nanotubes, encapsulated Fe nanowire can be formed. Such Fe@SWCNT were reported to show a higher magnetization than the $FeCp_2$@SWCNT and the pristine SWCNT, and exhibit both ferromagnetism and superparamagnetism at different temperatures [116].

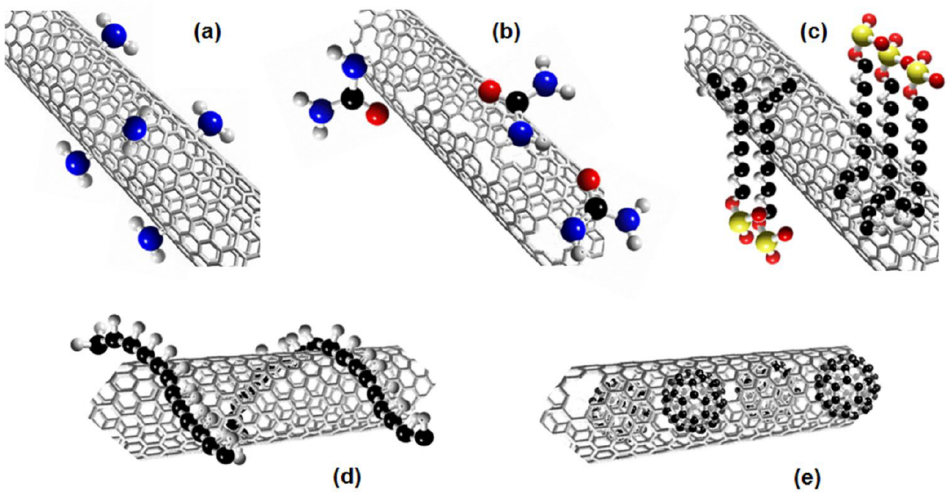

Figure 1.11: Functionalization possibilities for SWCNTs. (a) covalent sidewall functionalization, (b) covalent defect sidewall functionalization, (c) non-covalent adsorption of surfactants, (d) wrapping of polymers, and (e) endohedral functionalization (C_{60} peapods) [102].

Filled single-walled carbon nanotubes (SWCNT) can be used as nanoreactors to grow new materials at the nanoscale [125]. The transformation from filled SWCNT to double-walled carbon nanotubes (DWCNT) was shown first from C_{60} inside the SWCNT [126]. It was also found that C_{70} forms small diameter inner tubes as well as C_{60}@SWCNT [127]. The use of encapsulated ferrocene inside SWCNT as catalyst to synthesize DWCNT in a controllable way was also proposed in [128]. Using $FeCp_2$ inside the tubes, it is more likely to fill and transform SWCNT of smaller diameters than using C_{60}@SWCNT [129]. While the $FeCp_2$ decomposes inside the SWCNT to form inner tubes, the iron remains inside and it could be removed in a controllable way by an annealing process [117].

DWCNTs have been obtained by the laser annealing of C_{60} encapsulated in SWCNT (C_{60} peapods). The induced heating by laser results in a quicker transformation of the encapsulated C_{60} molecules into DWCNTs in comparison with the conventional furnace annealing [130]. The site selective heating to anneal small sample batches and the fast transformation of the ferrocene inside the SWCNT to inner tubes are two remarkable advantages of laser annealing process.

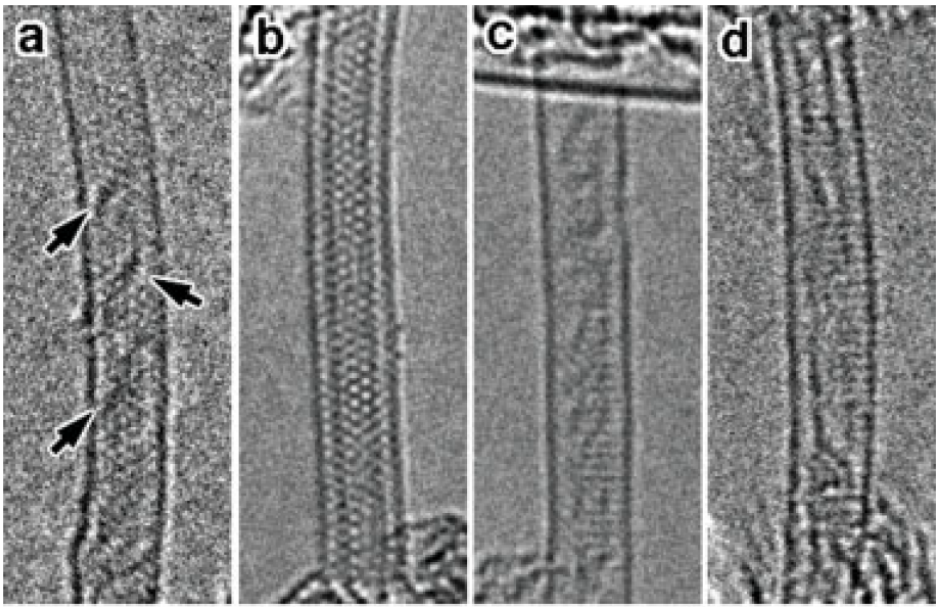

Figure 1.12: TEM migrographs of (a) ferrocene filled SWCNT. After annealing the filled nanotubes to 1150°C for one hour (b) the encapsulated molecule is transformed completely to inner tubes. Annealing at 600°C for two hrs (c,d), transform partially the encapsulated molecules to inner tubes obtaining also metal clusters. Adapted from [117].

1.7 Magnetism in SWCNT and in 1D metals encapsulated in SWCNT

The magnetic properties of SWCNT are highly anisotropic due to their unique 1D character. The diamagnetic nature of CNTs was predicted theoretically for semiconducting and metallic tubes [131]. One year later this prediction was proved experimentally [132, 133]. The electronic band structure of SWCNTs is altered differently at applied magnetic fields parallel or perpendicular to the tube axis, leading to novel magnetic, magneto-transport and magneto-optical properties [134].

However many previous studies show a nonconclusive behavior. Some of them show that CNTs synthesized by using catalytic particles, e.g. Fe, Ni or Co, show a ferromagnetic behavior while CNTs grown without catalytic particles are diamagnetic [121, 135–141]. A detailed study of magnetic properties of the so-called HiPCO nanotubes show a superparamagnetic behavior, which was attributed to the remaining catalytic particles encapsulated in the tubes [142]. The same is most likely the case for the use of other magnetic catalytic particles. Therefore, only the use of very pure SWCNT material will solve this discrepancy and allow to study their intrinsic magnetic properties.

In addition a ferromagnetic behaviour was observed in Fe encapsulated in SWCNT

even at room temperature, as a result of the large quantity of Fe, filling the hollow of the tubes, and the interaction between the Fe nanowires in the bundles of SWCNT [143]. Figure 1.13 shows the magnetization curves of carbon nanotubes grown using Fe as catalyst [138]. The as-grown carbon nanotubes show the typical hysteresis loop of a ferromagnetic material. This behavior is governed by the remaining Fe particles, figure 1.13(a). When the Fe-based carbon nanotubes are annealed at high temperatures, most of the remaining catalytic particles are removed from the nanotubes. A diamagnetic behavior is then obtained for the nanotubes after the annealing process, figure 1.13(b).

In a theoretical study of the local magnetic moment of Fe nanowires encapsulated in SWCNT, a dependency on the size of the Fe nanoparticles was found, due to the interaction between the particle and the nanotube [144]. The encapsulation of Fe in SWCNT strongly alters the spin magnetic moment and the magnitude of magnetic anisotropy energy [145].

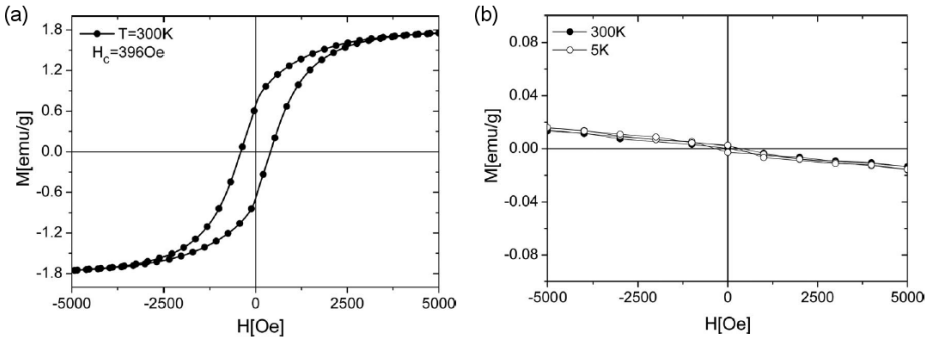

Figure 1.13: Magnetization curves of Fe-based carbon nanotubes (a) as-grown with a hysteresis loop governed by the remaining Fe particles, (b) after annealing in argon atmosphere at 2500°C with a diamagnetic behavior. Adapted from [138].

It is evident that the remaining catalytic particles alter considerably the magnetic properties of SWCNTs. Nevertheless, the possibility to control the amount or size of the encapsulated metal clusters, allows the magnetic properties of these hybrid nanostructures to be tuned.

As described in the previous section, structural and electronic properties of SWCNTs can be controllably modified by functionalization. Particularly, endohedral functionalization or filling of carbon nanostructures with different organometallic compounds has become a promising means to change the magnetic properties [109]. One attempt to alter the magnetic properties of carbon nanotubes, is via the filling of SWCNT with endohedral metallofullerenes [146]. Significant changes in magnetic moment of SWCNT encapsulating metallofullerenes ($Gd@C_{82}$ and $Dy@C_{82}$) were found at low temperature (10 K), attributed to the charge transfer from the metallofullerene to the SWCNT [114, 147]. In addition, SWCNT filled with magnetic salts such as $ErCl_3$ have been studied. The magnetization of purified empty SWCNT

were measured and found to be much lower than in $ErCl_3$ nanowires grown inside SWCNT where the magnetization values are the same as the ones of bulk anhydrous $ErCl_3$ [115, 148].

Regarding the magnetic properties of metallocene filled and especially ferrocene filled carbon nanotubes ($FeCp_2$@SWCNT) as mentioned above, their electronic properties can be modified via filling followed by nanochemical reactions that transforms the molecules into inner tubes and cementite clusters [117, 124]. After the decomposition of the $FeCp_2$ inside the nanotubes, encapsulated cementite nanowires can be formed. Such Fe_3C@SWCNT were reported to show a higher magnetization than the $FeCp_2$@SWCNT and the pristine SWCNT, and exhibit both ferromagnetism and paramagnetism at different temperatures in some preliminary studies [116]. However, the magnetic properties of ultra pure metallicity sorted SWCNT and Hipco and e-Dips SWCNT after ferrocene filling and nanochemical reactions is still unknown and will be studied in detail in this thesis.

Chapter 2

Experimental Methods

2.1 Introduction to characterization methods

In this work, several carbon nanotubes samples were synthesized and/or endohedrally functionalized with different organometallic compounds.

Raman spectroscopy, scanning electron miscroscopy (SEM), and x-ray diffraction (XRD) were used to structurally characterize the nanotubes before and after their functionalization. Superconducting quantum interference device (SQUID) and X-ray magnetic circular dichroism (XMCD) techniques were used to characterize the magnetic properties of the filled nanotubes.

In this chapter, a description of the methods and techniques to synthesize, functionalize and characterize the carbon nanotubes samples is presented.

2.1.1 Raman spectroscopy

Raman spectroscopy is based on the analysis of inelastically scattered light, where scattering from optical modes of quasi-particles (mainly phonons) occurs. A phonon contributes to the Raman process when it induces a change in the polarizability.

More details of the Raman theory can be found in the book of Kuzmany, 2009 [149]. The use of Raman spectroscopy to characterize carbon nanotubes has being widely studied. In this section we refer to the books [15, 150].

When a monochromatic light hits an obstacle (solid, liquid or gas), part of this light is elastically scattered (Rayleigh scattering) and a small fraction of it is inelastically scattered (Raman scattering). An schematic of the elastic and inelastic scattering process is shown in figure 2.1. The difference in energy between the incident ($\hbar\nu$) and the scattered photons ($\hbar\omega$), in the Raman scattering process, corresponds to the vibrational frequencies of the scattering medium ($\hbar\nu \pm \hbar\omega$). Is called Stokes radiation when the photon is scattered to a lower energy, i.e. the energy transfer from the photon to the molecule or solid ($\hbar\nu - \hbar\omega$). In Anti-Stokes radiation the energy is transferred from the molecule or solid to the photon, so the photon is scattered to a higher energy ($\hbar\nu + \hbar\omega$). As the population of states at room temperature is in its ground vibrational state, the Stokes process is stronger than the Anti-Stokes.

Resonance Raman spectroscopy

The probability of the Raman scattering process is very low (in the order of one photon over 10^7 incident photons), because it involves an excitation to a virtual

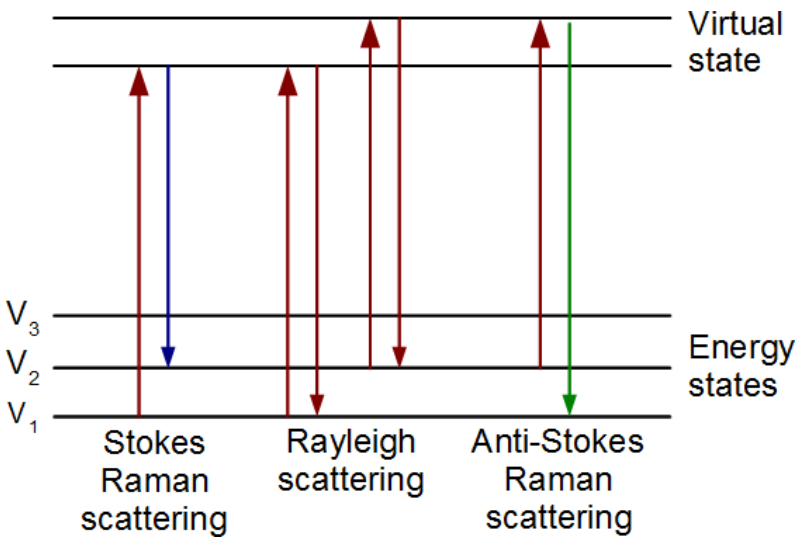

Figure 2.1: Schematic representation of the elastic (Rayleigh) and inelastic (Stokes Raman and Anti-Stokes Raman) scattering processes

.

level that is only allowed for a very short time, in the context of the uncertainty principle. This probability is increased if the transition energy for either the absorbed or the emitted photon coincides with an electronic transition energy of the molecule. The observation of this process is called resonant Raman spectroscopy. In the case of SWCNT, the cross section for a resonant Raman process is large enough to analyse vibrational modes of an individual tube. Furthermore, the Raman signals detected for different excitation energies can e used to identify SWCNTs with different chiralities at resonance.

This technique is commonly used to characterize SWCNTs due to its high sensibility without requiring an special preparation of the sample. A general view of a Raman spectrum of SWCNT is depicted in figure 2.2, where the Raman shift (i.e. the shift with respect to the excitation light wavenumber) is expressed in wavenumber units of cm^{-1}.

G-band

The dominant peak at $\sim$1590 cm^{-1} is associated with the in-plane tangential optical phonon that involves the stretching of the bond between the two atoms in the graphene unit cell [151]. This band, is referred to as the graphite-like band or G-band. The G-band of SWCNTs splits into a lower energy (G^-) peak and a higher energy (G^+) peak. This splitting is caused by the curvature of SWCNTs, which induces an energy difference between the axial and transverse in-plan vibrational modes. The G^- feature at 1570 cm^{-1} is associated with carbon atom vibrations along the circumferential direction of the nanotube and it is sensitive to the metallicity of the tube. In comparison to the G^-, the feature at 1590 cm^{-1} does not

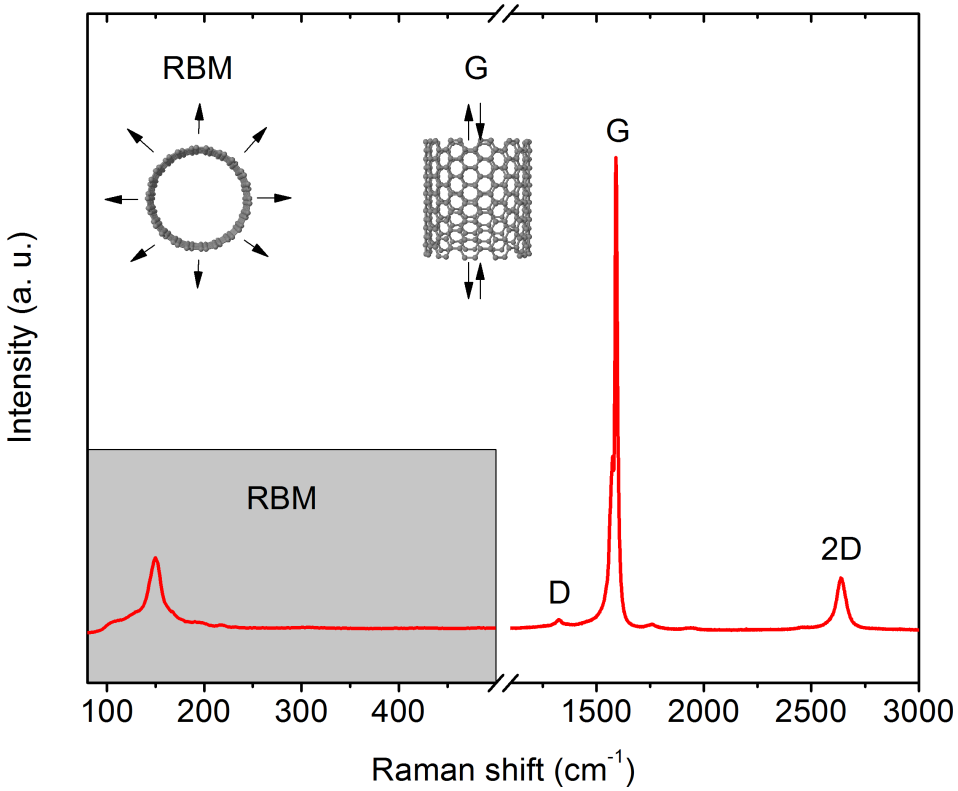

Figure 2.2: Typical Raman spectra of SWCNT. The vibrations along the circumferential direction of the nanotube correspond to the G-band. The oscillations of the nanotube diameter correpond to the RBM with frequencies 120-400 cm^{-1} (gray area). The D- and 2D-modes are related with second-order scattering events.

depend on the nanotube diameter and chiral angle. The G^+ feature is associated to carbon atom vibrations along the nanotube axis and is sensitive to the charge transfer between dopants and the SWCNT. The scattering process associated with the G band excitation ia a first-order process, i.e. only one scattering event occurs.

D- and 2D-band

The D-band is a longitudinal optical (LO) phonon and is known as the disordered or defect mode because a defect is required to elastically scatter in order for the process to conserve momentum. The D-band appears as a small peak at ~1355 cm^{-1}. Is well known that this position depends on the laser excitation wavelength due to the double resonance mechanism [152]. This band is observed when a symmetry breaking on the hexagonal sp^2-bonding lattices is observed. A conventional way to quantify the structural quality of carbon nanotubes by Raman spectrosocpy is by the D/G intensity ratio. When the material is defective, the D-band is observed larger and broader with a large D/G ratio. A detailed analysis of the D-band can be also used to study doping of CNTs and the tube-length shortening [150].

A second harmonic of the D-band occurs at ∼2700 cm^{-1} and is called 2D-band. This feature is sensitive to nanotube defects, but more information of the electronic structure of SWCNTs can be obtained by its study.

RBM

The Raman features at low frequencies (between 120-400 cm^{-1}) correspond to a phonon excitation that is unique to SWCNTs. An out-of-plane mode exists due to the vibrations perpendicular to the lattice plane where these vibrations are oriented radially away from the SWCNTs axis. This radial mode is result of the oscillations of the diameter of the entire SWCNT, appearing as though it was "breathing". This mode is know as the radial breathing mode or RBM. The Raman intensity of the RBM is strongly enhanced when the incident photon is in resonance with the energy gap E_{ii} of a SWCNT. Theoretical and experimental studies show that the RBM frequency ω_{RBM} is inversely proportional to the nanotube diameter d_t through the relation $\omega_{RBM} = 217.8/d_t + 15.7$ [153].

Because of its dependence on the nanotube diameter, the spectrum of this mode is largely used to characterize the diameter properties of SWCNTs. By collecting the Raman spectra measured by manny different laser lines, a good approach to the diameter distribution of the SWCNT can be obtained. Furthermore, when referring to the Kataura plot (figure 2.3), it is feasible to assign the RBMs to specific chiralities of SWCNTs. Each point in the Kataura plot represents one optical transition energy E_{ii} for a specific (n,m), calculated theoretically, as a function of the diameter of the tube, d_t (top horizontal axis). The bottom horizontal axis indicates the radial breathing mode frequency, ω_{RBM} [154].

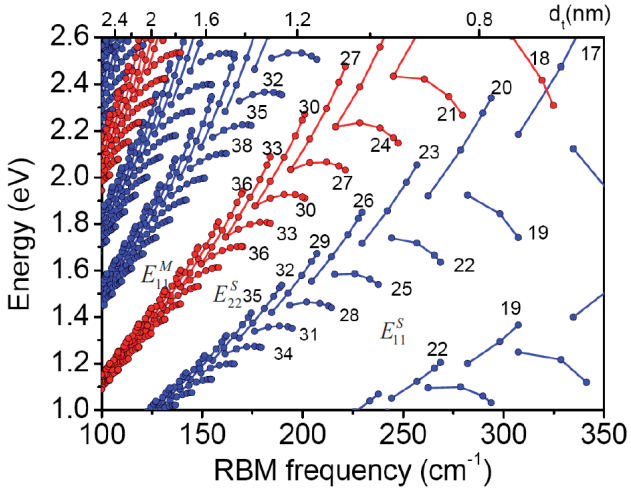

Figure 2.3: Values of optical transition energy E_{ii} as calculated theoretically for semiconducting (blue dots) and metallic (red dots) nanotubes vs. radial breathing mode frequency ω_{RBM} and nanotube diameter d_t. The 2n+m = constant families are joined by solid lines.

2.1.2 X-ray Magnetic Circular Dichroism

Some fragments of this section were extracted from references [155, 156].

The XMCD can be classified as a magneto-optical effect that relates the spectroscopic and optical properties to the magnetic state of a system. The first prediction of magneto-optical effects in x-ray absorption using circularly polarized light were done by Erskine and Stern in 1975 [157].

The possibility to measure XMCD emerged several years later with the development of synchrotron radiation sources providing a continuous spectrum of polarized x-rays with a high photon flux. The first experimental proof of XMCD measurements of a Fe foil at the K edge was done by Shütz et al. in 1987 [158].

This method is element-selective, i.e. the measurements can be carried out at different edges (K, $L_{2,3}$, $M_{4,5}$) providing information on the magnetic states of the sample.

XMCD Process

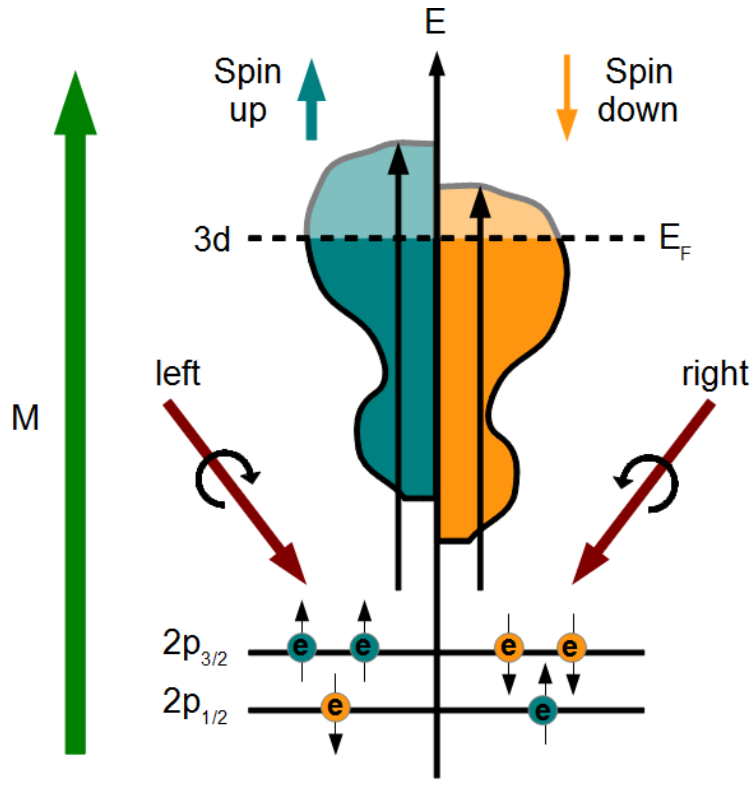

Figure 2.4: Schematic representation of the x-ray magnetic circular dichroism process at the $L_{2,3}$ edges of a 3d transition metal.

The description of the XMCD principle is depicted in figure 2.4. In the first step, the photoelectrons are excited from their initial states. Spin-polarized photoelectrons are created via the spin-orbit coupling in the initial states by using circularly

polarized light. Right and left circularly polarized photons transfer the opposite momentum to the electron. Then, the spin polarization at the L_3 and L_2 edges will be opposite due to the opposite spin-orbit coupling, $j = l + s$ for the L_3 edge and $j = l - s$ for the L_2 edge. The spin up and spin down character is defined relative to the photon helicity which is parallel (right) or antiparallel (left) to the x-ray propagation direction.

In the second step, the 3d valence band act as a spin-detector of the spin-polarized excited photoelectrons. Aligning the direction of the magnetization M with the photon-spin direction a maximum dichroism effect is obtained. The occupation of the spin up or spin down states will depends on the alignment of the magnetization parallel or antiparallel with respect to the x-ray propagation direction. Hence, the absorption of left-circularly polarized x-rays will be enhanced at the L_3 edge and reduced at the L_2 edge with respect to the exchange-splitted 3d states. The opposite effect is expected for right circularly polarized light. The x-ray magnetic circular dichroism is defined as the difference between the absorption of right and left circularly polarized x-rays with M parallel to the x-ray propagation direction, equation 2.1.

$$\triangle \mu(E) = \mu^{+}(E) - \mu^{-}(E) \tag{2.1}$$

An example of experimental x-ray absorption spectra (XAS) of right and left circularly polarized light and the corresponding magnetic circular dichroism (XMCD) is shown in figure 2.5. By changing the direction of the magnetization M instead of the helicity of the light produces the same effect on the x-ray absorption and therefore, on the magnetic circular dichroism.

XMCD Sum Rules

The XMCD sum rules were introduced for the first time by Thole et al. in 1992 [159] and Carra et al. in 1993 [160]. These sum rules state that integrations of the XMCD and the total XAS are related directly to the ground-state orbital (m_L) and spin (m_S) magnetic moments.

The ground-state expectation value of the orbital angular momentum per hole is given by:

$$\langle L_z \rangle = 2n_h \frac{\int_{j^+ + j^-} dE(\mu^+ - \mu^-)}{\int_{j^+ + j^-} dE(\mu^+ + \mu^- + \mu^0)} \tag{2.2}$$

The ground-state expectation value of the spin-dependant part of the local magnetic field per hole is given by:

$$\langle 2S_z \rangle + 7\langle T_z \rangle = 3n_h \left\{ \frac{\int_{j^+} dE(\mu^+ - \mu^-) - 2\int_{j^-} dE(\mu^+ - \mu^-)}{\int_{j^+ + j^-} dE(\mu^+ + \mu^- + \mu^0)} \right\} \tag{2.3}$$

Where n_h is the number of 3d holes and it is taken from theory [161]. The term $\mu^0 = (\mu^+ + \mu^-)/2$ is the average of the two polarizations. The expectation value of

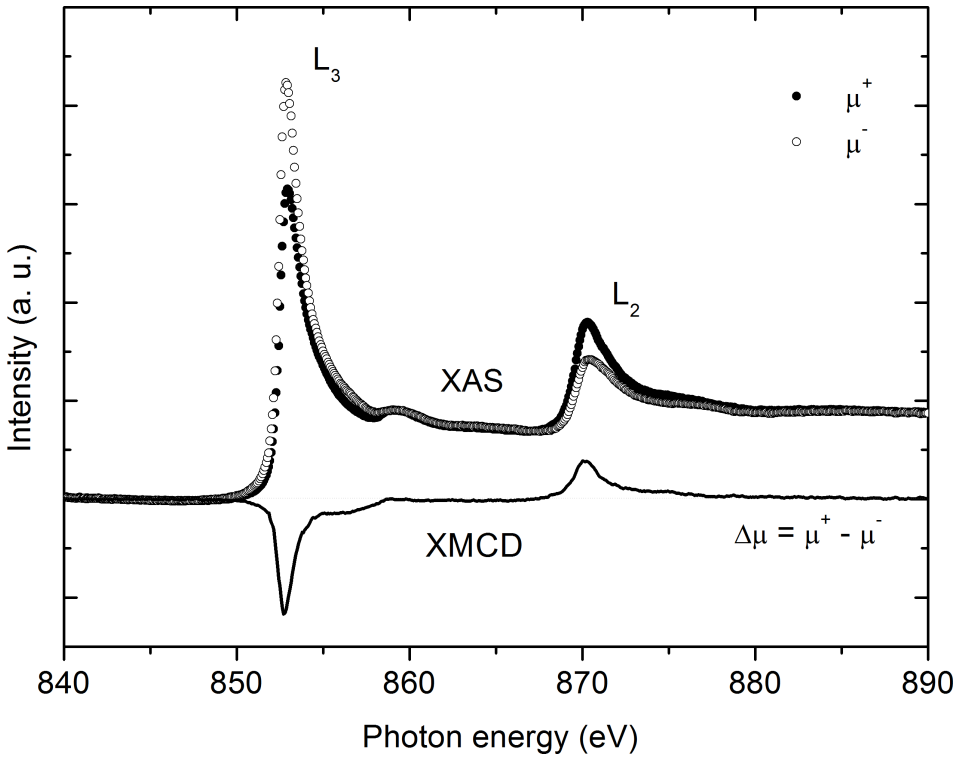

Figure 2.5: Experimental Ni $L_{2,3}$ XAS for right (empty dots) and left (solid dots) circularly polarized light. The corresponding XMCD is shown in a solid line.

the magnetic dipole operator $\langle T_z \rangle$ provides a measure of the anisotropy of the field of the spins, either by the spin-orbit interaction or by crystal-field effects. In the case of transition metals, the contribution of this term is lower than 10% of the spin magnetic moment [160, 162, 163], so can be neglected without affecting our analysis.

Finally, the orbital and spin magnetic moments are calculated by $m_L = -\langle L_z \rangle$ and $m_S = -2\langle S_z \rangle$, respectively.

Analysis of the Experimental Data

In order to use the sum rules it is necessary to remove the contribution of photoelectron excitations into continuum states from the absorption cross section. A convolution of a two-step and a Voigt function was adopted to remove the L_3 and the L_2 edge jumps. The height of the L_3 (2/3) and L_2 (1/3) steps was set according to its quantum degeneracy $(2j + 1)$ as was described in [164]. The XAS spectra, the two-step function and the integration of the XAS spectra after removal of the L_3 and L_2 edge jumps are shown in figure 2.6-a. The limit of the XAS integration is taken at r. The XMCD and its corresponding integration is show in figure 2.6-b. The limits of integration terms $\int_{j+} dE(\mu^+ - \mu^-)$ and $\int_{j-} dE(\mu^+ - \mu^-)$ in equations 2.2 and 2.3 are defined with letters p and q, respectively.

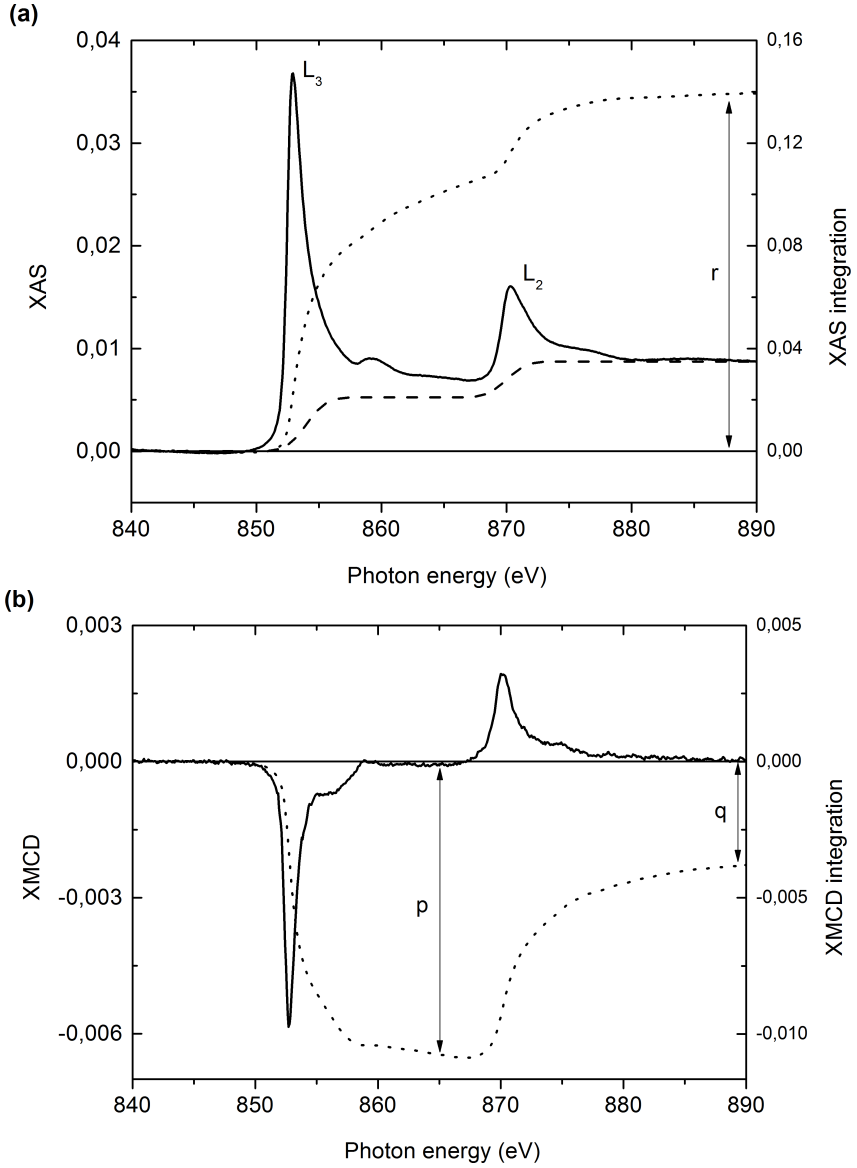

Figure 2.6: Ni $L_{2,3}$ (a) XAS (solid line) and two-step function (dashed line). The integration of the XAS spectra after removal of the edge jumps is shown as a dotted line. (b) XMCD (solid line) and its corresponding XMCD integration (dotted line)

2.1.3 Bulk magnetic moments

The description of the superconducting quantum interference device (SQUID) theory is based in the work of Barron, 2013 [165].

A SQUID consists of a superconductor ring with two weak links called Josephson junctions, figure 2.7. Josephson junctions allow current to pass with zero voltage if that current is less than a critical current I_c. If the current exceeds I_c, then a voltage V develops across the junction. If a current is applied to the coil, in parallel

across the Josephson junctions, these currents will become their critical currents. Any excess of current then will lead to a voltage across the SQUID. When a field B is applied so that an external flux enters the loop, then the loop compensate by generating a circulating current to maintain the flux quantization condition. This circulating current will cause one of the Josephson junctions to exceed its critical current I_c, and therefore a voltage V will appear across the SQUID.

In the superconducting loop the magnetic flux Φ, passing through it which is the product of the magnetic field and the area of the loop is quantized in units of $\Phi_0 = h/(2e)$, where Φ_0 is the critical flux, h is the Planck's constant and $2e$ is the charge of the Cooper pair of electrons. The superconducting current will compensate for the presence of an arbitrary magnetic field when there are no obstacles in the loop. In that case the total flux through the loop (external field plus the field generated by the current) is a multiple of Φ_0.

Finally, the voltage V is measured and then sent into a feedback system that applies a current I_{fb} through a loop, whose mutual inductance to the SQUID L_{fb} is known. The feedback flux $\Phi_{fb} = L_{fb}I_{fb}$ required to minimize V, is equal to the applied flux through the SQUID that generated the signal.

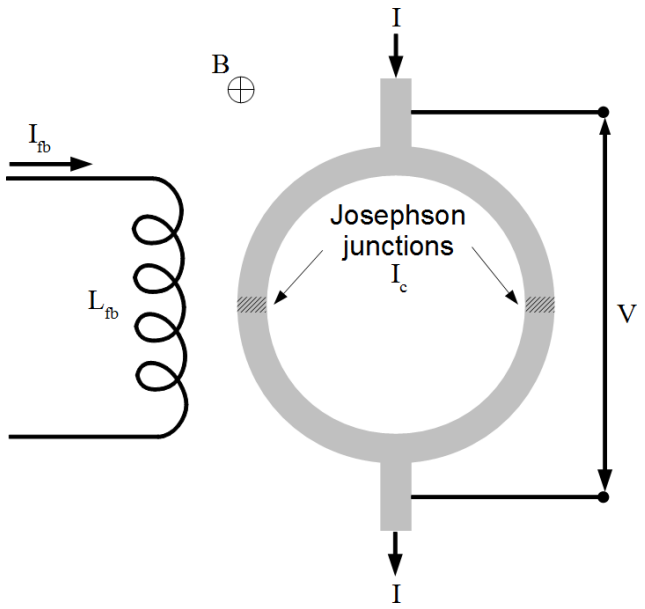

Figure 2.7: Schematic of an SQUID magnetometer

2.2 Experimental setups

2.2.1 Laser annealing and LA-CVD

A Janis ST-500H microscope cryostat has been used to anneal the nanotube samples by laser in vacuum. The laser is focused through a quartz window in the sample. An schematic figure and the real setup are shown in figure 2.8.

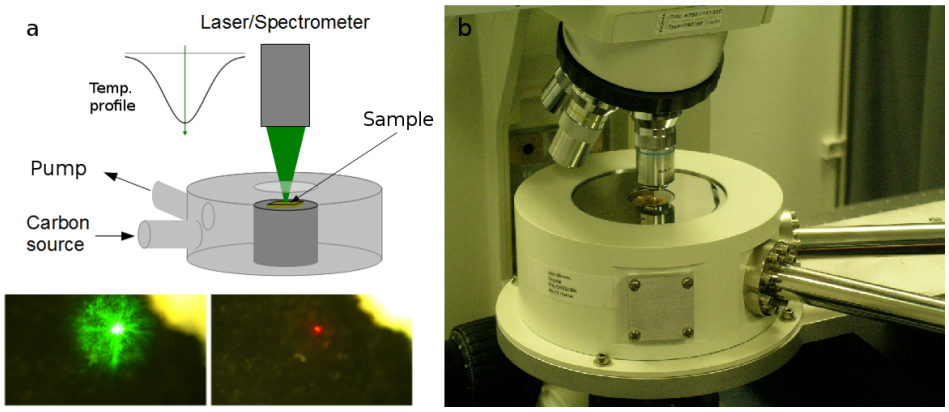

Figure 2.8: In-situ laser annealing and Raman spectroscopy setup. a) Schematic of the experimental setup, b) experimental setup, c) Alignment of the lasers. The green laser (514 nm) is used to anneal and the red (633 nm) laser is used to measure the Raman spectra.

A frequency doubled Nd:YAG laser, with wavelength of 532nm, was used for the laser annealing of the samples. A He-Ne (633nm) and a tunable Argon-Krypton mixed gas laser (458-647nm) were used to measure the Raman spectra. The spots of the lasers were aligned as shown in figure 2.8 in order to anneal and measure at the same point. The green spot corresponds to the annealing laser and the red one to the laser for Raman measurements. The measuring laser power is between 1-20 mW, while for annealing laser intensities between 0.5-1.0 mW are used.

Table 2.1: Composition of the multilayer catalysts used for LA-CVD of CNTs

Sample label	Substrate	Support		Mo (nm)	Co (nm)	Fe (nm)
		MgO (nm)	Al_2O_3 (nm)			
MLC1	Si + 1μm SiO_x	-	20	-	-	2
MLC2	Si + 1μm SiO_x	-	10	-	-	2
MLC3	Si + 1μm SiO_x	20	-	-	-	2
MLC4	Si + 1μm SiO_x	10	-	-	-	2
MLC5	Si + 1μm SiO_x	10	-	0.5	-	1.5
MLC6	Si + 1μm SiO_x	10	-	0.5	1.5	-

The LA-CVD synthesis of CNTs was performed on different supports and catalysts. The first approach to grow CNTs by laser-assisted CVD were done in pellets of a mixture of Al_2O_3(90%) and $FeCp_2$(10%). The pellet is prepared by grinding and mixing both powders in a mortar. The homogeneous mixture is then placed in a die and then a pressure of 10000 psi is applied for 30 seconds by using an hydraulic press. The pellet is placed inside the cryostat to proceed with the LA-CVD process, as shown in figure 2.8(a).

In the second approach, several multilayer catalyst (MLC) with different compositions (provided by Andreas Berger, CIC nanoGUNE) have been used to grow

CNTs in localized spots by LA-CVD. Table 2.1, shows the compositions of the MLC used to grow CNTs by LA-CVD. The MLC are place into the chamber as is shown in figure 2.8(a) to perform the LA-CVD process.

2.2.2 Filling of SWCNT

The procedure for the filling of the SWCNT consist of mainly three steps, as is shown in figure 2.9.

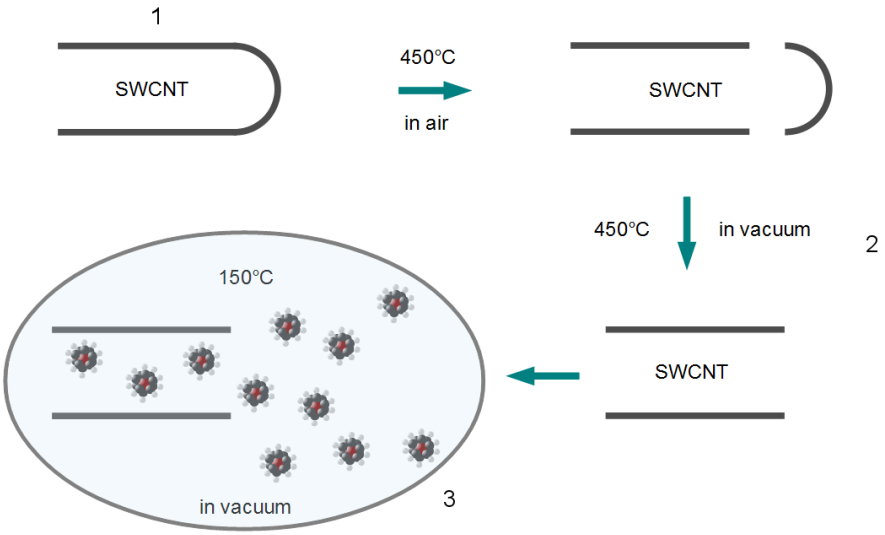

Figure 2.9: Schematic of the filling process of SWCNT with organometallic compounds.

1. SWCNTs are purified and prepared as buckypaper. In this work, HiPCO [35], laser ablation [30] and eDIPS [54] SWCNTs with mean diameter 1.0±0.15, 1.5±0.05 and 1.6±0.12 nm, respectively, have been filled. Bucky papers of metallicity sorted arc-discharge SWCNTs have been also used [166].

2. The buckypaper of purified nanotubes is annealed between 400-450°C in air for ∼1 hr to remove the tips of the tubes (open the tubes). During this step some defects are created in the tubes, facilitating the encapsulation of the molecules to be filled. After annealing in air, the open tubes are annealed in vacuum for ∼30 min to remove amorphous carbon.

3. Once the nanotubes are opened and clean, the buckypaper is placed in a glass tube together with the organometallic compound (metallocenes or metal acetylacetonates) to fill SWCNTs. The tube with the nanotubes and the powder

is then evacuated to a vacuum pressure of $2x10^{-6}$ mbar or lower. Once the desired vacuum pressure is reached the glass tube is sealed to get an ampoule containing the nanotubes and the powder of the organometallic compound.

The next step for the filling depends on the molecule to be encapsulated. The filling procedure can be performed in two different ways. When the molecule is stable at a temperature of 150°C approximately, the ampoule can be introduced directly in an oven and kept there for several days. This is the case for molecules like ferrocene or C_{60} fullerenes. If the molecule to be filled is not stable, i.e. it decomposes during the sublimation, the ampoule needs to be annealed by a coiled heating wire covering the powder and the buckypaper and leaving on side of the ampoule uncovered as is shown in figure 2.10. When the organometallic compound starts to evaporate, the molecules travel from the hot zone to the cold zone (uncovered with the wire) to form crystals. The temperature is measured with a thermocouple in contact with the heating wire.

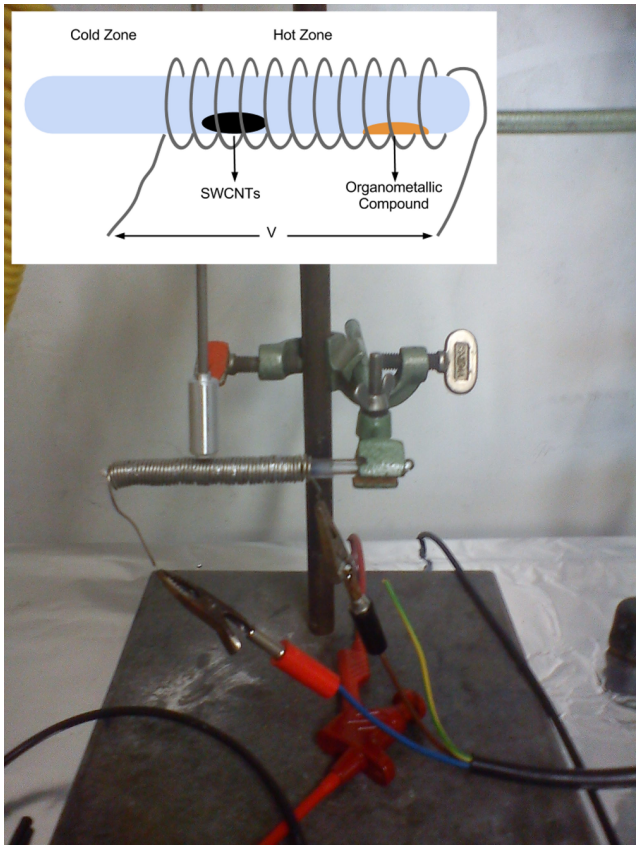

Figure 2.10: Schematic and setup for filling SWCNT using a heating wire.

After several days, the annealing process is stopped and the ampoule is opened. The buckypaper is again placed in high vacuum and annealed for 1 hr to remove the remaining molecules attached to the nanotubes surface.

2.2.3 Raman spectrometers

Three different spectrometers equipped with cooled CCD detectors were used to record the Raman spectra of the samples.

A Brucker RFS 100/S FT-Raman Spectrometer with a laser wavelength of 1064 nm was used in micro and macro mode. The spectra were recorded with 1 cm^{-1} resolution.

A HORIBA LabRAM HR800 spectrometer equipped with a confocal microscope (figure 2.11) was used to measure the samples in micro mode with a spectral resolution up to 2 cm^{-1}. An internal 633 nm laser and an external tunable Ar/Kr mixed gas laser with wavelengths between 458-647 nm were used as excitation sources.

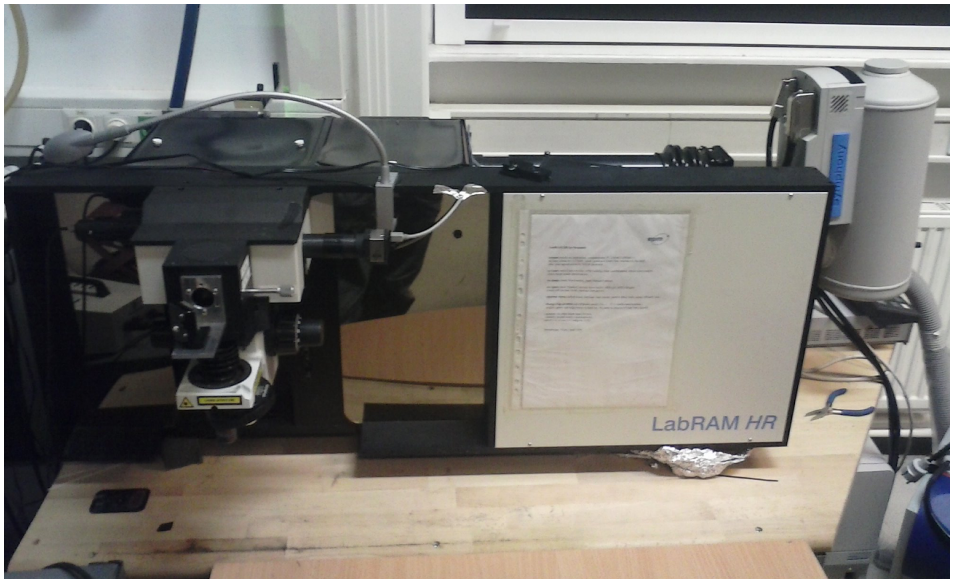

Figure 2.11: HORIBA LabRAM spectrometer equipped with a confocal microscope.

A Dilor XY triple monochromator with two resolution modes has also been used in micro and macro mode. The resolution in the normal mode is about 2 cm^{-1} and in the high resolution mode is 0.5 cm^{-1}. A tunable Ar/Kr mixed gas laser with wavelengths between 458-647 nm were used as excitation sources.

Measurements of the samples in bulk were done in macro mode with high sensitivity. In the micro mode, the samples were placed under objectives of the built-in microscope (10x and 50x), allowing to measure spots of 1 μm^2. Laser intensities up to 5 mW were used to measure without observing heating effects.

2.2.4 SQUID

Bulk magnetic properties of the samples were measured in a Quantum Design MPMS-XL SQUID magnetometer at the Atominstitut (TU Wien). Magnetic fields up to 7 T were applied to the samples at temperatures ranging from 5 to 300 K. The data was recorded using the reciprocating sample option (RSO) that avoids the field

inhomogeneities that affect the DC scan mode caused by the small size and possible movements of the sample.

2.2.5 Beamline UE46/PGM-1 at BESSY II

The XAS and XMCD measurements were carried out at the variable polarization undulator beamline UE46-PGM-1 at the BESSY II (Helmholtz-Zentrum Berlin) synchrotron facility. Circular polarization dependent XAS were obtained by measuring the sample drain current with the photon helicity parallel ($\mu+$) or antiparallel (μ-) to the sample magnetization. The energy range is 120-2000 eV with an energy resolution of 10,000.

The experimental high-field end-station of this beamline allows cooling the sample down to 5 K applying a magnetic field up to 7 T. XAS spectra were taken at the L-edge of the corresponding metal encapsulated in the SWCNT sample. The base pressure in the measurement chamber was kept below $5x10^{-10}$ mbar. A heating station in the preparation chamber was used to in-situ anneal the filled nanotube samples to transform the organometallic molecules to inner tubes and metal clusters. Figure 2.12 shows the high-field end-station (left) and the UE46-PGM-1 beamline (right).

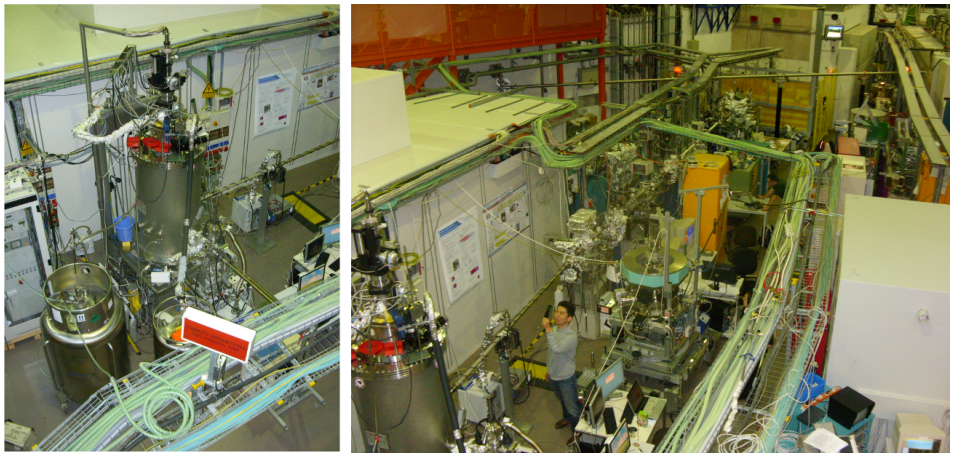

Figure 2.12: UE46-PGM-1 beamline and high field end-station.

2.2.6 X-ray characterization

X-ray scattering was performed with a rotating anode generator (Nanostar, turbospeed solution, Bruker AXS, Karlsruhe, Germany), equipped with an area detector (Vantec 2000, gas-detector based on microgap technology) and an additional image plate (Fujifilm FLA-7000, Japan) for simultaneous small-angle scattering and wide-angle diffraction. The beam diameter of the system, which fully operates in vacuum, is about 0.5 mm. X-ray images were typically measured for one hour and radially averaged to give the scattering intensity in dependence on the scattering

vector $q = (4\pi/\lambda)\sin\theta$. Here, 2θ is the scattering angle and λ=0.1542 nm is the X-ray wavelength (CuKα radiation). The images were then background corrected by subtracting the q^{-4} intensity from large objects (>100nm) within the samples. Using both the gas-detector and the image plate, the maximum accessible q-range of the system is 0.08 to 50 nm^{-1}. The size of the particles was determined by the Scherrer equation:

$$L = \frac{K\lambda}{\beta\cos\theta} \tag{2.4}$$

Where λ is the x-ray wavelength, $\beta = \triangle(2\theta)$ is the line broadening, 2θ the scattering angle and θ the Bragg angle. A shape factor K=0.9 is assumed, considering the shape of the crystallite as unknown [167].

Chapter 3

Local growth and transformation of CNTs

3.1 Introduction

The transformation of SWCNT encapsulating fullerenes (peapods) into DWCNT by laser annealing was proved and reported in [130]. In the first part of this chapter the use of a laser to locally anneal and transform organometallic molecules (ferrocene) encapsulated in SWCNT into DWCNT is discussed. The filling and the in-situ laser annealing setup are described in the first section of Chapter 2. In the second part, the laser assisted chemical vapor deposition (LA-CVD) method is used to synthesise carbon nanotubes using different supports and catalysts. The setup used in the LA-CVD process is similar to the in-situ laser annealing setup described in the first section of Chapter 2, with a slight modification to introduce the carbon source to the chamber during the synthesis process.

The results shown in the first section of this chapter were published in PSSB [20].

3.2 Laser induced nanochemcal reactions of ferrocene filled SWCNT

The transformation of the $FeCp_2$@SWCNT was first done by furnace annealing of eDIPS and HiPco samples to have reference samples. Figure 3.1 depicts the Raman spectra of both types of samples. The eDIPS tubes (figure 3.1, left) before annealing have low frequency RBM between 120 and 200 cm^{-1} (1.6±0.12 nm). When the eDIPS sample is annealed in the furnace above 550°C, the RBM for the inner tubes is well observed between 200 and 275 cm^{-1}. For the HiPco sample (figure 3.1, right), the RBM of the outer tubes is between 150 and 320 cm^{-1} (1.0±0.15 nm) before annealing. The transformation to DWCNT for the HiPco sample occurs at 570°C showing the RBM of the inner tubes between 450 and 500 cm^{-1}. In both samples the annealing time was 2 hours. For the HiPco sample, rising the temperature beyond 700°C causes the destruction of the thin inner tubes, unlike the eDIPS sample were both, the outer and inner tubes, remain above 1000°C. The inner tube growth process of $FeCp_2$@SWCNT was described in [117]. After $FeCp_2$ decomposition and growth of inner tubes, iron nanoparticles remain inside the DWCNT.

Turning to the local laser annealing case, figure 3.2 shows the RBM of the three

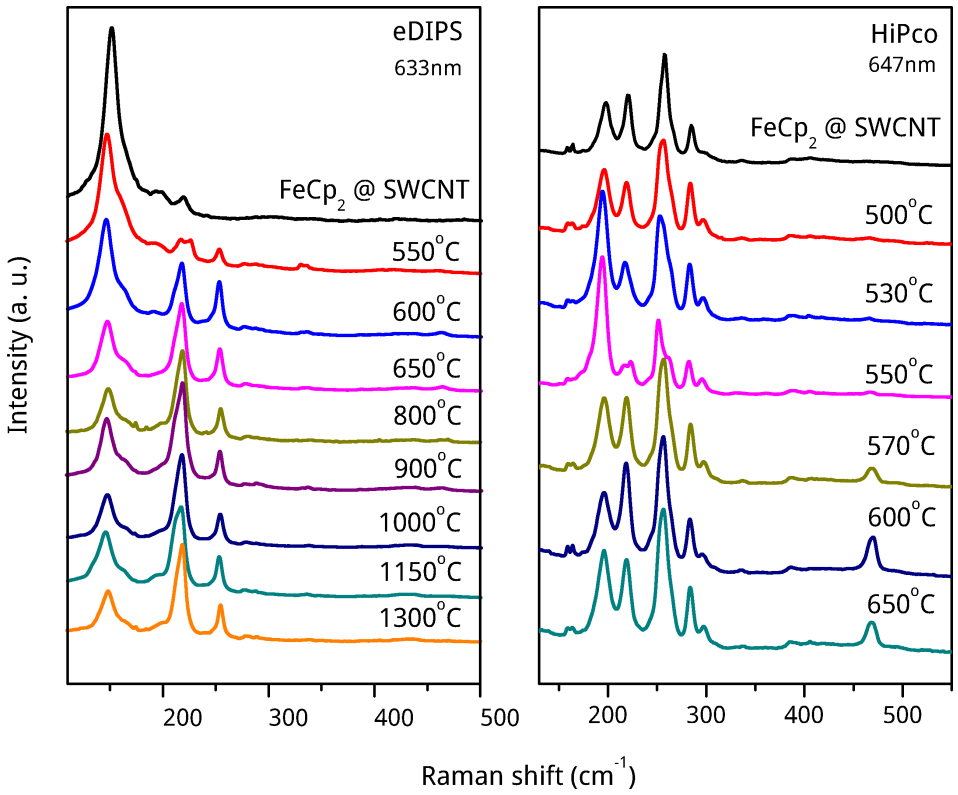

Figure 3.1: RBM of two samples with different diameters distribution annealed by furnace during 2 hours; eDIPS sample measured with wavelength of 633 nm (left), HiPCO sample measured with a wavelength of 647 nm (right).

samples studied. The presence of inner tubes is clear for the eDIPS sample (left). As well as in the spectra recorded for the tubes processed by furnace annealing, the frequency for the inner tubes is localized between 200 and 275 cm^{-1}. The transformation to DWCNT was achieved at 160 mW, and no significant changes were observed above this laser power. For the LA sample (middle) the inner tubes were also obtained at 160 mW laser power, shown in the RBM between 120 and 250 cm^{-1}. The resonance response of the inner tubes using the 633nm laser lines is not as strong as for the eDIPS sample, but the RBM of the inner tubes is also clear and it is between 300 and 400 cm^{-1}. The Raman spectra does not change considerably below 700 mW, above this power the inner tubes are destroyed and defects increase on the outer tubes. For the HiPco sample (right) there is no resonance of the inner tubes with the 633 nm laser. Other laser lines were used to monitor the presence of their inner tubes. With the 647 nm line (inset), the Raman spectrum shows the response of the inner tubes between 450 and 500 cm^{-1}, the same as in the furnace annealing process. For laser powers above 160 mW the inner tubes are destroyed and the sample starts to be more defective, proved by the increase of the D-band

(figure 3.3). The main diameters of the outer and inner tubes, corresponding to the RBM measured with the 633 nm laser of the three samples, are shown in Table 3.1.

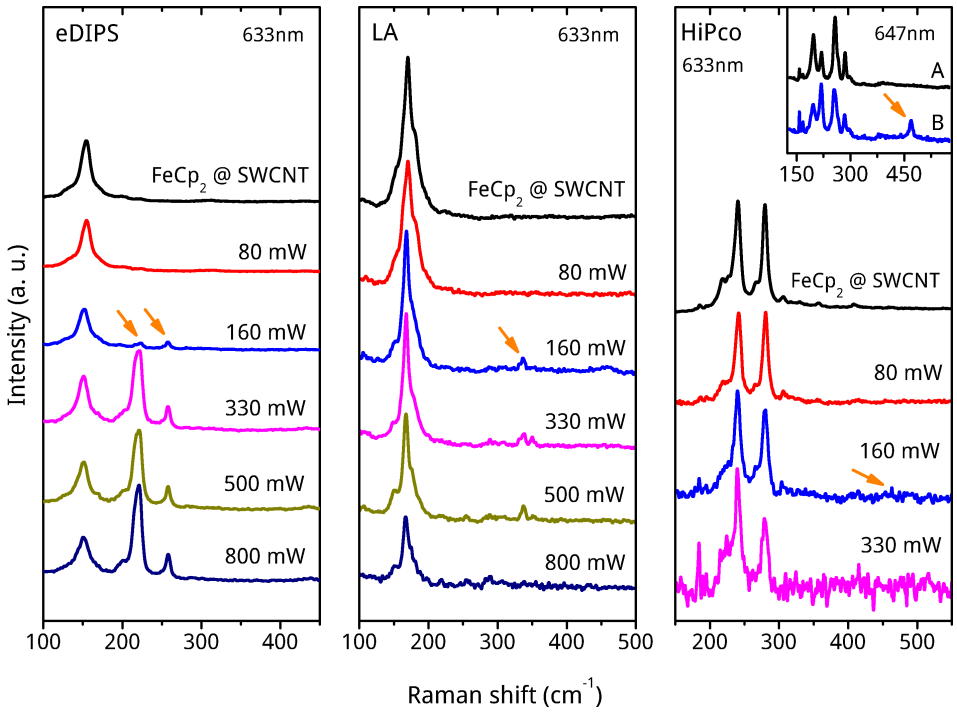

Figure 3.2: Raman spectra in the RBM for the three samples measured with the 633 nm laser line. Left, eDIPS; middle, LA and right, HiPco. All the samples were annealed during 1 min with the frequency doubled Nd:YAG laser line (532 nm). Inset: RBM of the HiPco sample measured with the 647 nm laser line, the spectra correspond to the $FeCp_2$ @ SWCNT before (A) and after (B) annealing.

Table 3.1: Raman peak positions and observed outer and inner tube diameters at 633nm.

Sample	Outer tubes		Inner tubes	
	RBM (cm^{-1})	~d (nm)	RBM (cm^{-1})	~d (nm)
eDIPS	152	1.60±0.13	221	1.06±0.05
			258	0.90±0.01
LA	168	1.43±0.06	337	0.68±0.02
HiPco	240	0.97±0.03	469	0.48±0.01
	280	0.83±0.02		

The G-band of the Raman spectra of the annealed samples is depicted in figure

3.3. After the growth of the inner tubes, an increase in the D-band and the decrease of the G-band is evident. By increasing the laser power this ratio between G and D modes gets lower, this corresponds to an increment of the defects on the sample. At the same time, the valley in the G-band is covered by the downshifted response of the additional inner tube. A peak between 1225 and 1270 cm^{-1} is present when the transformation from $FeCp_2$@SWCNT to DWCNT is completed, the peak disappears as the laser power is increased. The nature of this peak is still under debate. However, the dispersion of this peak indicates a corresponding D-band of the inner tubes.

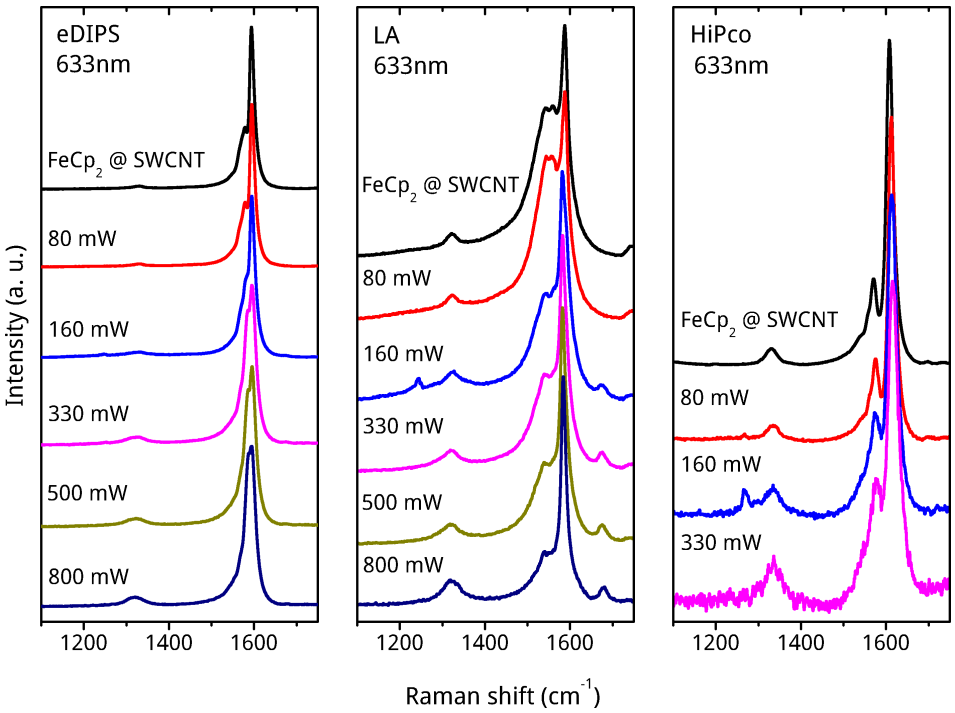

Figure 3.3: Raman spectra in the G and D modes for the three samples measured with the 633 nm laser line. Left, eDIPS; middle, LA and right, HiPco.

The Raman spectra for the eDIPS sample excited with different lasers is shown in figure 3.4. The resonance response for the transformed DWCNT is different for every laser line. The response of the eDIPS sample for wavelengths between 458-514 nm is lower in intensity than for high wavelengths. On the other hand, the 633 nm laser seems to offer more information about the behavior of the transformation to DWCNT because of the best resonance condition of the inner tubes.

No additional changes in the spectral features from inner tubes were found with increasing the annealing time between 30 and 480 sec at 160 mW with the infrared Nd:YAG laser (1064 nm). It means that the inner tubes grow within less than 30 sec under this condition. In the furnace, the annealing time required to transform the ferrocene to inner tubes is of several minutes, which is much longer than in the

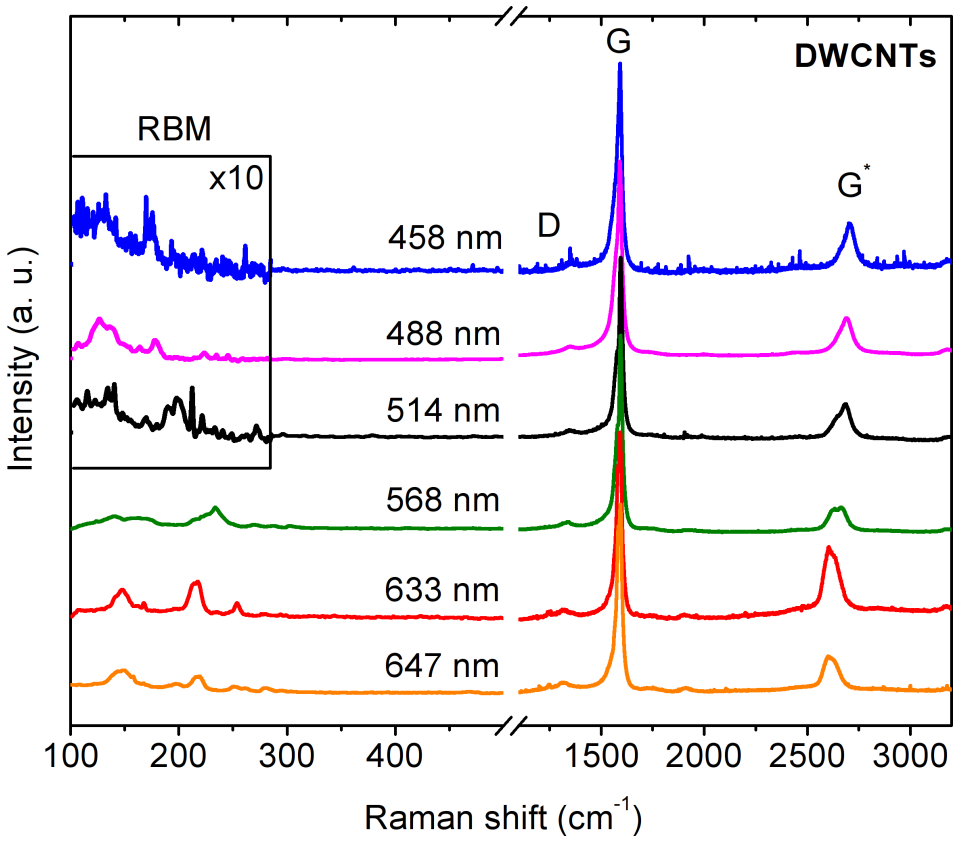

Figure 3.4: Resonant Raman spectra of DWCNT produced from $FeCp_2$@eDIPS by laser annealing at 540 mW for 1 min.

laser annealing. With high laser power, the fast transformation of the inner tubes as well as their destruction is observed. Laser annealing effects can be attributed to two main reasons. First, the non-linear heating induced by the laser, i.e. the temperature on the sample do not increase proportionally with increasing the laser power. Second, the photo-induced effect of the laser: when the outer tube band gap matches the laser energy, in which case the resonant absorption dramatically increases the annealing effects [168].

The transformation of ferrocene filled SWCNT to DWCNT has been achieved by laser annealing. Annealing effects are clearly dependent on the diameters of the SWCNT, as it was observed with the destruction of the SWCNT with high laser powers. The laser annealing has two main advantages in comparison to the furnace annealing process. First, the annealing time required for the transformation is considerably lower with the laser than with the furnace. Second, the local probing of the laser annealing lets chose an area as small as the size of the laser spot used for these purposes. The laser annealing opens the possibility to produce novel carbon nanostructures using SWCNT as nanoreactors, in order to tune the electronic and magnetic properties of these materials.

3.3 Laser-assisted CVD of carbon nanotubes

3.3.1 LA-CVD on powder

The first experiments to synthesize CNTs by LA-CVD were done in the pellets of $Al_2O_3/FeCp_2$ prepared as described in Chapter 2.

Figure 3.5 depicts the Raman spectra of different spots on the pellet before and after laser irradiation for 5 min with different laser intensities. The spectra were measured at 488 nm wavelength. Before the synthesis process, the pellet does not show any Raman response. The G and D Raman modes appear at 50 mW of laser power. From 50 to 250 mW, the Raman spectrum of the grown nanostructures has the characteristics of MWCNTs with a D/G ratio of 1.18, as observed in figure 3.5. At 300 mW SWCNTs are obtained. The peak at $\sim$179 cm^{-1} corresponds to a SWCNT with diameter of $\sim$1.3 nm. The D/G ratio of the spot irradiated at 300 mW is 0.58. Two RBM peaks are observed in the SWCNTs grown at 350 mW. The same peak that the 300 mW annealed spot at $\sim$179 cm^{-1} and another peak at $\sim$203 cm^{-1} corresponding to nanotube diameters of $\sim$1.3 and 1.16 nm, respectively. The D/G ratio decrease to 0.66. At 500 mW of laser power, the peak at $\sim$179 cm^{-1} vanishes and the D/G ratio increases to 0,80.

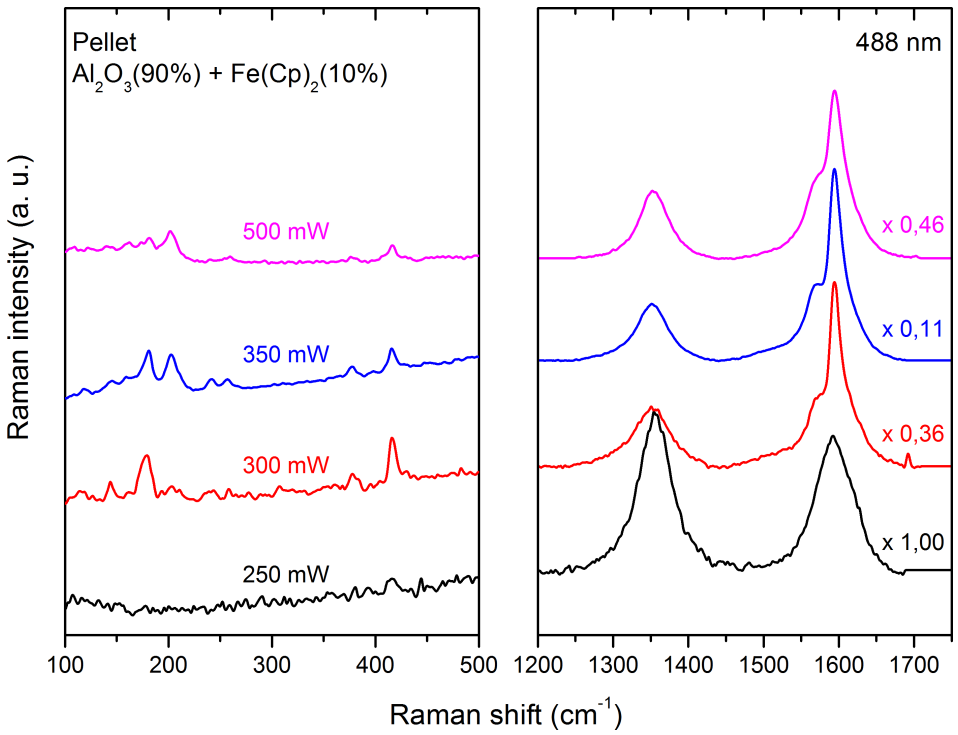

Figure 3.5: Raman spectra of CNTs grown on a $Al_2O_3/FeCp_2$ pellet for 5 min as function of the laser power indicated by the labels. The spectra are normalized to the intensity of the G peak. The Raman spectra were measured with a 488 nm laser wavelength.

Significant structural changes are induced to the grown nanotubes by using different laser intensities. A low value of the D/G ratio, is a measure of the quality of the nanotubes grown. The lowest D/G value obtained is in the spot annealed at 300 mW where the most intense Raman peak is also observed. By further increasing the laser intensity decreases the quality of the grown nanotubes. Different diameter distributions can be also obtained by changing the laser power. The amount of the SWCNTs grown can be approximated by the relative intensities. A higher amount of CNTs in the spot annealed at 350 mW is observed. With increasing the laser power, SWCNTs are destroyed and the spectral intensity decreases.

The low thermal conductivity of the powder allows the growth of SWCNTs by LA-CVD. The best quality of SWCNTs produced was observed in pellets of Al_2O_3(90%)/$FeCp_2$(10%) annealed at 300 mW.

3.3.2 LA-CVD on predefined substrates

The synthesis of CNTs as function of the laser intensity was done in the multilayer catalysts (MLC) listed in table 2.1. The MLC used have either Al_2O_3 or MgO as support layer. The samples with a support thickness of 10 nm (MLC2, MLC4, MLC5, MLC6) do not show carbon nanotubes growth by LA-CVD. The analysis of the results of synthesis using the MLC1 and MLC3 are discussed next.

In figure 3.6(top) the Raman spectra on different places of the spots after the LA-CVD process in the MLC1 are shown. When the MLC is irradiated in the ethanol atmosphere with the laser, the heating distribution is concentrated in the center of the spot (1) where the nanotubes grow. Out of this spot there is no growth of CNTs. In the MLC3, the heating distribution is broader (figure 3.6(bottom)). Amorphous carbon is deposited in the center of the spot (1), the CNTs are grown mostly in the next ring (2) followed by some CNTs of lower quality (3) and amorpouos carbon deposition (4,5) (3,4,5,6). The laser intensity was chosen to obtain a visible black spot in the microscope. All these spectra where measured with a 633 nm laser wavelength.

The thermal conductivity of the MLC affects the shape of the spot where the CNTs are growing. In the case of the MLC1, CNTs can grow in a uniform spot. In the case of the MLC3 a ring shape of CNTs is obtained.

Figure 3.7 shows the Raman spectra for the MLC1 after the LA-CVD process varying the laser intensity. CNTs were grown after irradiate the MLC with the laser at 0.5 W in ethanol vapor for 5 seconds. By increasing the intensity to 1.0 W the D line of the Raman spectrum gets narrow and radial breathing mode (RBM) appears. When a laser power of 2.0 W is applied during the LA-CVD process, the D line gets broader and the RBM signal vanishes. The broadening of the D line after increasing the intensity means a transformation of the CNTs into amorphous carbon. The inset in figure 3.7 shows a close up of the RBM signal. The intensity of the first peak at 211 cm^{-1} is around the noise level of the spectrum and it is not considered as a RBM of an specific SWCNT. The second peak at 243 cm^{-1} is much higher in intensity, corresponding to 0.95 nm SWCNT diameter at 1064 nm wavelength.

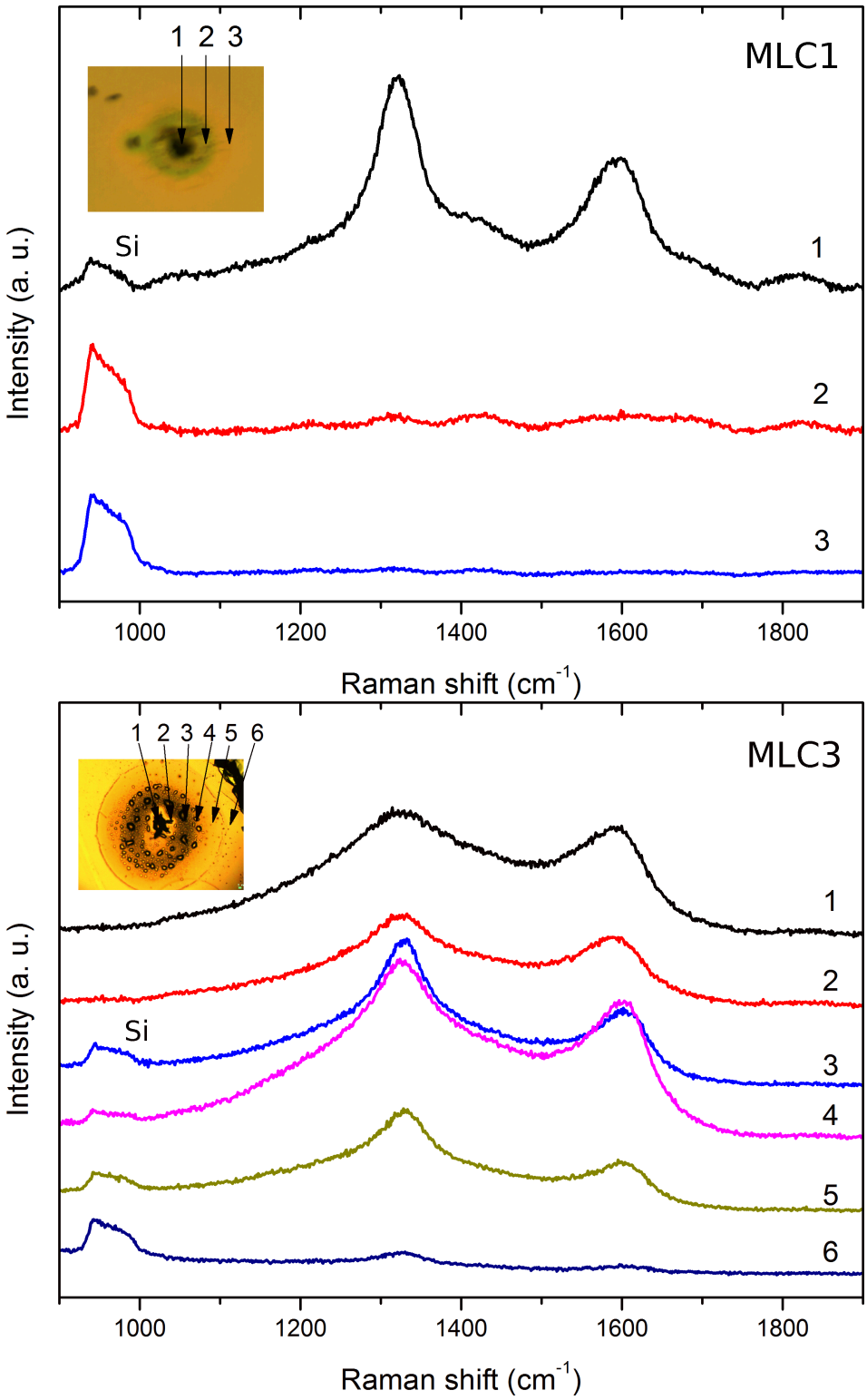

Figure 3.6: Raman spectra of different points in the multilayer catalyst with (top) Al_2O_3 and (bottom) MgO after the laser assisted CVD process. The insets show the localization of each spot ($\backsim 10\,\mu$m) taken with the optical microscope. The approximated size of the spots are $1\,\mu$m (top) and $15\,\mu$m (bottom). The Raman spectra were measured with a 633 nm laser wavelength.

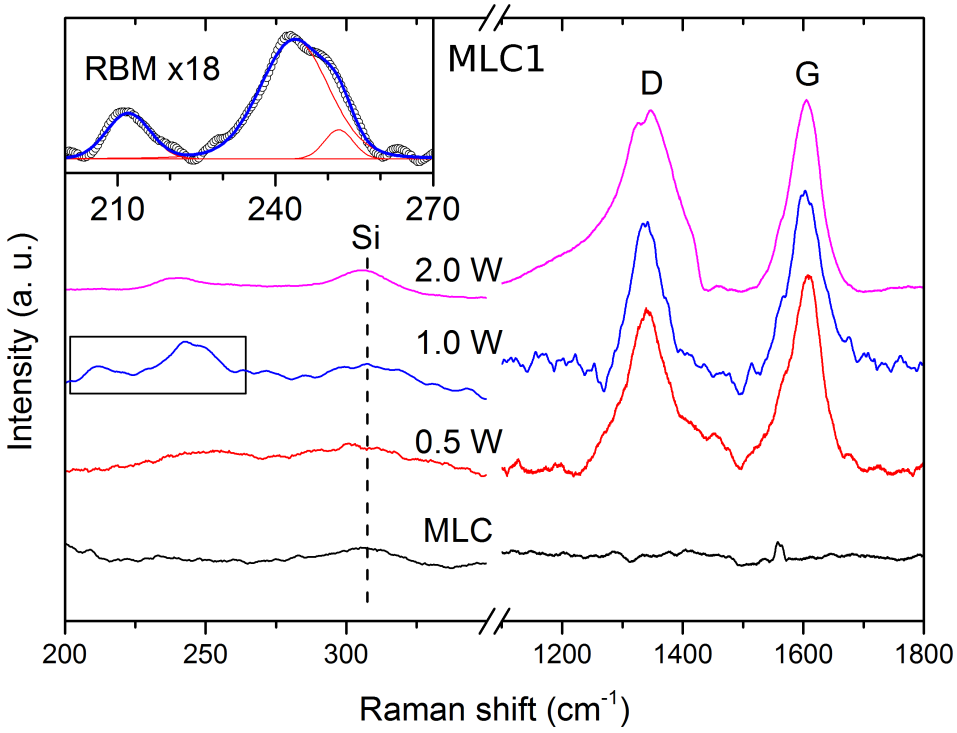

Figure 3.7: Intensity dependence Raman spectra of the MLC with Al_2O_3 as support catalyst (MLC1) after the laser assisted CVD process. The inset in left panel shows the RBM signal of the grown nanotubes. The Raman spectra were measured with a 633 nm wavelength.

The Raman sectra of the MLC3 after the LA-CVD process is shown in figure 3.8. The MLC with MgO as support layer does not show evidence of SWCNT, no RBM are observed at low wave numbers. The effect of increasing the laser intensity in the LA-CVD synthesis of CNTs is different in this case. A broad D line is observed at 0.5 W, when the intensity is increased the D line becomes narrower but the D/G ration is higher than using Al_2O_3 as support layer.

This can be explain in terms of the difference between the thermal conductivity of both supports. Al_2O_3 in the bulk has a thermal conductivity of 30 $W\,m^{-1}\,K^{-1}$ while the thermal conductivity of MgO is 45-60 $W\,m^{-1}\,K^{-1}$. As is observed in the evolution of the Raman spectra by increasing the intensity of the laser, MgO needs more power to reach the temperature needed to grow SWCNT

Another attempt to control the temperature during the growth of CNTs, was done by changing the focal distance of the laser in the MLC1. A considerable improvement in the quality of grown nanotubes was observed. In figure 3.9 a Raman spectrum of the CNTs grown by controlling the focal distance during the LA-CVD process. Both peaks, the G and D lines, are narrower than in the previous experiments with a D/G ratio of ∼0.91. The inset shows a close up of the RBM, and is possible to clearly observe two main peaks at 198 and 218 cm^{-1} corresponding to

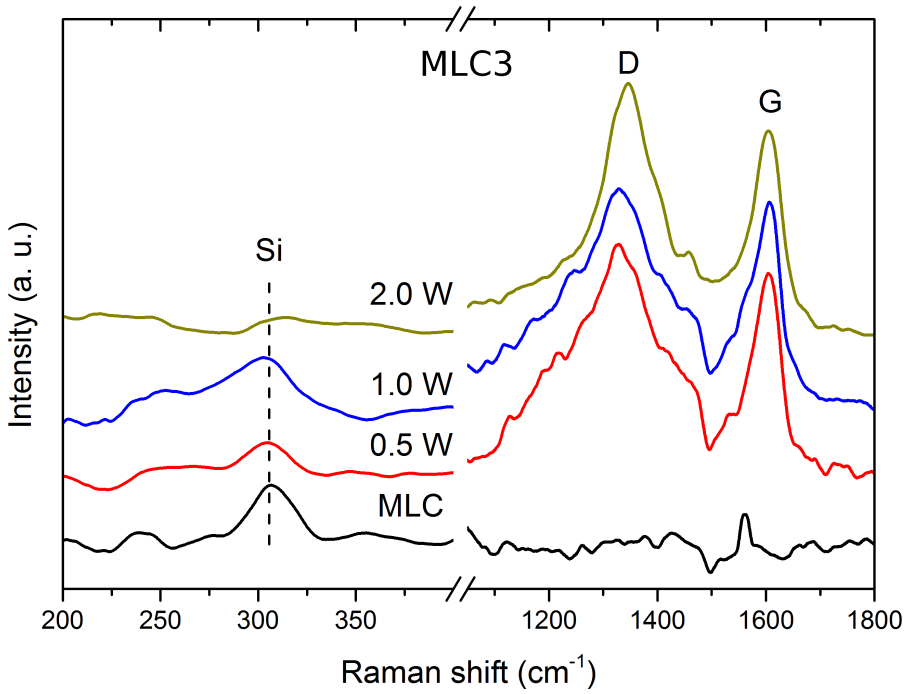

Figure 3.8: Intensity dependence Raman spectra of the MLC with MgO as support catalyst after the laser assisted CVD process. The Raman spectra were measured with a 633 nm wavelength.

SWCNT with diameters of 1.22 and 1.08 nm, respectively.

In figure 3.10, SEM images of the synthesized spots are shown at different magnifications. The center of the spot is depicted in the top-left micrograph. Very thin nanotubes (SWCNT) deposited in the substrate as a film are observed. At the edge of the spot, top-right image, a small amount of SWCNT are observed but with a high concentration of MWCNTs. Although the structural differences in the center and in the edge, the deposited film of CNTs looks more homogeneous (bottom) than those ring shape spots reported in other works [91, 94, 169]. The oval shape of the spot is due to the optical alignment.

The temperature induced by the laser during the LA-CVD process is sufficient to grow CNTs on predefined substrates. In table 3.2 a list of the MLC after the LA-CVD process is shown. The 10 nm thick support layer (Al_2O_3 or MgO) is not sufficient to contain the heating induced by the laser in a localized spot, so the heating is dissipated on the Si substrate. That can be the reason for the CNTs to not grow on the MLC with this support layer thickness.

The thermal effect induced by the CW laser during the synthesis of CNTs is less significant in the powder than in the MLC. This is due to the low thermal conductivity of the powder. In the case of the MLC, the substrate acts dissipating the heating, making difficult the control of the temperature during the nanotube growth.

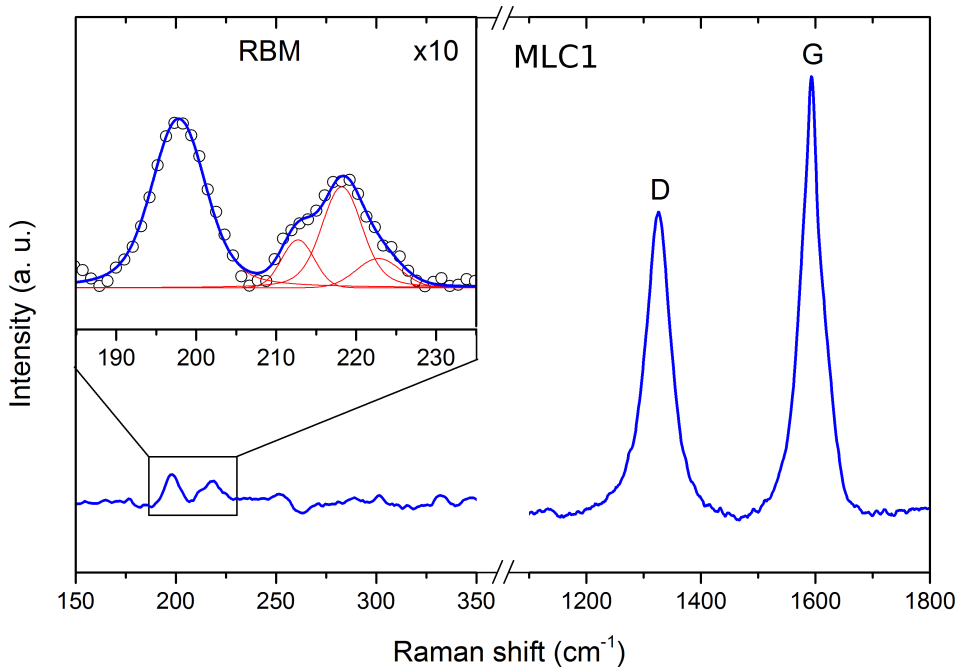

Figure 3.9: Raman spectra of spot of CNT grown in the MLC1 by LA-CVD. The inset shows the RBM signal of the nanotubes. The Raman spectra were measured with a 633 nm wavelength.

Table 3.2: List of the multilayer catalysts after the LA-CVD process.

Sample	MWCNT	SWCNT
MLC1	✓	✓
MLC2	-	-
MLC3	✓	-
MLC4	-	-
MLC5	-	-
MLC6	-	-

It is evident that a proper choice of the composition of the MLC leads to an improvement of the quality of the synthesized nanotubes. Other compositions of catalysts deposited on substrates plus their reduction by hydrogen treatment have been successfully used to grow aligned SWCNTs [69]. In that sense, different compositions and thicknesses of MLC need to be tried in order to choose the best combination of substrate and catalyst to grow aligned SWCNT by the LA-CVD process.

Further optimizations of the setup are also needed to locally grow aligned SWCNTs by this method. The possibilities to introduce hydrogen to reduce the catalyst and additional ways to measure the temperature in the sample are indispensable.

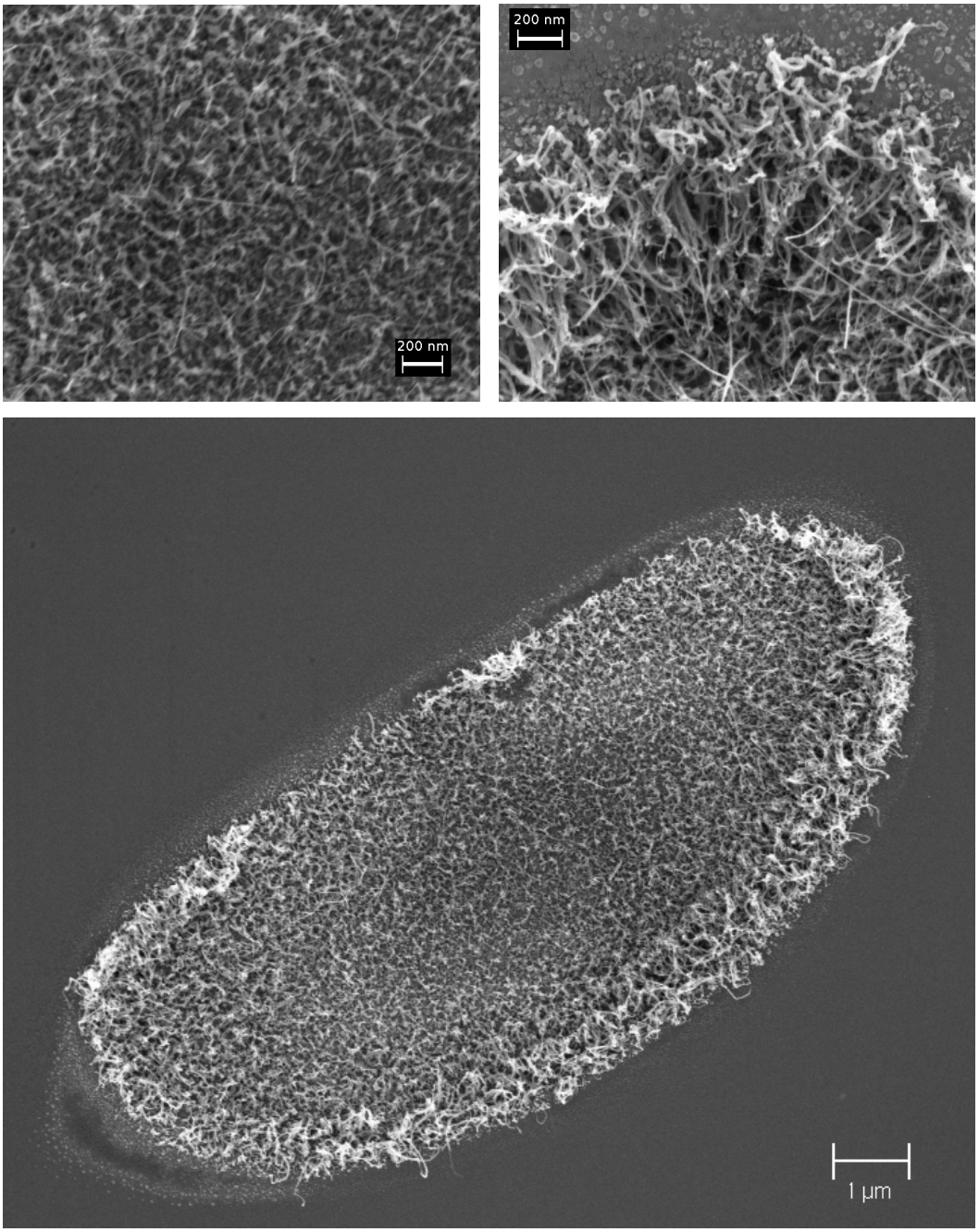

Figure 3.10: SEM micrographs of CNTs grown on the MLC containing the Al_2O_3 support layer.

Chapter 4

Magnetism in SWCNT encapsulating metallic clusters

4.1 Introduction

In this chapter, the magnetic properties of low-dimensional metallic clusters encapsulated in SWCNT are studied. Organometallic compounds have been initially introduced inside SWCNT and then transformed to metallic clusters via nanochemical pyrolisis.

In the first part of this chapter, the analysis of the magnetic moments of iron carbide inside SWCNT with different metallicities is presented. In the second part, the magnetism of nickel encapsulated in SWCNT is studied as function of the filling duration and annealing temperature.

The molecular orbital states of the encapsulated molecules before and after the transformation are analysed by the XAS measurements. The spin and orbital magnetic moments are evaluated from the XMCD data by using the sum rules [159, 160]. Structural information of the encapsulated clusters is extracted from the XRD measurements.

The results shown in the first section of this chapter were published in PSSB and PRB [21, 22].

4.2 Magnetism of Fe carbide inside metallicity sorted SWCNT

4.2.1 XAS and XMCD

The XMCD signal is defined as the difference between the XAS spectra measured at both polarizations ($\mu^+ - \mu^-$). We observe no XMCD signals at 0 T (not shown). The XAS and XMCD spectra for the metallicity sorted $FeCp_2$@SWCNT at the $L_{2,3}$ Fe edge at magnetic field of 6 T are depicted in figure 4.1. The shown spectra were recorded at 5K. For ease of comparison, the recorded spectra are normalized by the average area of the L edge XAS $\int(\mu^+ + \mu^-)/2$ and offsetted by 0.1. The XAS response shows slight dependency on the light polarization, figure 4.1a. The spectral shapes before annealing are in good agreement with those of ferrocene encapsulated in SWCNT, reported in the previous work on mixed [124] and separated samples [170]. The main spin-orbit splitting features L_3 and L_2 located at 710.3, 712.5 eV, and 722.6, 724.9 eV, respectively, coincide with those characteristic to the molecular

orbitals of ferrocene observed in solids [171]. The feature at 709.5 eV could be characteristic of encapsulated ferrocene, that was less significant but also observed in the previous work [124]. This feature shows a slight difference between the semiconducting and the metallic samples, which can be attributed to two possible effects: 1) the encapsulated molecules interacting with different proportions of metallic and semiconducting nanotubes or 2) the presence of Fe impurities in the samples. The corresponding XMCD are depicted in figure 4.1b. The main peak in the XMCD signal of $FeCp_2$@SWCNT correspond to the low energy band feature at 709.5 eV in the XAS signal. The XMCD signal is larger for the semiconducting nanotubes than the metallic ones. No contribution from the L_2 edge is observed.

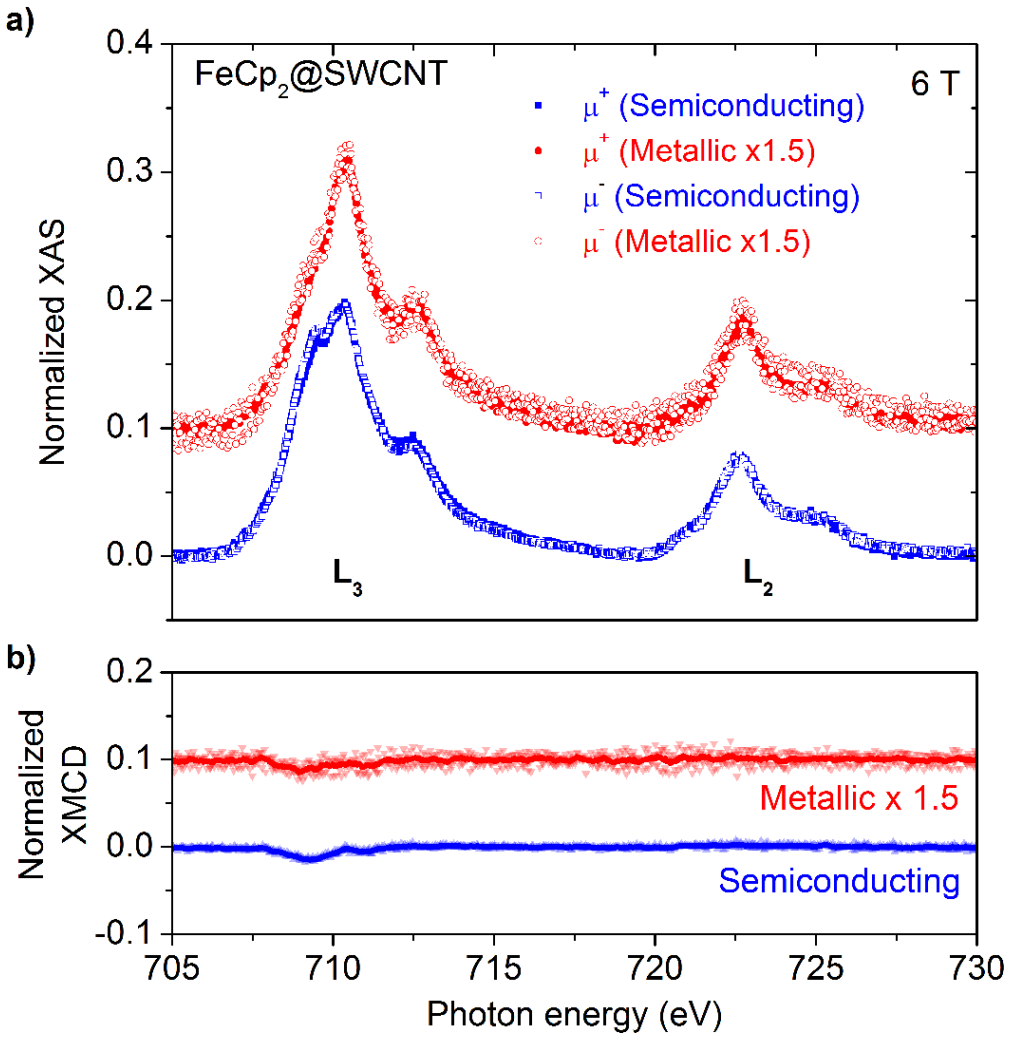

Figure 4.1: Observed XAS (a) and XMCD (b) response in the $L_{2,3}$ edge of Fe for the metallic and the semiconducting $FeCp_2$@SWCNT samples when a magnetic field of 6 T is applied to the sample at 5 K. All the spectra are offset by 0.1 and normalized by $\int(\mu^+ + \mu^-)/2$.

Provided that all the spectra were collected at the nearly identical experimental condition, except for the polarization of the light and magnetic field, the spectral intensity integrated over the Fe 2p edge is closely related to the concentration of Fe inside the nanotubes.

A filling factor of 44% was first determined for a non-separated SWCNT sample from XAS measurements at the C1s π edge by M. Sauer et al. [170]. From this value, by considering the differences in the XAS spectral intensity integrated over the Fe edge, filling factors of 49% and 30% were determined for the filled semiconducting and metallic samples, respectively. At room temperature no difference between μ^+ and μ^- was observed for the semiconducting and metallic $FeCp_2$@SWCNT, which means no XMCD response.

After annealing the $FeCp_2$@SWCNT samples above 500°C for several hours, the ferrocene inside the nanotubes decomposes and forms inner tubes and iron carbide Fe_3C clusters (Fe_3C@SWCNT), as proved by XAS and TEM studies (figure 4.6). In figure 4.2, the XAS and XMCD spectra for the $FeCp_2$@SWCNT samples are shown. The spectra were recorded at 4 T and room temperature. For ease of comparison, the recorded spectra are normalized by the average area of the L edge XAS $\int(\mu^+ + \mu^-)/2$ and offset by 0.1. The spectra are significantly altered in shape by annealing and composed of the two main skewed spin-orbit splitting peaks L_3 and L_2 located at 709.3 and 722.2 eV, respectively, figure 4.2a. From the spectral shapes and energies, these features can be assigned to metallic Fe [164, 172].

The effect of applying a magnetic field is more significant than in the samples before annealing, figure 4.2a. The XMCD signal for the Fe_3C@SWCNT is larger than that for the $FeCp_2$@SWCNT, figure 4.2b. The formation of the cementite clusters enhances the magnetic response of the filled nanotubes. The difference between the two different metallicity samples is greater for the Fe_3C@SWCNT. This difference can be attributed to the formation of larger cementite clusters due to the higher filling factor in the semiconducting nanotubes.

4.2.2 Spin and orbital magnetic moments

The experimental spin (m_S) and orbital (m_L) magnetic moments of the metallicity sorted $FeCp_2$@SWCNT samples are shown in figure 4.3 as a function of the applied magnetic field. The experimental data were fitted by a modified Langevin function:

$$M(x) = M_{S,L}(\coth(x) - 1/x) \tag{4.1}$$

where $M_{S,L}$ is the saturation magnetization of the spin (S) or the orbital (L) magnetic moments; $x = \mu_c H/k_B T$, in which μ_c is the uncompensated magnetic moment associated with the nanoparticle core, H is the applied magnetic field, k_B is the Boltzmann constant and T is the temperature.

The saturation values $M_{L,S}$ obtained for the filled samples and the reference values for bulk iron are listed in Table 4.1. The saturation value of the total angular moment reported for cementite (1.8 $\mu_B/atom$)[173] is lower only by ~10% than the total magnetic moment for iron (2.0 $\mu_B/atom$)[164]. As no spin and orbital

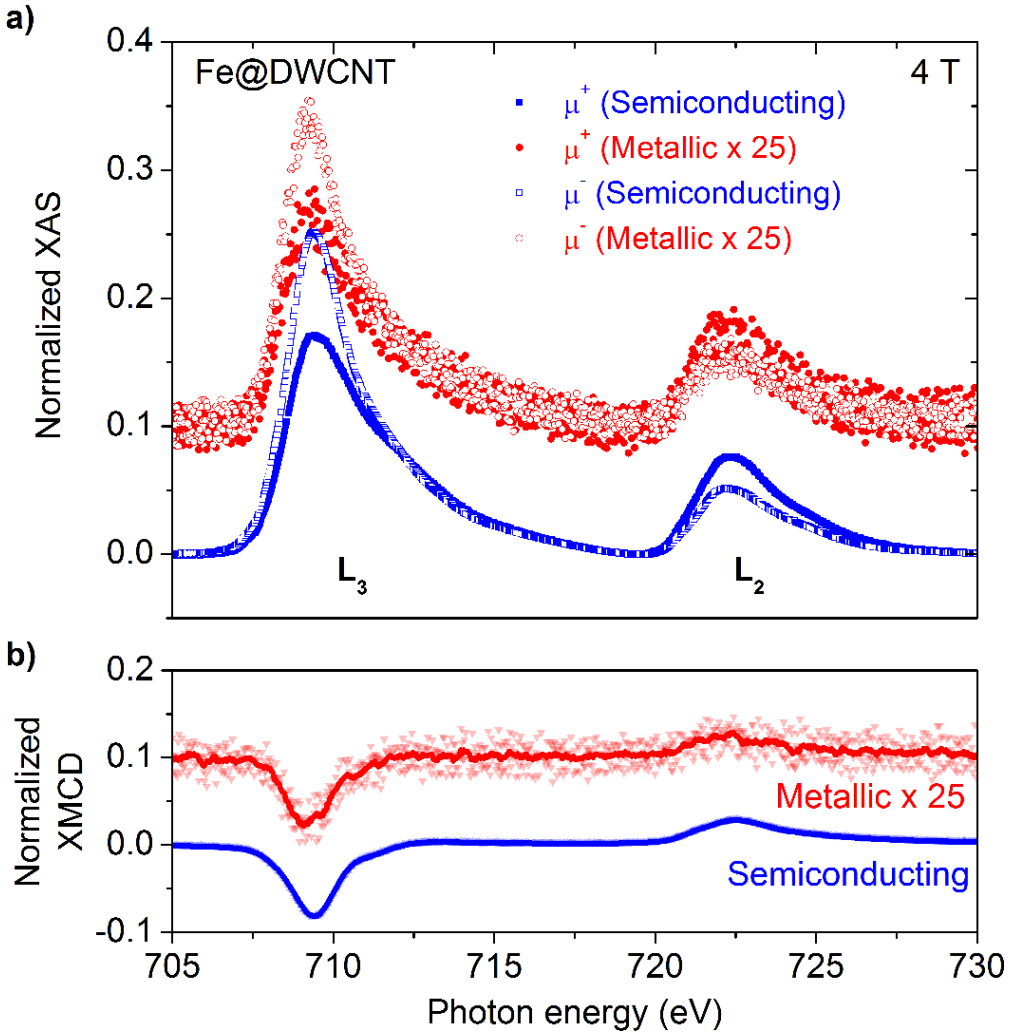

Figure 4.2: Observed XAS (a) and XMCD (b) response in the $L_{2,3}$ edge of Fe for the metallic and the semiconducting Fe_3C@SWCNT samples when a magnetic field of 4 T is applied to the sample at room temperature. All the spectra are offset by 0.1 and normalized by $\int(\mu^+ + \mu^-)/2$.

magnetic moments of cementite have been reported, we compare our $M_{L,S}$ data to the bulk iron values.

The obtained saturation values for the spin magnetic moments in the semiconducting (M_S=0.26 $\mu_B/atom$) and metallic (M_S=0.43 $\mu_B/atom$) $FeCp_2$@SWCNT samples are lower by ∼90% and ∼80%, respectively, than the value expected for bulk iron [164]. The reduced spin magnetic moment (m_S) in $FeCp_2$@SWCNT could be due to poor interactions between the adjacent Fe atoms, resulting in a low ordering of the spins. We could not obtain the M_L values for $FeCp_2$@SWCNT due to the small m_L almost linearly dependent on the magnetic field. This paramag-

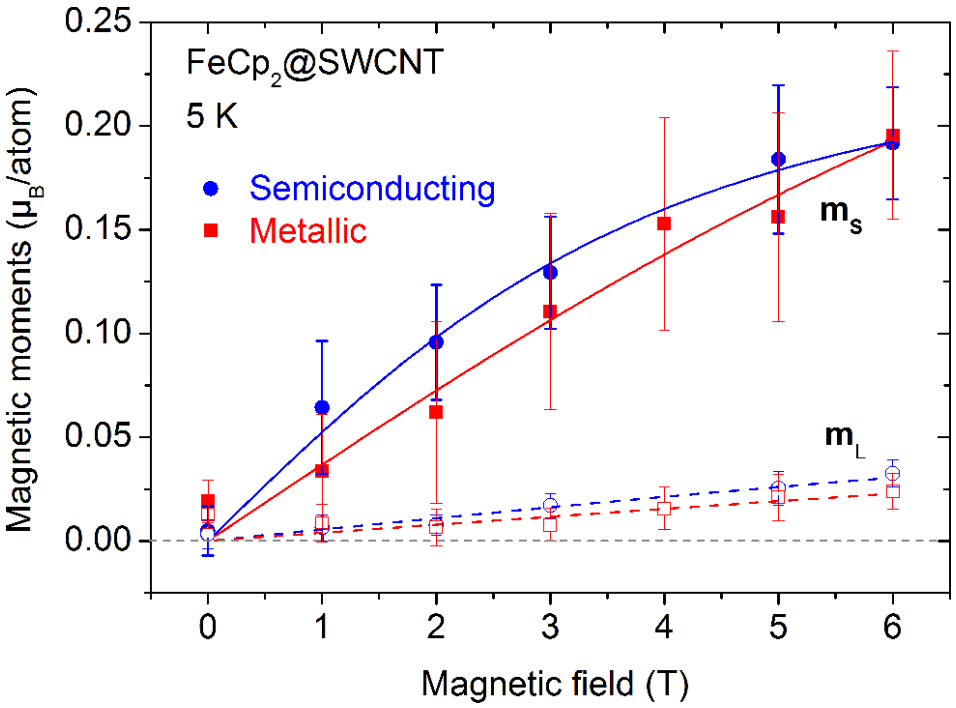

Figure 4.3: Spin and orbital magnetic moments of the metallic and semiconducting $FeCp_2$@SWCNT. The data are fitted with the modified Langevin function. The measurements were done at 5 K.

netic behavior at high magnetic fields is observed for the m_S too, and indicates low magnetic permeability of iron in $FeCp_2$@SWCNT.

By the transformation of the ferrocene to 1D Fe_3C inside the nanotubes, the iron 3d magnetic moments increase considerably, figure 4.2. The experimental data was fitted by the modified Langevin function (Eq. 4.1).

The saturation values of the spin magnetic moment for the semiconducting and metallic Fe_3C@SWCNT samples are M_S=1.38 and 1.19 $\mu_B/atom$, respectively. These values are lower by ∼30% and ∼40%, respectively, than the expected cementite values. The enhanced saturation value after annealing means that the spins get more ordered as the chemical status of the filling changes from ferrocene to the 1D cementite cluster. The difference between the two metalicity Fe_3C@SWCNT samples could be originating from the cluster size due to the filling degree and/or from the metallicity. Since the quantity of available iron atoms defines the mean length of the iron cluster formed inside the nanotube, the higher filling of the semiconducting sample leads to the formation of larger iron clusters which tend to have a greater spin ordering due to the size effect [174]. Alternatively, the enhanced metallicity of the SWCNT could also reduce the spin ordering in the encapsulated metal via scattering by conduction electrons. The saturation value for the orbital magnetic moments of iron in Fe_3C@SWCNT are M_L=0.086 and 0.084 $\mu_B/atom$ for semicon-

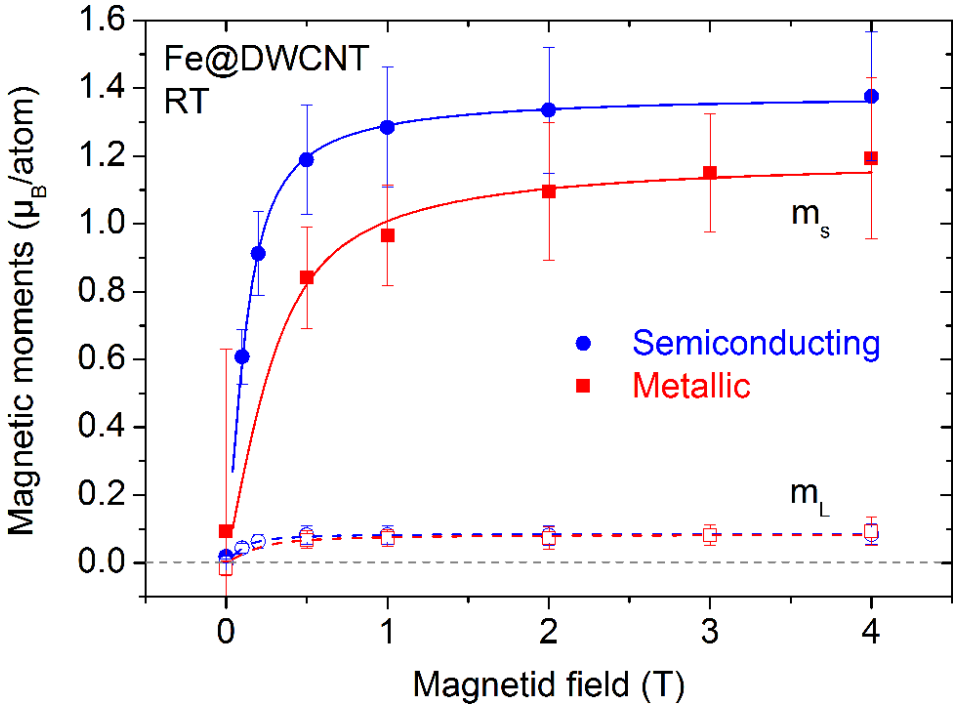

Figure 4.4: Spin and orbital magnetic moments of the metallic and semiconducting Fe_3C@SWCNT. The data are fitted with the modified Langevin function. The measurements were done at 300 K.

ducting and metallic, respectively, comparable to those reported for pure Fe (0.086 $\mu_B/atom$)[164] and the corresponding cementite value, with a very small difference between the two metallicity samples.

Table 4.1: Saturation values of the spin (M_S) and orbital (M_L) magnetic moments of metallic Fe [164] and fitting parameters, e. g., saturation magnetization ($M_{S,L}$) and uncompensated magnetic moment (μ_C) for the spin and orbital magnetic moments in $\mu_B/atom$, of the metallic (M) and semiconducting (SC) $FeCp_2$@SWCNT and Fe_3C@SWCNT

	Fe	Fitting param.	$FeCp_2$@SWCNT SC	$FeCp_2$@SWCNT M	Fe_3C@SWCNT SC	Fe_3C@SWCNT M
Spin	1.98	M_S	0.26	0.43	1.38	1.19
		μ_C	4.54	1.90	6552	2799
Orbital	0.086	M_L	-	-	0.086	0.084
		μ_C	-	-	8062	4343

4.2.3 Bulk magnetic moment

Another batch of metallicity sorted $FeCp_2$@SWCNT and Fe_3C@SWCNT were measured by SQUID in order to compare the "local" and the "bulk" character of the magnetic properties of these materials. The former refers to the magnetic moments strongly localised at the iron atoms while the latter stands for the sum of all magnetisms obtained by SQUID. By inspection of the RBM intensities of the inner tubes grown after the transformation relative filling degrees of $\sim$ 34% and $\sim$8% for the metallic and semiconducting samples, respectively, have been determined.

Figure 4.5 depicts the room temperature magnetisation curves for the semiconducting (blue) and metallic (red) samples measured at room temperature. The data for the $FeCp_2$@SWCNT and Fe_3C@SWCNT are the magnetisation subtracted by the reference data. The both empty SWCNT samples exhibit diamagnetism, figure 4.5(a). This changes to paramagnetism in the semiconducting $FeCp_2$@SWCNT while the magnetic response of the metallic $FeCp_2$@SWCNT remains diamagnetic, figure 4.5(a). The drastic change in the semiconducting sample can be attributed to the weak interaction between the SWCNT and $FeCp_2$, and the low filling degree.

When both aspects are present, the $FeCp_2$ molecules are electronically more isolated and possibly free to rotate inside the tubes. Under a magnetic field, these molecular magnets respond to exhibit the paramagnetic behaviour. In the case of the metallic sample the interaction between the $FeCp_2$ and SWCNT is stronger due to the higher metallicity, as well as between the adjacent $FeCp_2$ molecules due to the higher filling degree. This leads to more delocalised electrons over the sample, which can result in the enhanced diamagnetism as observed in the right panel in figure 4.5(a).

After the transformation to Fe_3C@SWCNT, the semiconducting sample stays paramagnetic. For the metallic sample, which has a filling degree higher by 23% than the semiconducting sample, a ferromagnetic behaviour is evident with a coercivity of 40 mT, figure 4.5(b). This ferromagnetism is thought to be enhanced due to the larger cementite cluster size and possibly the strong metallic character. The small coercivity value for the semiconducting sample means that the cementite nanoparticles hardly interact with each other and the spin alignment is poor owing to the smaller cluster size. Note that the magnetic moments obtained by SQUID are much larger than those obtained by XMCD, due to the "in bulk" character of the measurements in which the contributions of electron spins in the conduction band are observed. Hence, the remarkable differences between the filled metallic and semiconducting samples observed by SQUID are associated with the delocalized magnetisms which should be more sensitive to changes in SWCNT metallicity.

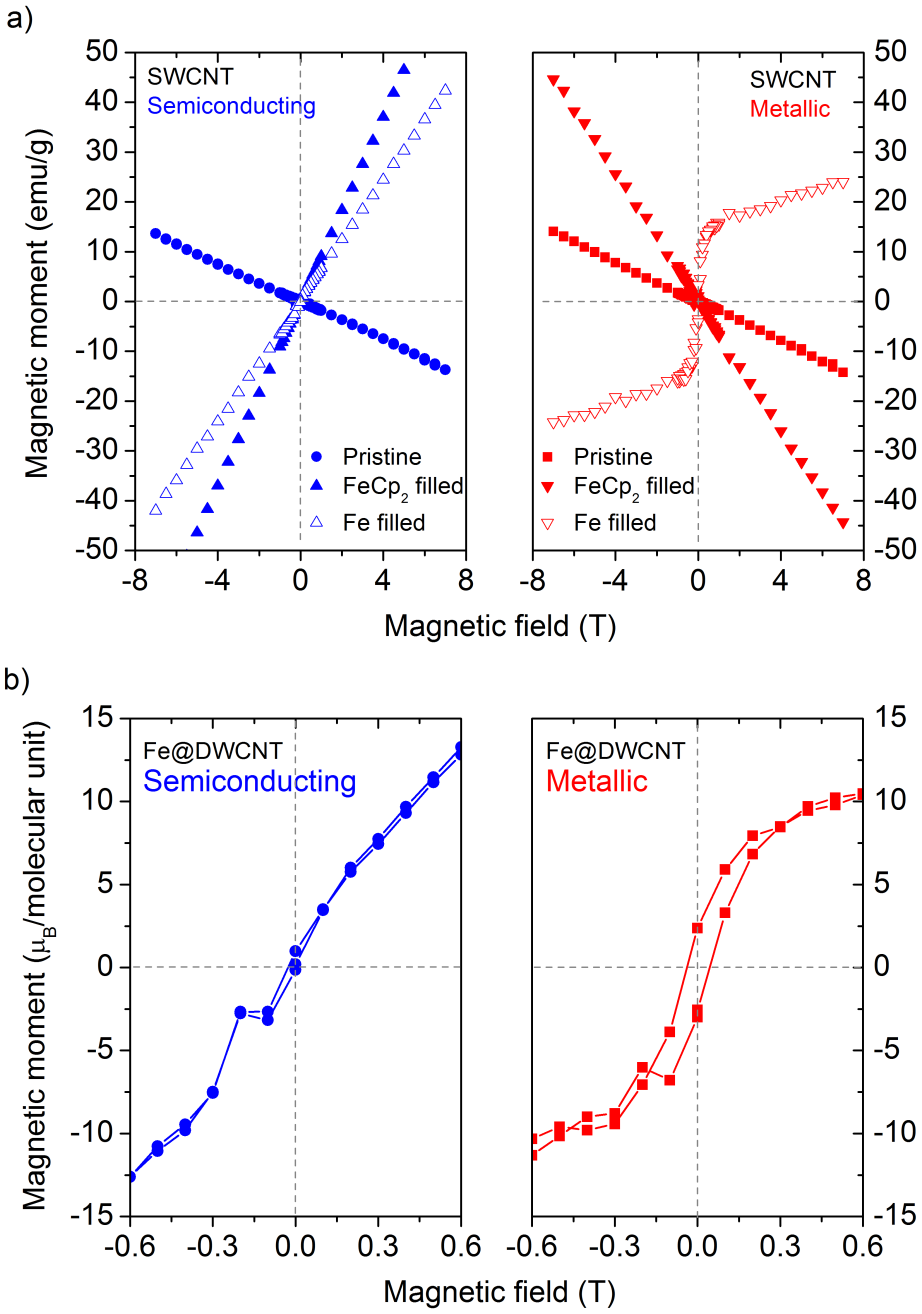

Figure 4.5: (a) Total magnetic moment measured by SQUID for empty semiconducting (left) and metallic (right) SWCNT, $FeCp_2$@SWCNT and Fe_3C@SWCNT. The magnetic moments were calculated per molecular unit with one Fe atom. The diamagnetic background of the pristine nanotubes were subtracted from the data of the Fe filled nanotubes. (b) Zoom in to the semiconducting (left) and metallic (right) Fe_3C@SWCNT. The metallic sample shows ferromagnetic behavior. The measurements were done at 300 K.

4.2.4 Structural characterization of encapsulated particles

Transmission electron microscopy (TEM) imaging was performed using an aberration-corrected JEOL-2200FS FEG TEM (Aalto University) operated at 80 kV. The samples were sonicated in acetone and the suspensions were cast onto a holey carbon grid. figure 4.6 reveal the metal nanoclusters created after the annealing in both the semiconducting (figure4.6(a-c)) and metallic nanotubes (figure4.6(d-f)). The high-resolution micrographs in panel c, e and f exhibit inner-tube structures being formed in the original tubes, as indicated by the arrows in panel c. The lower magnification micrographs in panel a, b and d show clearly the dimension of the encapsulated metal clusters. Note that these clusters have a diameter compared to the diameter corresponding to the encapsulating tubes, and they are elongated to around double their width. As shown in the previous TEM observations on similar samples [117], it has already been confirmed the cementite nature of the clusters, which catalyses the inner tube formation. This is consistent with the chemical characterization via XAS in the present study. These results prove that the ferrocene is encapsulated in the hollow space of the nanotubes and successively transformed into cementite clusters by annealing.

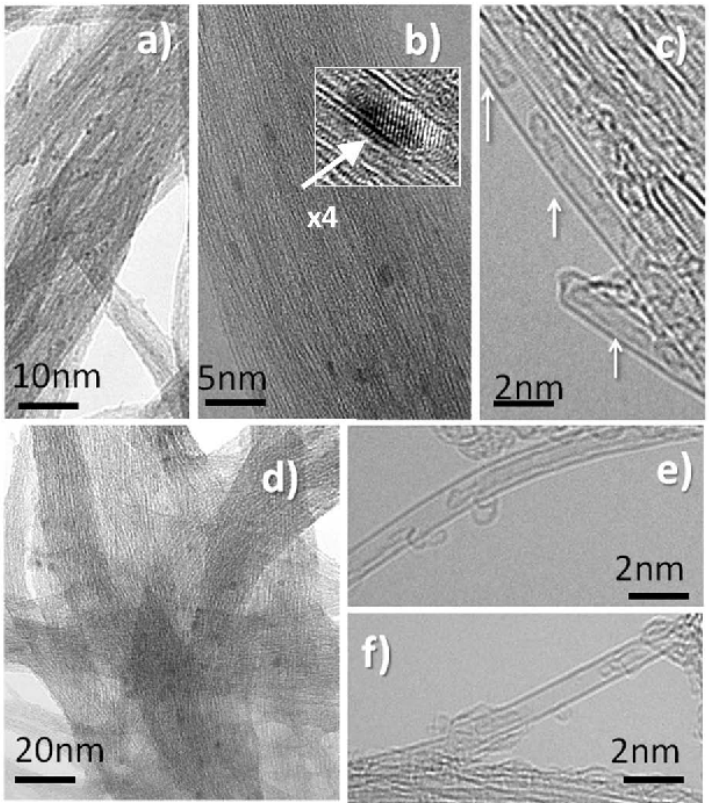

Figure 4.6: TEM micrographs of ferrocene filled semiconducting (a-c) and metallic (d-f) SWCNT after transformation.

4.3 Magnetism of Ni encapsulated in SWCNT

In the case of nickel encapsulated in SWCNTs, the magnetic properties were studied as function of annealing temperature and filling ratio.

4.3.1 Filling as proved by Raman spectroscopy

Three samples of Ni(II)Acac@SWCNT with three different filling degrees were prepared, via filling carried out for 1, 3 and 6 days. After filling the SWCNTs with Ni(II) acetylacetonate and annealing the samples in vacuum, the encapsulated molecules are transformed into metallic clusters encapsulated into SWCNT (Ni@SWCNT). The 6 days filled sample was annealed at two different temperatures 600°C and 800°C for 2 hrs. The rest of the samples were annealed only at 600°C for 2 hrs.

The filling of nanotubes is proved by Raman spectroscopy after annealing to transform the filled SWCNT to metallic clusters encapsulated inside DWCNT. In figure 4.7 the Raman spectra of different samples measured with a 1064 nm laser are shown. The spectra are normalized to the low frequency Raman lines, that corresponds to the RBM modes of the outer tubes. The pristine sample shows two main peaks at 147 and 160 cm^{-1} corresponding to tube diameters of 1.70 and 1.56 nm, respectively. Raman peaks at higher frequencies that appear after annealing correspond to the RBM of inner tubes. Two peaks are observed at 263 and 326 cm^{-1}, corresponding to inner tube diameters of 0.92 and 0.74 nm, respectively. As the spectra are normalized to the RBM of the outer tubes, we can associate the difference in intensity to the difference in filling degree, which depends on the duration of filling reaction. A correlation between the Raman intensities and the filling duration is observed.

4.3.2 XAS and XMCD

Figure 4.8 shows the normalized XAS spectra at the $L_{2,3}$ edge of Ni for the Ni(II)Acac@SWCNT before and after annealing at 600 and 800°C for 2 hours. Before annealing the XAS spectra shows peaks at 853.2, 855.1, 870.4 and 871.5 eV associated with the XAS spectra of the Ni(II) acetylacetonate molecule. After annealing at 600°C, the peaks at 855.1 and 871.5 eV start to vanish and the main peak at 853.2 eV shifts slightly to a lower energy. For the sample annealed at 800°C, both peaks 855.1 and 871.5 eV vanish completely and a new peak appears at 859.3 eV. This spectral shape corresponds to the XAS spectra of metallic Ni.

It is evident that the structural change of the encapsulated molecule is induced by nanochemical reactions during the annealing. At 800°C a metallic phase of Ni is obtained, while the filling is reduced as observed by Raman spectroscopy. This reduction in filling is attributed to some of filling materials released at high temperatures.

The relative Ni filling degree can also be estimated from the XAS spectra. Figure 4.9 shows the normalized XAS spectra of the 1, 3 and 6 days filled SWCNT samples annealed at 600°C for 2 hrs. The spectral shape of the three samples is practically

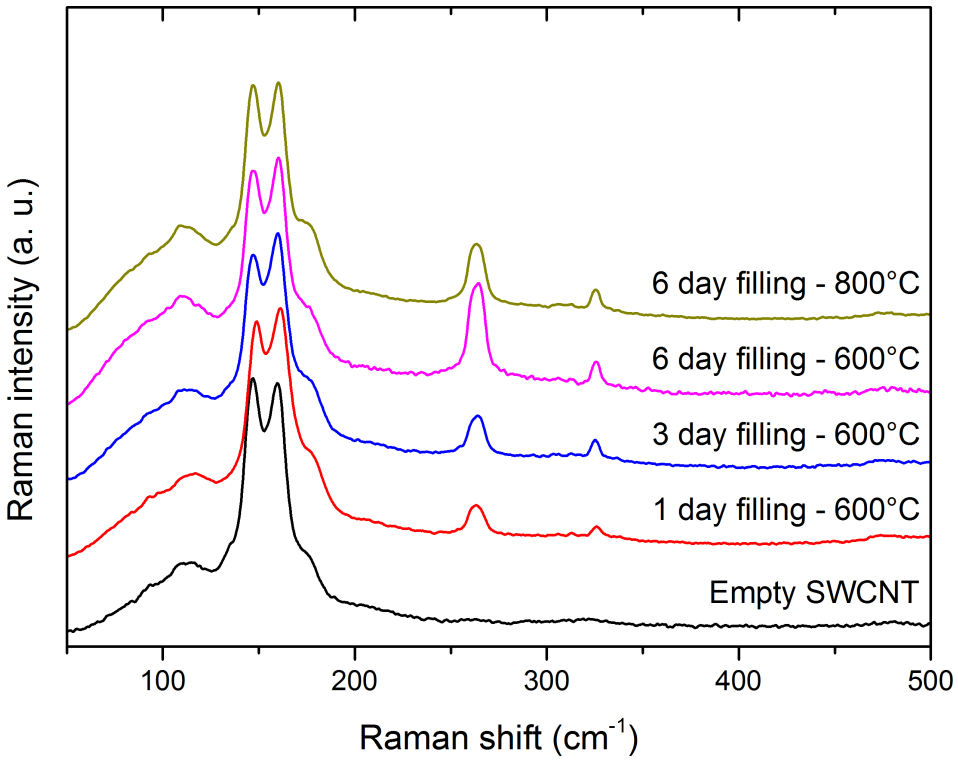

Figure 4.7: Raman spectra in the RBM frequencies of Ni(II) acetylacetonate encapsulated in eDIPS SWCNT for different filling ratios and annealing temperatures. The spectra were recorded with a 1064 nm laser wavelength.

the same. The Ni filling with respect to the 6 days filled sample are 27 and 36% for the 1 and 3 days filled samples, respectively. Table 4.2, summarizes the filling degree relative to the 6 days filled sample annealed at 600°C obtained from Raman and XPS. It is evident that the filling degree is increased with increasing the filling duration. Nevertheless, the longer the annealing duration, higher the filling obtained.

Table 4.2: Relative filling ratios estimated from Raman spectroscopy and XAS

Sample	Raman spectroscopy	XAS
1 day	27%	36%
3 days	42%	54%
6 days	100%	100%

Figure 4.10, shows the XAS and XMCD spectra of the 6 days filled sample before annealing and after annealing at 600°C and 800°C collected at 4 K at magnetic fields

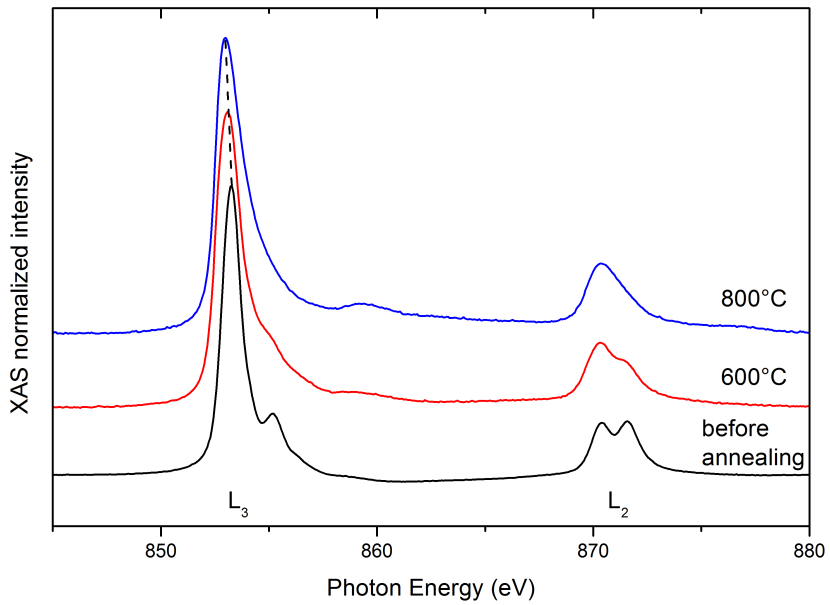

Figure 4.8: XAS at the Ni $L_{2,3}$ edge, for the Ni(II) acetylacetonate encapsulated in SWCNT before and after annealing at 600 and 800°C for 2hrs. The spectra are normalized to the L_3 peak.

from 0 to 6 T. As described above, the spectral shape of the Ni(II) acetylacetonate molecule is different from the one of metallic nickel, figure 4.10(a). The XMCD signal of the encapsulated molecule is increased linearly with increasing the magnetic field, figure 4.10(b). The 6 days filled sample annealed at 600°C shows the XMCD intensity that saturates at ∼1 T, figure 4.10(c-d). The same behavior is observed for the sample annealed at 800°C, figure 4.10(c-d), but the XMCD intensity at saturation is higher.

The spin m_S and orbital m_L magnetic moments calculated using equations 2.2 and 2.3 are plotted against the magnetic field in figure 4.11. As reported for bulk transition metals the orbital magnetic moment quenches with values below $0.1\mu_B$/atom. The spin magnetic moment varies between 0.35 and $0.60\mu_B$/atom. The spin magnetic moment of the encapsulated Ni(II) acetylacetonate show a linear behavior, while the annealed samples saturate at ∼1 T.

The total magnetic moment $(m_S + m_L)$ for all the samples is shown in figure 4.12. The data can be fitted with a modified Langevin function (equation 4.1) plus a linear contribution (χ), with an uncompensated magnetic moment (μ_C) of ∼200. The large uncompensated magnetic moment compared with that of ionic Ni, is a signature of superparamagnetism, which does not exhibit a clear sample dependence. As the filling duration increases, the saturation magnetization increases and the linear contribution is reduced. The 1 day filled sample shows the smallest

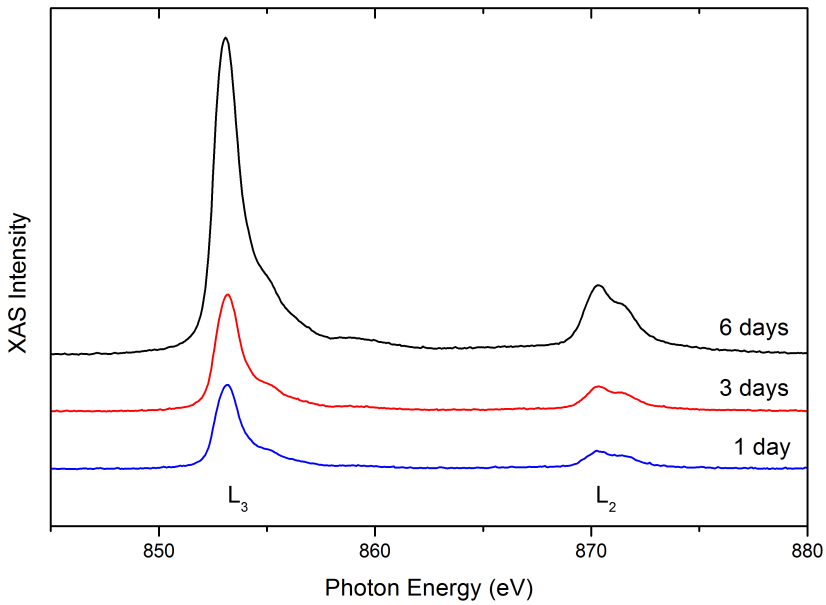

Figure 4.9: XAS at the Ni $L_{2,3}$ edge, for the 1, 3 and 6 days filled samples of Ni(II) acetylacetonate inside SWCNT after being annealed at 600°C for 2hrs.

saturation magnetization with the highest linear contribution. The 6 days filled sample annealed at 800°C shows the highest saturation magnetization with the lowest linear contribution. The sample before annealing shows a linear behavior (no saturation) associated with paramagnetism.

The contribution of the orbital magnetic moment to the total magnetic moment is less than 10%, with the spin magnetic moment governing the magnetic properties of these samples.

The fitting parameters of the Langevin function are shown in table 4.3. As discussed above the saturation magnetization is increased and the linear contribution is reduced with increasing the filling ratio. We attribute the saturating magnetization to the metallic Ni clusters and the linear contribution to the non-transformed Ni(II) acetylacetonate molecules in the sample. As observed in the XAS measurements, the encapsulated Ni(II) acetylacetonate molecule is fully transformed to encapsulated Ni clusters after anneal at 800°C. This explains the high saturation magnetization ($0.63\mu_B/atom$) that equals to the saturation magnetization of metallic Ni.

Figure 4.13 shows a temperature dependence of the total magnetic moment for the 6 days filled samples annealed at 600 and 800°C. Fitting these data with the modified Langevin equation as a function of temperature gives different parameters than in the case of the isotherm plots. This variation can be explained in terms of an antiferromagnetic contribution to the magnetism. The inverse plot, depicted in the inset of figure 4.13, shows Curie-Weiss behavior with Weiss temperatures of

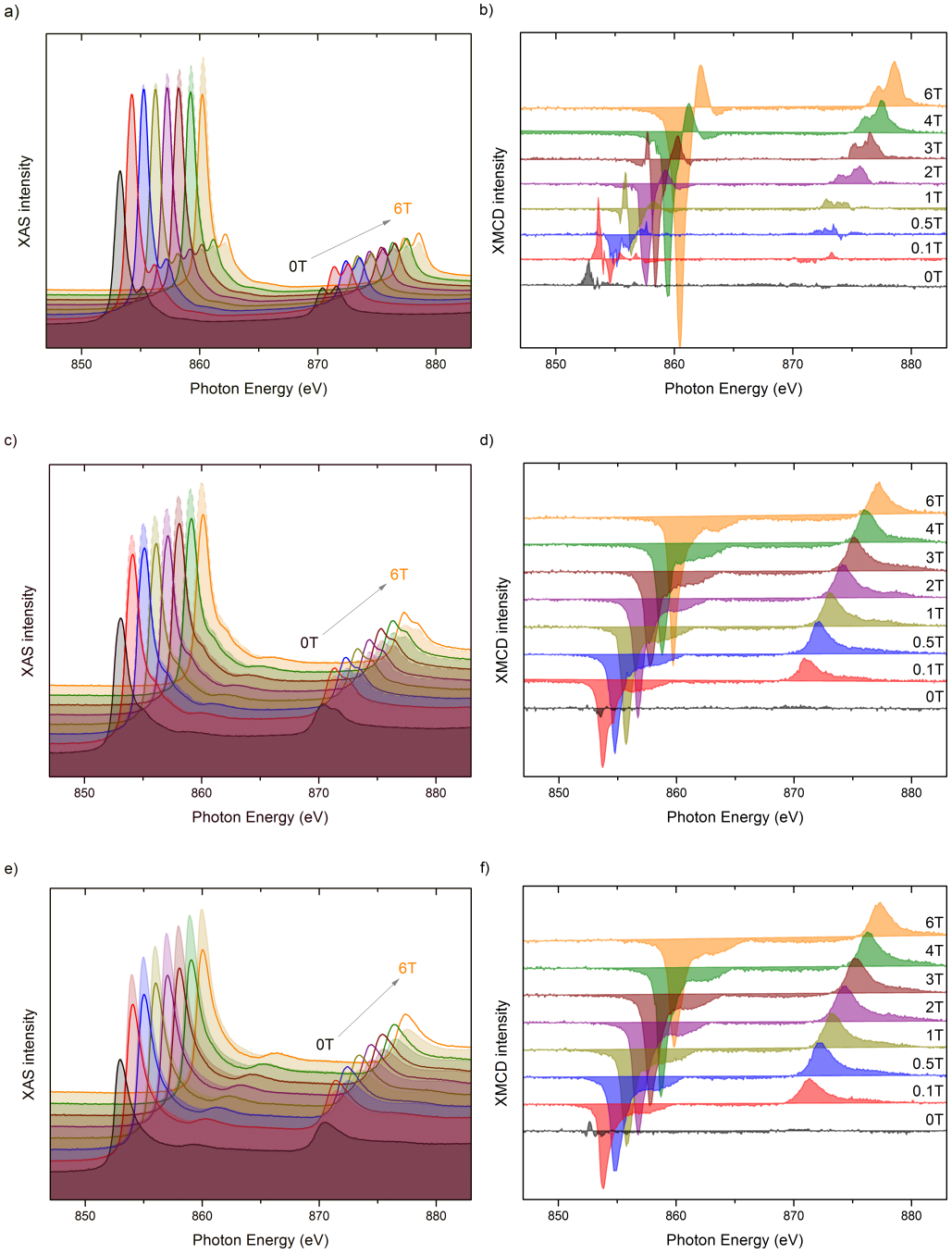

Figure 4.10: Observed (a,c,e) XAS and (b,d,f)XMCD in the $L_{2,3}$ edge of Ni, for the Ni(II) acetylacetonate encapsulated in SWCNT (a,b) before and after annealing at (c,d) 600ºC and (e,f) 800ºC at magnetic fields from 0 to 6 T. The spectra are offset one another in X axis by 1 eV.

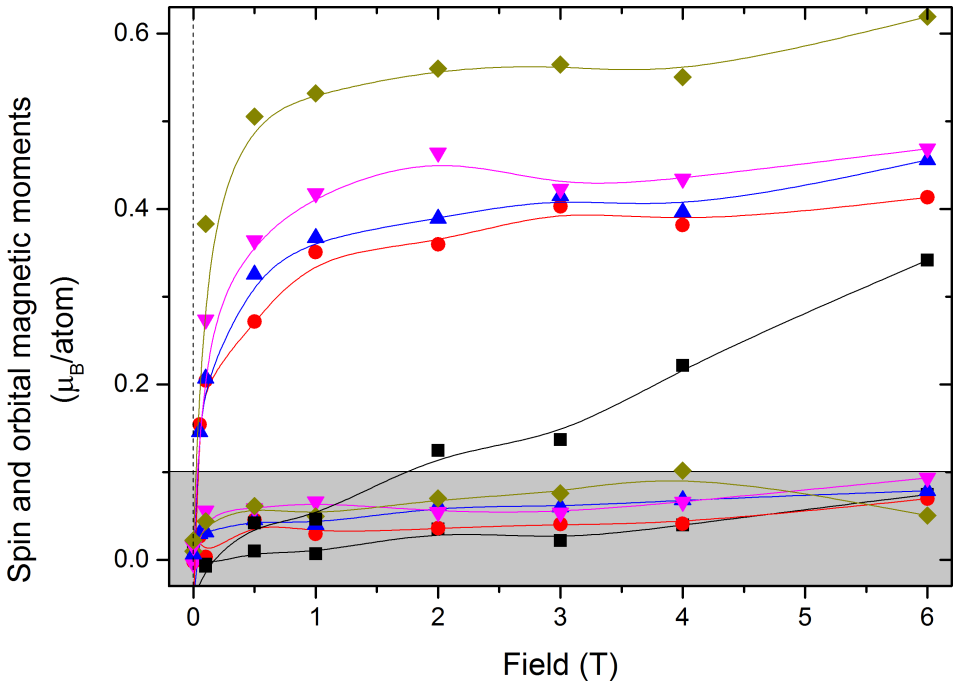

Figure 4.11: Spin and orbital magnetic moments calculated through the XMCD sum rules for the Ni(II) acetylacetonate encapsulated in SWCNT before annealing (square), 1 day filled annealed at 600°C (circle), 3 days filled annealed at 600°C (up arrow), 6 days filled annealed at 600°C (down arrow) and 6 days filled annealed at 800°C (diamond).

Table 4.3: Fitting Langevin parameters for the 1, 3, and 6 days filled Ni(II)Acac@SWCNT after annealing

Sample	M_S (μ_B/atom)	μ_C	χ
1d 600°C	0.33	194.94	0.027
3d 600°C	0.39	176.52	0.025
6d 600°C	0.46	211.50	0.014
6d 800°C	0.60	195.02	0.012

~300 and ~150 K for the samples annealed at 600 and 800°C, respectively.

4.3.3 Bulk magnetic moments

Figure 4.14 shows the SQUID data of the 3 and 6 days filled samples annealed at 600°C recorded at 5 and 300 K. The diamagnetic background of the empty SWCNTs (solid diamonds) was subtracted from the data. Both samples show hysteresis at low temperature (solid circles), but no hysteresis at room temperature (empty circles).

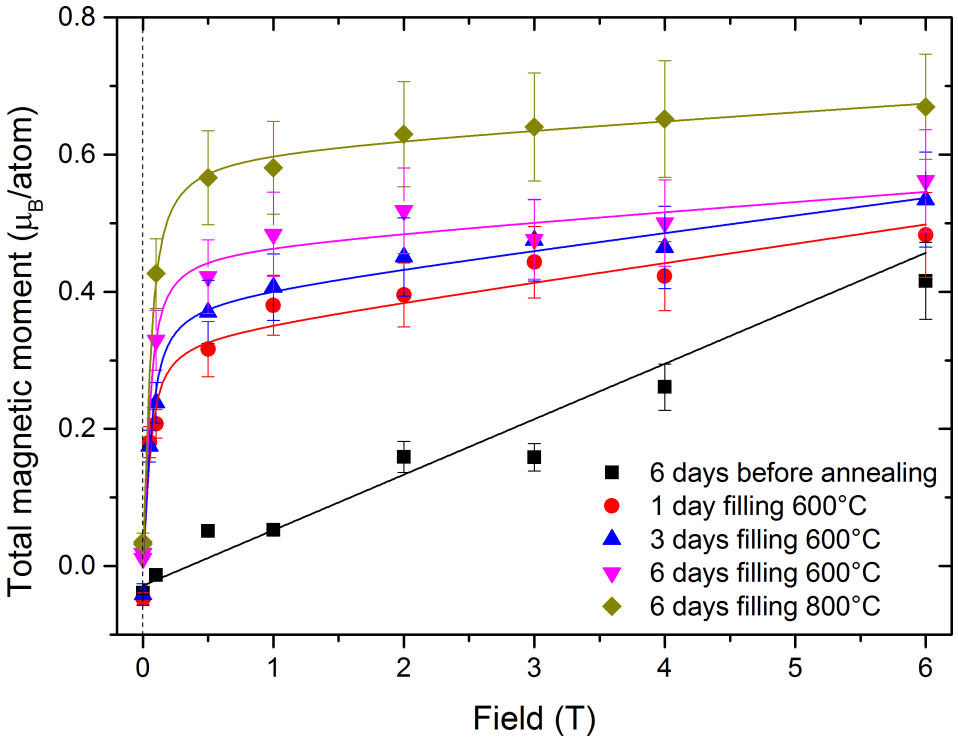

Figure 4.12: Total magnetic moments for the Ni(II) acetylacetonate encapsulated in SWCNT before annealing (square), 1 day filled annealed at 600°C (circle), 3 days filled annealed at 600°C (up arrow), 6 days filled annealed at 600°C (down arrow) and 6 days filled annealed at 800°C (diamond).

This suggests a superparamagnetic behavior of the annealed samples with a blocking temperature in between . The SQUID signal of the 1 day filled sample is too weak to be analysed (not shown). Coercivity values of ∼140 and ∼80 mT (dashed lines), are observed on the 3 and 6 days filled samples, respectively. The saturation magnetization also increases with the filling degree, in agreement with the XMCD data.

In the case of the samples annealed at different temperatures, the SQUID data show a different behavior than that observed in the XMCD measurements. In contrast with the XMCD data, the saturation magnetization in the SQUID measurements is lower for the sample annealed at 800°C than the sample annealed at 600°C. This difference can be associated with the amount of metallic clusters encapsulated in the nanotubes. As observed by Raman spectroscopy and XAS part of the Ni particles goes out of the tube at 800°C, reducing the amount of encapsulated particles. This can also explain the higher diamagnetic contribution of the nanotubes in the sample as shown in the inset of figure 4.14. The coercivity is similar for both samples with a value of ∼140 mT. Both samples show no hysteresis at room temperature.

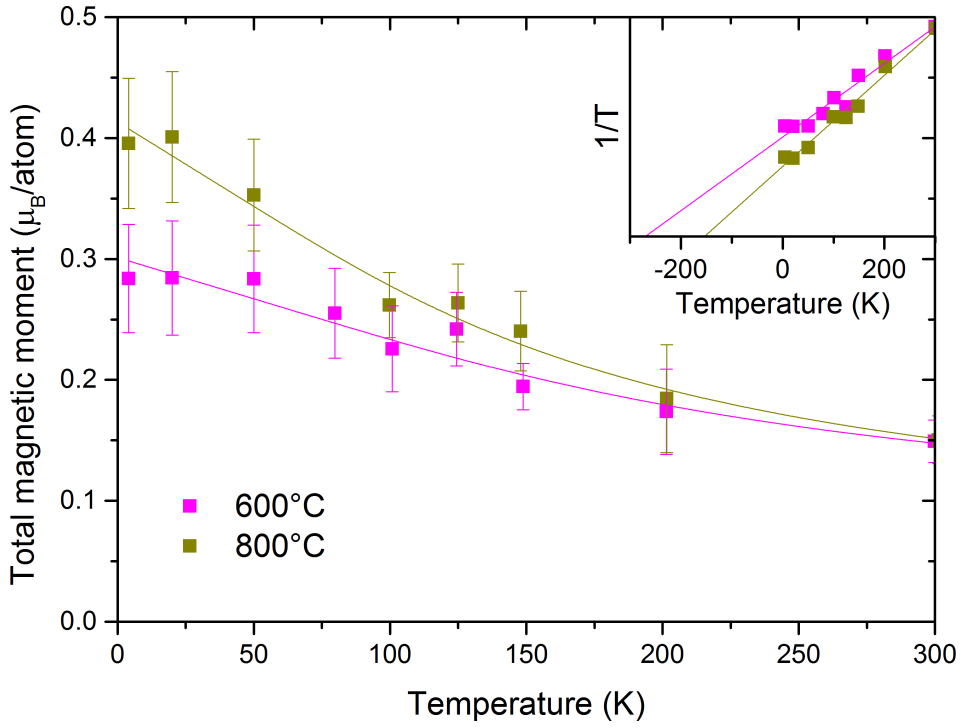

Figure 4.13: Total magnetic moments for the Ni(II) acetylacetonate encapsulated in SWCNT before annealing (square), 1 day filled annealed at 600°C (circle), 3 days filled annealed at 600°C (up arrow), 6 days filled annealed at 600°C (down arrow) and 6 days filled annealed at 800°C (diamond).

4.3.4 Size of encapsulated Ni clusters evaluated by XRD

Structural information of the encapsulated metallic clusters can be extracted from XRD measurements.

Figure 4.15 shows the XRD for empty SWCNTs, 6 days filled sample before annealing, 1, 3 and 6 days filled sample annealed at 600°C and 6 days filled sample annealed at 800°C. All the curves are normalized to the intensity of the broad peak at a low q value, that correspond to a diffraction peak related with the SWCNT bundles [175]. The empty SWCNTs (pristine) and the 6 days filled before annealing show a peak whose position is in good agreement with the peak for bcc Fe(110) (dashed line). This is an indication of remaining catalytic particles in the samples. Note that the remaining Fe particles do not contribute to the magnetism of the samples as the empty SWCNT was observed diamagnetic (figure 4.14(top)).

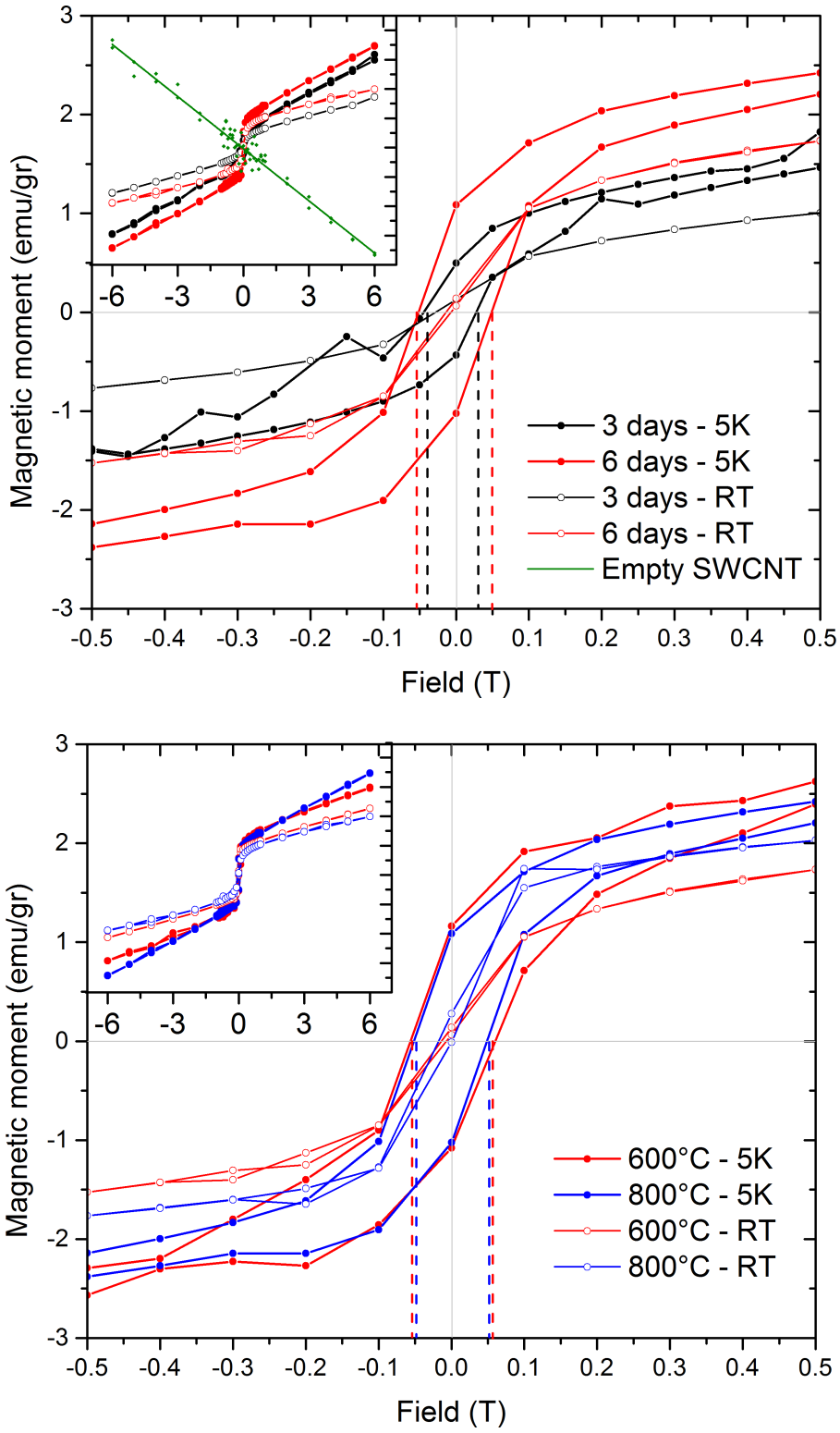

Figure 4.14: M-H plot of Ni@SWCNT as function of (top) filling duration and (bottom) annealing temperature. The data were recorded at 5K (solid circles) and room temperature (empty circles). The coercivity values for the samples are shown in dashed lines. The inset shows the magnetization at higher magnetic fields. The diamagnetic background from the empty SWCNT (green diamonds) was subtracted from the SQUID data.

The samples after the annealing process, show a broad peak near to the bcc Fe(110) (dashed line) and a peak at $\sim$30.96 nm^{-1} assigned to fcc Ni(111) (dotted line). The sample annealed at 800°C shows a narrower fcc Ni(111) peak and also at $\sim$35.73 nm^{-1} assigned to fcc Ni(200) (dotted line).

The XRD data at the bcc Fe(110) and fcc Ni(111) is shown in figure 4.15. The data for empty tubes and the sample before annealing were fitted with a Gaussian, located at $\sim$30.2 nm^{-1}. The rest of the samples were fitted with two Gaussian, the γ-Fe peak and the Ni (111) peak. The peak positions are shifted slightly due to different scattering geometries. The remaining catalytic Fe particles do not contribute to the magnetism of the samples as was observed in the diamagnetism measured by SQUID on empty nanotubes.

To find the relationship between the magnetism of the Ni clusters and their size, a detailed inspection of the Ni (111) peak is carried out. It is possible to determine the approximate size of the encapsulated cluster by analysing the Gaussian parameter of the Ni (111) peak for each sample. From the averaged line width ($\triangle q$) of a diffraction pattern a cluster size is deduced through the Scherrer equation (equation 2.4).

As the diameter of the nanotube confines the size of the particle, we can consider the calculated cluster size as the length of the 1D metallic cluster encapsulated into the SWCNTs. The Gaussian area intensity and width for the Fe(110) and Ni(111) peaks and the calculated length of the 1D metallic cluster are shown in table 4.4. The encapsulated cluster is increased in size by increasing the filling duration and/or the annealing temperature.

The magnetic properties of the 1D metallic cluster formed into SWCNTs are clearly dependent on the cluster size. In figure 4.16, the Langevin parameters for the 1, 3 and 6 days filled samples annealed at 600°C and the 6 days filled sample annealed at 800°C are shown as function of the cluster size extracted from the XRD data.

The saturation magnetization M_S increases linearly with the cluster size. The 6 days filled sample annealed at 800°C is the only sample that shows both the Ni (111) and Ni(200) peaks. This sample also shows the highest saturation magnetization with a value close to the value for metallic Ni ($\sim$0.65μ_B/atom) [176].

As discussed above the high values of the uncompensated magnetic moments μ_C are a signature of paramagnetism and do not depend on the cluster size.

In the case of the linear term χ, this also changes with the cluster size. It is observed in figure 4.16 bottom-panel, that the magnitude of the linear component decreases as the cluster size increases. This is associated to the paramagnetic nature of small clusters and/or to the amount of Ni(II) acetylacetonate molecules that remain in the SWCNTs. At higher temperatures more molecules are decomposed and transformed to metallic clusters and inner tubes, this explains the lowest value for the sample annealed at 800°C.

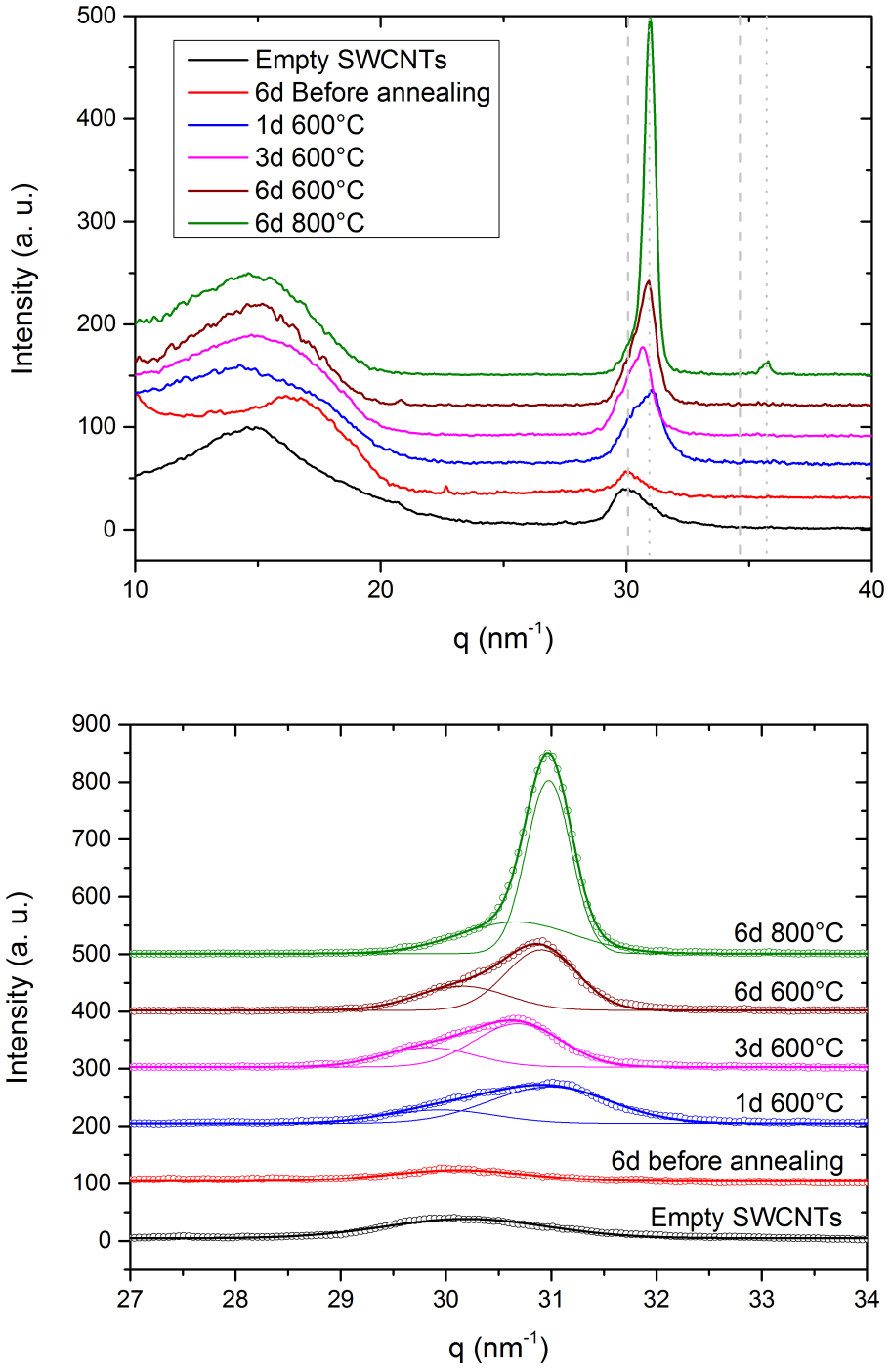

Figure 4.15: XRD of the pristine SWCNT and the Ni(II) acetylacetonate filled SWCNT before and after annealing. The dashed dotted lines correspond to γ-Fe and Ni peaks. The data was normalized to the short range peak. The bottom panel shows the XRD data fitted by Gaussian curves for the γ-Fe and the Ni (111) peaks.

Table 4.4: Gaussian parameters for the bcc Fe(110) and fcc Ni(111) of the empty SWCNTs, 6 days filled sample before annealing, the 1, 3, and 6 days filled samples annealed at 600°C and the 6 days sample annealed at 800°C

Sample	bcc Fe(110)		fcc Ni(111)		Cluster size (nm)
	Area	Width	Area	Width	
Empty SWCNT	65.48	1.55			
6d before annealing	30.01	1.27			
1d 600°C	30.51	1.03	91.40	1.15	4.91
3d 600°C	36.92	0.87	78.32	0.82	6.93
6d 600°C	45.62	0.86	90.17	0.68	8.37
6d 800°C	74.41	1.08	160.2	0.52	11.32

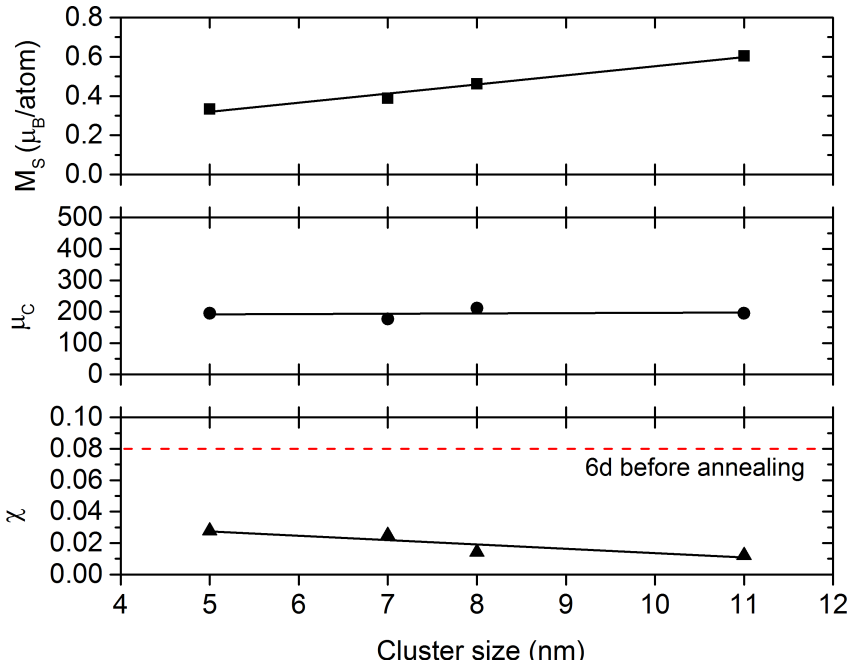

Figure 4.16: Langevin parameters plotted against the cluster size. The dashed line shows the slope of the linear contribution for the Ni(II) acetylacetonate encapsulated in SWCNTs.

As it is observed in table 4.4, the Gaussian parameters for the Fe(110) peak do not change significantly. From this we can conclude that the magnetic behavior of the samples depends only on the encapsulated Ni clusters.

This study shows a potential to tune the magnetic properties of low-dimensional metallic clusters encapsulated in SWCNTs by controlling the filling ratio and the annealing temperature.

Chapter 5

Summary and Outlook

5.1 Laser annealing and laser assisted CVD

The use of laser for fast and local annealing has been proved for both the transformation of organometallic molecules encapsulated in SWCNT to DWCNT by nanochemical reactions, and for the synthesis of carbon nanotubes in small areas on powder and flat substrates.

The laser annealing provides a rapid and local way to transform the encapsulated molecules into metallic clusters and inner tubes. $FeCp_2$@SWCNT has been transformed to Fe carbide and DWCNTs in a microscopic area in less than one minute by heating with a focused laser. The area of transformation can be as small as $10\,\mu$m.

In the case of the laser-assisted CVD, carbon nanotubes were succesfully grown in a small area in predefined substrates. Multilayer catalysts (MLC) with different compositions were used in order to study the effect of the thermal conductivity of the support layer in the laser-assisted CVD process. The growth of carbon nanotubes is achieved in less than 5 sec, with a spot size of $\sim 10\,\mu$m. Changes in the focus allows a more sensitive control of the laser heating induced to the multilayer catalyst.

Hybrid systems of functionalized carbon nanostructures can be fabricated by LA-CVD for possible use as sensors or electronic devices. Further optimizations are needed to improve the yield and purity. Different compositions of MLC need to be tested in order to grow aligned SWCNT by the LA-CVD process.

5.2 Magnetic properties of encapsulated 1D metallic clusters

Single-walled carbon nanotubes have been filled with different organometallic compounds in order to study their magnetic properties. Ferrocene and Ni (II) acetylacetonates have been studied in detail in this work. The protection provided by the nanotube allows to study this hybrid structures without the formation of metallic oxides.

Ferrocene filled metallicity separated SWCNTs have been used to study the influence of the metallicity of the tubes on the magnetic properties of the encapsulated metallic clusters. In the case of metallic tubes, their metallic character enhance the ferromagnetic behavior of the encapsulated clusters. The semiconducting tubes does not show the same behavior.

A detailed study of the magnetic moments as function of filling duration and annealing temperature has been carried out on SWCNTs encapsulating Ni(II) acety-

lacetonate. Filled SWCNTs were annealed to transform the Ni(II) acetylacetonate into metallic clusters. Raman spectroscopy has been used to prove the filling and transformation of the filled nanotubes. Raman spectroscopy and XAS measurements show a clear relationship between the filling degree and the filling duration.

The spin and orbital magnetic moments have been calculated from XMCD measurements. As it is common for transition metals, the orbital magnetic moment quenches and the spin magnetic moment dictates the magnetism of the cluster inside the nanotubes. The magnetic moments are also affected by the filling degree. Higher magnetic moments were observed after annealing at higher temperatures.

The size of the encapsulated cluster can be measured by XRD measurements. It has been found that the size of the clusters is proportional to the filling duration and possibly to the annealing temperature. The magnetic properties of metallic clusters grown inside SWCNTs can be tuned by the cluster size that is controlled by filling and annealing.

The results obtained in this study show potential for 1) patterned growth of aligned SWCNTs on predefined substrates, and 2) control of magnetization of 1D metallic clusters encapsulated in SWCNTs. The filling of aligned SWCNTs leads to interesting anisotropic magnetic properties due to the anisotropy of carbon nanotubes. A thorough understanding of all the processes involved in this study is indispensable for this hybrid structures to be used in future applications in bio- and material-technologies and spintronics.

Bibliography

[1] H. W. Kroto, J. R. Heath, S. C. Obrien, R. F. Curl, and R. E. Smalley, "C-60 - buckminsterfullerene," *Nature*, vol. 318, no. 6042, pp. 162–163, 1985.

[2] S. Iijima, "Helical microtubules of graphitic carbon," *Nature*, vol. 354, pp. 56–58, 1991.

[3] S. Iijima and T. Ichihashi, "Single-shell carbon nanotubes of 1-nm diameter," *Nature*, vol. 363, pp. 603–605, 1993.

[4] L. X. Zheng, M. J. O'Connell, S. K. Doorn, X. Z. Liao, Y. H. Zhao, E. A. Akhadov, M. A. Hoffbauer, B. J. Roop, Q. X. Jia, R. C. Dye, D. E. Peterson, S. M. Huang, J. Liu, and Y. T. Zhu, "Ultralong single-wall carbon nanotubes," *Nature Materials*, vol. 3, pp. 673–676, Oct. 2004.

[5] M. Dresselhaus, G. Dresselhaus, and P. Eklund, *Science of Fullerenes and Carbon Nanotubes*. Academic Press Inc. San Diego, 1996.

[6] M. S. Dresselhaus and P. C. Eklund, "Phonons in carbon nanotubes," *Advances in Physics*, vol. 49, no. 6, pp. 705–814, 2000.

[7] A. Krishnan, E. Dujardin, T. W. Ebbesen, P. N. Yianilos, and M. M. J. Treacy, "Young's modulus of single-walled nanotubes," *Phys. Rev. B*, vol. 58, pp. 14013–14019, Nov 1998.

[8] B. I. Yakobson, C. J. Brabec, and J. Bernholc, "Nanomechanics of carbon tubes: Instabilities beyond linear response," *Phys. Rev. Lett.*, vol. 76, pp. 2511–2514, Apr 1996.

[9] J. W. Mintmire, B. I. Dunlap, and C. T. White, "Are fullerene tubules metallic?," *Phys. Rev. Lett.*, vol. 68, pp. 631–634, Feb 1992.

[10] N. Hamada, S.-i. Sawada, and A. Oshiyama, "New one-dimensional conductors: Graphitic microtubules," *Phys. Rev. Lett.*, vol. 68, pp. 1579–1581, Mar 1992.

[11] S. Saito, "Carbon nanotubes for next-generation electronics devices," *Science*, vol. 278, no. 5335, pp. 77–78, 1997.

[12] E. Gal'pern, I. Stankevich, A. Chistykov, and L. Chernozatonskii, "Carbon nanotubes with metal inside: electron structure of tubelenes [Li@C24]n and [K@C36]n," *Chemical Physics Letters*, vol. 214, pp. 345 – 348, 1993.

[13] Y. Chen, R. C. Haddon, S. Fang, A. M. Rao, W. H. Lee, E. C. Dickey, E. A. Grulke, J. C. Pendergrass, A. Chavan, B. E. Haley, and R. E. Smalley, "Chemical attachment of organic functional groups to single-walled carbon nanotube material," *Journal of Materials Research*, vol. 13, no. 9, pp. 2423–2431, 1998.

[14] M. M. J. Treacy, T. W. Ebbesen, and J. M. Gibson, "Exceptionally high Young's modulus observed for individual carbon nanotubes," *Nature*, vol. 381, pp. 678–680, 1996.

[15] R. Saito, G. Dresselhaus, and M. S. Dresselhaus, *Physical properties of carbon nanotubes*. Imperial College Press, 1998.

[16] P. Ajayan and O. Zhou, "Applications of carbon nanotubes," in *Carbon Nanotubes* (M. Dresselhaus, G. Dresselhaus, and P. Avouris, eds.), vol. 80 of *Topics in Applied Physics*, pp. 391–425, Springer Berlin Heidelberg, 2001.

[17] R. H. Baughman, A. A. Zakhidov, and W. A. de Heer, "Carbon nanotubes-the route toward applications," *Science*, vol. 297, no. 5582, pp. 787–792, 2002.

[18] R. Saito and H. Kataura, *Carbon Nanotubes*, vol. 80 of *Topics in Applied Physics*, review Optical properties and Raman spectroscopy of carbon nanotubes, pp. 213–246. Springer-Verlag Berlin, 2001.

[19] X. Liu, *Electronic structure and excited states of pristine and intercalated single-wall carbon nanotubes*. PhD thesis, Fakultät Mathematik und Naturwissenschaften, Technischen Universität Dresden, 2003.

[20] A. Briones-Leon, X. J. Liu, C. Kramberger, T. Saito, and T. Pichler, "Nanochemical reactions by laser annealing of ferrocene filled single-walled carbon nanotubes," *Physica Status Solidi B*, vol. 248, pp. 2488–2491, Nov. 2011.

[21] A. Briones-Leon, X. Liu, P. Ayala, H. Kataura, K. Yanagi, E. Weschke, T. Pichler, and H. Shiozawa, "Orbital and spin magnetic moments of ferrocene encapsulated in metallicity sorted single-walled carbon nanotubes," *Physica Status Solidi B*, vol. 249, no. 12, pp. 2424–2427, 2012.

[22] A. Briones-Leon, P. Ayala, X. Liu, K. Yanagi, E. Weschke, M. Eisterer, H. Jiang, H. Kataura, T. Pichler, and H. Shiozawa, "Orbital and spin magnetic moments of transforming one-dimensional iron inside metallic and semiconducting carbon nanotubes," *Phys. Rev. B*, vol. 87, p. 195435, May 2013.

[23] T. Belin and F. Epron, "Characterization methods of carbon nanotubes: a review," *Materials Science and Engineering: B*, vol. 119, no. 2, pp. 105 – 118, 2005.

[24] R. Saito, G. Dresselhaus, and M. S. Dresselhaus, "Trigonal warping effect of carbon nanotubes," *Phys. Rev. B*, vol. 61, pp. 2981–2990, Jan 2000.

[25] D. S. Bethune, C. H. Klang, M. S. de Vries, G. Gorman, R. Savoy, J. Vazquez, and R. Beyers, "Cobalt-catalysed growth of carbon nanotubes with single-atomic-layer walls," *Nature*, vol. 363, pp. 605–607, 1993.

[26] C. Journet, W. K. Maser, P. Bernier, A. Loiseau, M. L. delaChapelle, S. Lefrant, P. Deniard, R. Lee, and J. E. Fischer, "Large-scale production of single-walled carbon nanotubes by the electric-arc technique," *Nature*, vol. 388, no. 6644, pp. 756–758, 1997.

[27] T. Guo, P. Nikolaev, A. Thess, D. Colbert, and R. Smalley, "Catalytic growth of single-walled manotubes by laser vaporization," *Chemical Physics Letters*, vol. 243, pp. 49 – 54, 1995.

[28] A. Thess, R. Lee, P. Nikolaev, H. Dai, P. Petit, J. Robert, C. Xu, Y. H. Lee, S. G. Kim, A. G. Rinzler, D. T. Colbert, G. E. Scuseria, D. Tománek, J. E. Fischer, and R. E. Smalley, "Crystalline ropes of metallic carbon nanotubes," *Science*, vol. 273, no. 5274, pp. 483–487, 1996.

[29] O. Jost, A. A. Gorbunov, W. Pompe, T. Pichler, R. Friedlein, M. Knupfer, M. Reibold, H.-D. Bauer, L. Dunsch, M. S. Golden, and J. Fink, "Diameter grouping in bulk samples of single-walled carbon nanotubes from optical absorption spectroscopy," *Applied Physics Letters*, vol. 75, no. 15, pp. 2217–2219, 1999.

[30] M. H. Rummeli, E. Borowiak-Palen, T. Gemming, T. Pichler, M. Knupfer, M. Kalbac, L. Dunsch, O. Jost, S. R. P. Silva, W. Pompe, and B. Buchner, "Novel catalysts, room temperature, and the importance of oxygen for the synthesis of single-walled carbon nanotubes," *Nano Letters*, vol. 5, pp. 1209–1215, July 2005.

[31] M. Jose-Yacaman, M. Miki-Yoshida, L. Rendon, and J. G. Santiesteban, "Catalytic growth of carbon microtubules with fullerene structure," *Applied Physics Letters*, vol. 62, pp. 657–659, 1993.

[32] Z. F. Ren, Z. P. Huang, J. W. Xu, J. H. Wang, P. Bush, M. P. Siegal, and P. N. Provencio, "Synthesis of large arrays of well-aligned carbon nanotubes on glass," *Science*, vol. 282, no. 5391, pp. 1105–1107, 1998.

[33] S. Fan, M. G. Chapline, N. R. Franklin, T. W. Tombler, A. M. Cassell, and H. Dai, "Self-oriented regular arrays of carbon nanotubes and their field emission properties," *Science*, vol. 283, no. 5401, pp. 512–514, 1999.

[34] H. Dai, J. H. Hafner, A. G. Rinzler, D. T. Colbert, and R. E. Smalley, "Nanotubes as nanoprobes in scanning probe microscopy," *Nature*, vol. 384, no. 6605, pp. 147–50, 1996.

[35] P. Nikolaev, M. J. Bronikowski, R. Bradley, F. Rohmund, D. T. Colbert, K. Smith, and R. E. Smalley, "Gas-phase catalytic growth of single-walled carbon nanotubes from carbon monoxide," *Chemical Physics Letters*, vol. 313, pp. 91 – 97, 1999.

[36] H. Dai, A. G. Rinzler, P. Nikolaev, A. Thess, D. T. Colbert, and R. E. Smalley, "Single-wall nanotubes produced by metal-catalyzed disproportionation of carbon monoxide," *Chemical Physics Letters*, vol. 260, pp. 471 – 475, 1996.

[37] J. Kong, H. T. Soh, A. M. Cassell, C. F. Quate, and H. Dai, "Synthesis of individual single-walled carbon nanotubes on patterned silicon wafers," *Nature*, vol. 395, pp. 878–881, Oct. 1998.

[38] J. Kong, A. M. Cassell, and H. Dai, "Chemical vapor deposition of methane for single-walled carbon nanotubes," *Chemical Physics Letters*, vol. 292, pp. 567 – 574, 1998.

[39] J. Liu, A. G. Rinzler, H. Dai, J. H. Hafner, R. K. Bradley, P. J. Boul, A. Lu, T. Iverson, K. Shelimov, C. B. Huffman, F. Rodriguez-Macias, Y.-S. Shon, T. R. Lee, D. T. Colbert, and R. E. Smalley, "Fullerene pipes," *Science*, vol. 280, no. 5367, pp. 1253–1256, 1998.

[40] H. Dai, "Carbon nanotubes: opportunities and challenges," *Surface Science*, vol. 500, pp. 218 – 241, 2002.

[41] M. Kumar, *Carbon Nanotubes - Synthesis, Characterization, Applications*, ch. Carbon Nanotube Synthesis and Growth Mechanism, pp. 155–158. INTECH, 2011.

[42] S. Sinnott, R. Andrews, D. Qian, A. Rao, Z. Mao, E. Dickey, and F. Derbyshire, "Model of carbon nanotube growth through chemical vapor deposition," *Chemical Physics Letters*, vol. 315, pp. 25 – 30, 1999.

[43] J. H. Hafner, M. J. Bronikowski, B. R. Azamian, P. Nikolaev, A. G. Rinzler, D. T. Colbert, K. A. Smith, and R. E. Smalley, "Catalytic growth of single-wall carbon nanotubes from metal particles," *Chemical Physics Letters*, vol. 296, pp. 195 – 202, 1998.

[44] B. Zheng, C. Lu, G. Gu, A. Makarovski, G. Finkelstein, and J. Liu, "Efficient CVD growth of single-walled carbon nanotubes on surfaces using carbon monoxide precursor," *Nano Letters*, vol. 2, no. 8, pp. 895–898, 2002.

[45] A. M. Cassell, J. A. Raymakers, J. Kong, and H. Dai, "Large scale CVD synthesis of single-walled carbon nanotubes," *The Journal of Physical Chemistry B*, vol. 103, no. 31, pp. 6484–6492, 1999.

[46] K. Hata, D. N. Futaba, K. Mizuno, T. Namai, M. Yumura, and S. Iijima, "Water-assisted highly efficient synthesis of impurity-free single-waited carbon nanotubes," *Science*, vol. 306, pp. 1362–1364, Nov. 2004.

[47] Z. W. Pan, S. S. Xie, B. H. Chang, C. Y. Wang, L. Lu, W. Liu, W. Y. Zhou, W. Z. Li, and L. X. Qian, "Very long carbon nanotubes," *Nature*, vol. 394, pp. 631–632, Aug. 1998.

[48] Q. Yang, S. Bai, T. Fournier, F. Li, G. Wang, H. Cheng, and J. Bai, "Direct growth of macroscopic fibers composed of large diameter SWNTs by CVD," *Chemical Physics Letters*, vol. 370, pp. 274 – 279, 2003.

[49] L. Huang, B. White, M. Y. Sfeir, M. Huang, H. X. Huang, S. Wind, J. Hone, and S. O'Brien, "Cobalt ultrathin film catalyzed ethanol chemical vapor deposition of single-walled carbon nanotubes," *The Journal of Physical Chemistry B*, vol. 110, no. 23, pp. 11103–11109, 2006.

[50] S. Maruyama, R. Kojima, Y. Miyauchi, S. Chiashi, and M. Kohno, "Low-temperature synthesis of high-purity single-walled carbon nanotubes from alcohol," *Chemical Physics Letters*, vol. 360, pp. 229–234, July 2002.

[51] Y. Murakami, Y. Miyauchi, S. Chiashi, and S. Maruyama, "Direct synthesis of high-quality single-walled carbon nanotubes on silicon and quartz substrates," *Chemical Physics Letters*, vol. 377, pp. 49–54, Aug. 2003.

[52] P. Ayala, W. Plank, A. Gruneis, E. I. Kauppinen, M. H. Rummeli, H. Kuzmany, and T. Pichler, "A one step approach to b-doped single-walled carbon nanotubes," *J. Mater. Chem.*, vol. 18, pp. 5676–5681, 2008.

[53] C. L. Cheung, A. Kurtz, H. Park, and C. M. Lieber, "Diameter-controlled synthesis of carbon nanotubes," *The Journal of Physical Chemistry B*, vol. 106, no. 10, pp. 2429–2433, 2002.

[54] T. Saito, S. Ohshima, T. Okazaki, S. Ohmori, M. Yumura, and S. Iijima, "Selective diameter control of single-walled carbon nanotubes in the gas-phase synthesis," *J. Nanosci. Nanotech.*, vol. 8, pp. 6153–6157, Nov. 2008.

[55] A. Moisala, A. G. Nasibulin, and E. I. Kauppinen, "The role of metal nanoparticles in the catalytic production of single-walled carbon nanotubes: a review," *Journal of Physics: Condensed Matter*, vol. 15, no. 42, p. S3011, 2003.

[56] M. H. Hu, Y. Murakami, M. Ogura, S. Maruyama, and T. Okubo, "Morphology and chemical state of co-mo catalysts for growth of single-walled carbon nanotubes vertically aligned on quartz substrates," *Journal of Catalysis*, vol. 225, pp. 230–239, July 2004.

[57] C. N. R. Rao and A. Govindaraj, "Carbon nanotubes from organometallic precursors," *Accounts of Chemical Research*, vol. 35, no. 12, pp. 998–1007, 2002.

[58] H. Cui, G. Eres, J. Howe, A. Puretkzy, M. Varela, D. Geohegan, and D. Lowndes, "Growth behavior of carbon nanotubes on multilayered metal catalyst film in chemical vapor deposition," *Chemical Physics Letters*, vol. 374, pp. 222 – 228, 2003.

[59] Y. J. Yoon, J. C. Bae, H. K. Baik, S. Cho, S.-J. Lee, K. M. Song, and N. S. Myung, "Growth control of single and multi-walled carbon nanotubes by thin film catalyst," *Chemical Physics Letters*, vol. 366, pp. 109 – 114, 2002.

[60] W. De Zhang, Y. Wen, S. M. Liu, W. C. Tjiu, G. Q. Xu, and L. M. Gan, "Synthesis of vertically aligned carbon nanotubes on metal deposited quartz plates," *Carbon*, vol. 40, no. 11, pp. 1981–1989, 2002.

[61] D. B. Geohegan, A. A. Puretzky, I. N. Ivanov, S. Jesse, G. Eres, and J. Y. Howe, "In situ growth rate measurements and length control during chemical vapor deposition of vertically aligned multiwall carbon nanotubes," *Applied Physics Letters*, vol. 83, pp. 1851–1853, Sept. 2003.

[62] N. Chopra, P. D. Kichambare, R. Andrews, and B. J. Hinds, "Control of multi-walled carbon nanotube diameter by selective growth on the exposed edge of a thin film multilayer structure," *Nano Letters*, vol. 2, pp. 1177–1181, Oct. 2002.

[63] K. Y. Lee, S. I. Honda, M. Katayama, T. Miyake, K. Himuro, K. Oura, J. G. Lee, H. Mori, and T. Hirao, "Vertically aligned growth of carbon nanotubes with long length and high density," *Journal of Vacuum Science & Technology B*, vol. 23, pp. 1450–1453, July 2005.

[64] J. W. Liu, X. J. Li, A. Schrand, T. Ohashi, and L. M. Dai, "Controlled syntheses of aligned multi-walled carbon nanotubes: Catalyst particle size and density control via layer-by-layer assembling," *Chemistry of Materials*, vol. 17, pp. 6599–6604, Dec. 2005.

[65] C. Liu, A. J. Cheng, M. Clark, and Y. Tzeng, "Effects of interfacial layers on thermal chemical vapour deposition of carbon nanotubes using iron catalyst," *Diamond and Related Materials*, vol. 14, pp. 835–840, Mar. 2005.

[66] T. Komukai, K. Aoki, H. Furuta, M. Furuta, K. Oura, and T. Hirao, "Density control of carbon nanotubes through the thickness of Fe/Al multilayer catalyst," *Japanese Journal of Applied Physics Part 1-regular Papers Brief Communications & Review Papers*, vol. 45, pp. 6043–6045, July 2006.

[67] J. W. Ward, B. Q. Wei, and P. M. Ajayan, "Substrate effects on the growth of carbon nanotubes by thermal decomposition of methane," *Chemical Physics Letters*, vol. 376, pp. 717–725, July 2003.

[68] H. C. Cheng, K. C. Lin, H. C. Tai, C. P. Juan, R. L. Lai, Y. S. Liu, H. W. Chen, and Y. Y. Syu, "Growth and field emission characteristics of carbon nanotubes using Co/Cr/Al multilayer catalyst," *Japanese Journal of Applied Physics Part 1-regular Papers Brief Communications & Review Papers*, vol. 46, pp. 4359–4363, July 2007.

[69] Y. Murakami, S. Chiashi, Y. Miyauchi, M. H. Hu, M. Ogura, T. Okubo, and S. Maruyama, "Growth of vertically aligned single-walled carbon nanotube films on quartz substrates and their optical anisotropy," *Chemical Physics Letters*, vol. 385, pp. 298–303, Feb. 2004.

[70] S. Maruyama, E. Einarsson, Y. Murakami, and T. Edamura, "Growth process of vertically aligned single-walled carbon nanotubes," *Chemical Physics Letters*, vol. 403, pp. 320–323, Feb. 2005.

[71] Y. Mizutani, K. Sato, T. Maruyama, and S. Naritsuka, "SWNT growth on Al2Ox/Co/Al2Ox multilayer catalyst using alcohol gas source method in high vacuum," *Journal of Crystal Growth*, vol. 318, pp. 1101–1104, Mar. 2011.

[72] C. Fisher, Z. J. Han, I. Levchenko, and K. Ostrikov, "Control of dense carbon nanotube arrays via hierarchical multilayer catalyst," *Applied Physics Letters*, vol. 99, p. 143104, Oct. 2011.

[73] M. Cantoro, S. Hofmann, S. Pisana, V. Scardaci, A. Parvez, C. Ducati, A. C. Ferrari, A. M. Blackburn, K. Y. Wang, and J. Robertson, "Catalytic chemical vapor deposition of single-wall carbon nanotubes at low temperatures," *Nano Letters*, vol. 6, pp. 1107–1112, June 2006.

[74] P. Ayala, A. Grueneis, T. Gemming, B. Buchner, M. H. Rummeli, D. Grimm, J. Schumann, R. Kaltofen, F. L. Freire, H. D. Fonseca, and T. Pichler, "Influence of the catalyst hydrogen pretreatment on the growth of vertically aligned nitrogen-doped carbon nanotubes," *Chemistry of Materials*, vol. 19, pp. 6131–6137, Dec. 2007.

[75] M. Kumar and Y. Ando, "Chemical vapor deposition of carbon nanotubes: A review on growth mechanism and mass production," *Journal of Nanoscience and Nanotechnology*, vol. 10, no. 6, pp. 3739–3758, 2010.

[76] S. Helveg, C. Lopez-Cartes, J. Sehested, P. L. Hansen, B. S. Clausen, J. R. Rostrup-Nielsen, F. Abild-Pedersen, and J. K. Norskov, "Atomic-scale imaging of carbon nanofibre growth," *Nature*, vol. 427, no. 6973, pp. 426–429, 2004.

[77] S. Hofmann, R. Sharma, C. Ducati, G. Du, C. Mattevi, C. Cepek, M. Cantoro, S. Pisana, A. Parvez, F. Cervantes-Sodi, A. C. Ferrari, R. Dunin-Borkowski, S. Lizzit, L. Petaccia, A. Goldoni, and J. Robertson, "In situ observations of catalyst dynamics during surface-bound carbon nanotube nucleation," *Nano Letters*, vol. 7, no. 3, pp. 602–608, 2007.

[78] J. Gavillet, A. Loiseau, C. Journet, F. Willaime, F. Ducastelle, and J.-C. Charlier, "Root-growth mechanism for single-wall carbon nanotubes," *Phys. Rev. Lett.*, vol. 87, p. 275504, Dec 2001.

[79] Y. Li, W. Kim, Y. Zhang, M. Rolandi, D. Wang, and H. Dai, "Growth of single-walled carbon nanotubes from discrete catalytic nanoparticles of various sizes," *The Journal of Physical Chemistry B*, vol. 105, no. 46, pp. 11424–11431, 2001.

[80] J.-Y. Raty, F. m. c. Gygi, and G. Galli, "Growth of carbon nanotubes on metal nanoparticles: A microscopic mechanism from *Ab Initio* molecular dynamics simulations," *Phys. Rev. Lett.*, vol. 95, p. 096103, Aug 2005.

[81] A. Rinzler, J. Liu, H. Dai, P. Nikolaev, C. Huffman, F. Rodríguez-Macías, P. Boul, A. Lu, D. Heymann, D. Colbert, R. Lee, J. Fischer, A. Rao, P. Eklund, and R. Smalley, "Large-scale purification of single-wall carbon nanotubes: process, product, and characterization," *Applied Physics A*, vol. 67, no. 1, pp. 29–37, 1998.

[82] K. Hernadi, A. Fonseca, J. Nagy, D. Bernaerts, J. Riga, and A. Lucas, "Catalytic synthesis and purification of carbon nanotubes," *Synthetic Metals*, vol. 77, pp. 31 – 34, 1996.

[83] I. W. Chiang, B. E. Brinson, R. E. Smalley, J. L. Margrave, and R. H. Hauge, "Purification and characterization of single-wall carbon nanotubes," *The Journal of Physical Chemistry B*, vol. 105, no. 6, pp. 1157–1161, 2001.

[84] V. Georgakilas, D. Voulgaris, E. Vazquez, M. Prato, D. M. Guldi, A. Kukovecz, and H. Kuzmany, "Purification of hipco carbon nanotubes via organic functionalization," *Journal of the American Chemical Society*, vol. 124, pp. 14318–14319, Dec. 2002.

[85] M. Arnold, A. Green, J. Hulvat, S. Stupp, and M. Hersam, "Sorting carbon nanotubes by electronic structure using density differentiation," *Nature Nanotechnology*, vol. 1, pp. 60–65, 2006.

[86] P. Lukaszczuk, E. Borowiak-PalénĎ, M. H. Rümmeli, and R. J. Kalenczuk, "Gel-based separation of single-walled carbon nanotubes for metallic and semiconducting fractions," *Materials Research Bulletin*, vol. 46, no. 10, pp. 1535 – 1539, 2011.

[87] H. Liu, D. Nishide, T. Tanaka, and H. Kataura, "Large-scale single-chirality separation of single-wall carbon nanotubes by simple gel chromatography," *Nat Commun*, vol. 2, pp. 309–, May 2011.

[88] N. Perea-Lopez, B. Rebollo-Plata, J. A. Briones-Leon, A. Morelos-Gomez, D. Hernandez-Cruz, G. A. Hirata, V. Meunier, A. R. Botello-Mendez, J.-C. Charlier, B. Maruyama, E. Munoz-Sandoval, F. Lopez-Urias, M. Terrones, and H. Terrones, "Millimeter-long carbon nanotubes: Outstanding electron-emitting sources," *ACS Nano*, vol. 5, no. 6, pp. 5072–5077, 2011.

[89] M. Ishida, H. Hongo, F. Nihey, and Y. Ochiai, "Diameter-controlled carbon nanotubes grown from lithographically defined nanoparticles," *Japanese Journal of Applied Physics*, vol. 43, pp. L1356–L1358, 2004.

[90] F. Rohmund, R.-E. Morjan, G. Ledoux, F. Huisken, and R. Alexandrescu, "Carbon nanotube films grown by laser-assisted chemical vapor deposition," *Journal of Vacuum Science & Technology B: Microelectronics and Nanometer Structures*, vol. 20, no. 3, pp. 802–811, 2002.

[91] M. C. D. Bock, R. Denk, C. T. Wirth, P. Goldberg-Oppenheimer, S. Hofmann, and J. J. Baumberg, "Optical feedback mechanisms in laser induced growth of carbon nanotube forests," *Applied Physics Letters*, vol. 100, no. 1, p. 013112, 2012.

[92] Y. van de Burgt, Y. Bellouard, R. Mandamparambil, M. Haluska, and A. Dietzel, "Closed-loop control of laser assisted chemical vapor deposition growth of carbon nanotubes," *Journal of Applied Physics*, vol. 112, no. 3, p. 034904, 2012.

[93] K. Kasuya, K. Nagato, Y. Jin, H. Morii, T. Ooi, and M. Nakao, "Rapid and localized synthesis of single-walled carbon nanotubes on flat surface by laser-assisted chemical vapor deposition," *Japanese Journal of Applied Physics*, vol. 46, no. 14, pp. L333–L335, 2007.

[94] J. Park, M. Jeong, and S. Jeong, "Direct writing of carbon nanotube patterns by laser-induced chemical vapor deposition on a transparent substrate," *Applied Surface Science*, vol. 255, no. 8, pp. 4526 – 4530, 2009.

[95] Y. S. Zhou, W. Xiong, J. Park, M. Qian, M. Mahjouri-Samani, Y. Gao, L. Jiang, and Y. Lu, "Laser-assisted nanofabrication of carbon nanostructures," *Journal of Laser Applications*, vol. 24, p. 042007, 2012.

[96] C. Dekker, "Carbon nanotubes as molecular quantum wires," *Physics Today*, vol. 52, no. 5, pp. 22–28, 1999.

[97] A. Hirsch, "Functionalization of single-walled carbon nanotubes," *Angewandte Chemie International Edition*, vol. 41, no. 11, pp. 1853–1859, 2002.

[98] Y.-P. Sun, K. Fu, Y. Lin, and W. Huang, "Functionalized carbon nanotubes: Properties and applications," *Accounts of Chemical Research*, vol. 35, no. 12, pp. 1096–1104, 2002.

[99] A. Kukovecz, T. Pichler, R. Pfeiffer, C. Kramberger, and H. Kuzmany, "Diameter selective doping of single wall carbon nanotubes," *Physical Chemistry Chemical Physics*, vol. 5, no. 3, pp. 582–587, 2003.

[100] H. Kuzmany, A. Kukovecz, F. Simon, M. Holzweber, C. Kramberger, and T. Pichler, "Functionalization of carbon nanotubes," *Synthetic Metals*, vol. 141, pp. 113 – 122, 2004.

[101] K. Balasubramanian and M. Burghard, "Chemically functionalized carbon nanotubes," *Small*, vol. 1, no. 2, pp. 180–192, 2005.

[102] C. A. Ávila Orta, P. González-Morones, C. J. Espinoza-González, J. G. Martínez-Colunga, M. G. Neira-Velázquez, A. Sáenz-Galindo, and L. I. López-López, "Toward greener chemistry methods for preparation of hybrid polymer materials based on carbon nanotubes," in *Syntheses and Applications of Carbon Nanotubes and Their Composites* (S. Suzuki, ed.), ch. 8, pp. 167–192, InTech - Open Access, 2013.

[103] C. Dwyer, M. Guthold, M. Falvo, S. Washburn, R. Superfine, and D. Erie, "DNA - functionalized single-walled carbon nanotubes," *Nanotechnology*, vol. 13, no. 5, p. 601, 2002.

[104] T. Ramanathan, F. T. Fisher, R. S. Ruoff, and L. C. Brinson, "Amino-functionalized carbon nanotubes for binding to polymers and biological systems," *Chemistry of Materials*, vol. 17, no. 6, pp. 1290–1295, 2005.

[105] S. Daniel, T. P. Rao, K. S. Rao, S. U. Rani, G. Naidu, H.-Y. Lee, and T. Kawai, "A review of DNA functionalized/grafted carbon nanotubes and their characterization," *Sensors and Actuators B: Chemical*, vol. 122, no. 2, pp. 672 – 682, 2007.

[106] L. S. Cahill, Z. Yao, A. Adronov, J. Penner, K. R. Moonoosawmy, P. Kruse, and G. R. Goward, "Polymer-functionalized carbon nanotubes investigated by solid-state nuclear magnetic resonance and scanning tunneling microscopy," *The Journal of Physical Chemistry B*, vol. 108, no. 31, pp. 11412–11418, 2004.

[107] N. G. Sahoo, S. Rana, J. W. Cho, L. Li, and S. H. Chan, "Polymer nanocomposites based on functionalized carbon nanotubes," *Progress in Polymer Science*, vol. 35, no. 7, pp. 837 – 867, 2010.

[108] B. W. Smith, M. Monthioux, and D. E. Luzzi, "Encapsulated C-60 in carbon nanotubes," *Nature*, vol. 396, pp. 323–324, Nov. 1998.

[109] M. Monthioux, "Filling single-wall carbon nanotubes," *Carbon*, vol. 40, no. 10, pp. 1809–1823, 2002.

[110] J. Sloan, S. Friedrichs, R. R. Meyer, A. I. Kirkland, J. L. Hutchison, and M. L. H. Green, "Structural changes induced in nanocrystals of binary compounds confined within single walled carbon nanotubes: a brief review," *Inorg. Chim. Acta*, vol. 330, pp. 1–12, Mar. 2002.

[111] Y. F. Li, T. Kaneko, T. Ogawa, M. Takahashi, and R. Hatakeyama, "Magnetic characterization of Fe-nanoparticles encapsulated single-walled carbonnanotubes," *Chem. Commun.*, no. 3, pp. 254–256, 2006.

[112] L. J. Li, A. N. Khlobystov, J. G. Wiltshire, G. A. D. Briggs, and R. J. Nicholas, "Diameter-selective encapsulation of metallocenes in single-walled carbon nanotubes," *Nat. Mater.*, vol. 4, pp. 481–485, June 2005.

[113] R. Kitaura and H. Shinohara, "Endohedral metallofullerenes and nanopeapods," *Japanese Journal of Applied Physics Part 1-regular Papers Brief Communications & Review Papers*, vol. 46, pp. 881–891, Mar. 2007.

[114] R. Kitaura, H. Okimoto, H. Shinohara, T. Nakamura, and H. Osawa, "Magnetism of the endohedral metallofullerenes M@C(82) (M=Gd,Dy) and the corresponding nanoscale peapods: Synchrotron soft x-ray magnetic circular dichroism

and density-functional theory calculations," *Phys. Rev. B*, vol. 76, p. 172409, Nov. 2007.

[115] R. Kitaura, D. Ogawa, K. Kobayashi, T. Saito, S. Ohshima, T. Nakamura, H. Yoshikawa, K. Awaga, and H. Shinohara, "High yield synthesis and characterization of the structural and magnetic properties of crystalline ErCl(3) nanowires in single-walled carbon nanotube templates," *Nano Research*, vol. 1, pp. 152–157, Aug. 2008.

[116] Y. Li, T. Kaneko, T. Ogawa, M. Takahashi, and R. Hatakeyama, "Novel properties of single-walled carbon nanotubes with encapsulated magnetic atoms," *Japanese Journal of Applied Physics, Part 1 (Regular Papers, Short Notes & Review Papers)*, vol. 47, no. 4, pp. 2048–55, 2008.

[117] H. Shiozawa, T. Pichler, A. Gruneis, R. Pfeiffer, H. Kuzmany, Z. Liu, K. Suenaga, and H. Kataura, "A catalytic reaction inside a single-walled carbon nanotube," *Advanced Materials*, vol. 20, pp. 1443–1449, Apr. 2008.

[118] H. Shiozawa, T. Pichler, C. Kramberger, M. Rummeli, D. Batchelor, Z. Liu, K. Suenaga, H. Kataura, and S. R. P. Silva, "Screening the missing electron: Nanochemistry in action," *Phys. Rev. Lett.*, vol. 102, p. 046804, Jan. 2009.

[119] M. Koshino, Y. Niimi, E. Nakamura, H. Kataura, T. Okazaki, K. Suenaga, and S. Iijima, "Analysis of the reactivity and selectivity of fullerene dimerization reactions at the atomic level," *Nat. Chem.*, vol. 2, pp. 117–124, Feb. 2010.

[120] H. Shiozawa, C. Kramberger, R. Pfeiffer, H. Kuzmany, T. Pichler, Z. Liu, K. Suenaga, H. Kataura, and S. R. P. Silva, "Catalyst and chirality dependent growth of carbon nanotubes determined through nano-test tube chemistry," *Advanced Materials*, vol. 22, p. 3685, Sept. 2010.

[121] F. X. Geng and H. T. Cong, "Fe-filled carbon nanotube array with high coercivity," *Physica B-condensed Matter*, vol. 382, pp. 300–304, June 2006.

[122] A. Vyalikh, A. U. B. Wolter, S. Dampel, D. Haase, M. Ritschel, A. Leonhardt, H. J. Grafe, A. Taylor, K. Kramer, B. Buchner, and R. Klingeler, "A carbon-wrapped nanoscaled thermometer for temperature control in biological environments," *Nanomedicine*, vol. 3, pp. 321–327, June 2008.

[123] H. Shiozawa, C. E. Giusca, S. R. P. Silva, H. Kataura, and T. Pichler, "Capillary filling of single-walled carbon nanotubes with ferrocene in an organic solvent," *Physica Status Solidi B-basic Solid State Physics*, vol. 245, pp. 1983–1985, Oct. 2008.

[124] H. Shiozawa, T. Pichler, C. Kramberger, A. Gruneis, M. Knupfer, B. Buchner, V. Zolyomi, J. Koltai, J. Kurti, D. Batchelor, and H. Kataura, "Fine tuning the charge transfer in carbon nanotubes via the interconversion of encapsulated molecules," *Physical Review B*, vol. 77, p. 153402, Apr. 2008.

[125] R. Pfeiffer, T. Pichler, Y. A. Kim, and H. Kuzmany, "Double-wall carbon nanotubes," *Carbon Nanotubes: Advanced Topics In the Synthesis, Structure, Properties and Applications*, vol. 111, pp. 495–530, 2008.

[126] S. Bandow, M. Takizawa, K. Hirahara, M. Yudasaka, and S. Iijima, "Raman scattering study of double-wall carbon nanotubes derived from the chains of fullerenes in single-wall carbon nanotubes," *Chem. Phys. Lett.*, vol. 337, no. 1-3, pp. 48 – 54, 2001.

[127] F. Simon, A. Kukovecz, C. Kramberger, R. Pfeiffer, F. Hasi, H. Kuzmany, and H. Kataura, "Diameter selective reaction processes of single-wall carbon nanotubes," *Phys. Rev. B*, vol. 71, p. 165439, Apr 2005.

[128] L. H. Guan, Z. J. Shi, M. X. Li, and Z. N. Gu, "Ferrocene-filled single-walled carbon nanotubes," *Carbon*, vol. 43, pp. 2780–2785, Nov. 2005.

[129] W. Plank, H. Kuzmany, R. Pfeiffer, T. Saito, and S. Iijima, "Raman scattering from ferrocene encapsulated in narrow diameter carbon nanotubes," *Phys. Status Solidi B*, vol. 246, no. 11-12, pp. 2724–2727, 2009.

[130] C. Kramberger, A. Waske, K. Biedermann, T. Pichler, T. Gemming, B. Buchner, and H. Kataura, "Tailoring carbon nanostructures via temperature and laser irradiation," *Chem. Phys. Lett.*, vol. 407, pp. 254–259, May 2005.

[131] H. Ajiki and T. Ando, "Magnetic properties of carbon nanotubes," *Journal of the Physical Society of Japan*, vol. 62, pp. 2470–2480, 1993.

[132] J. Heremans, C. H. Olk, and D. T. Morelli, "Magnetic susceptibility of carbon structures," *Phys. Rev. B*, vol. 49, pp. 15122–15125, 1994.

[133] A. P. Ramirez, R. C. Haddon, O. Zhou, R. M. Fleming, J. Zhang, S. M. McClure, and R. E. Smalley, "Magnetic susceptibility of molecular carbon: Nanotubes and fullerite," *Science*, vol. 265, pp. 84–86, 1994.

[134] J. Kono, R. J. Nicholas, and S. Roche, "High magnetic field phenomena in carbon nanotubes," *Carbon Nanotubes: Advanced Topics In the Synthesis, Structure, Properties and Applications*, vol. 111, pp. 393–421, 2008.

[135] N. Grobert, W. K. Hsu, Y. Q. Zhu, J. P. Hare, H. W. Kroto, D. R. M. Walton, M. Terrones, H. Terrones, P. Redlich, M. Ruhle, R. Escudero, and F. Morales, "Enhanced magnetic coercivities in Fe nanowires," *Applied Physics Letters*, vol. 75, pp. 3363–3365, Nov. 1999.

[136] A. Leonhardt, M. Ritschel, R. Kozhuharova, A. Graff, T. Mühl, R. Huhle, I. Mönch, D. Elefant, and C. Schneider, "Synthesis and properties of filled carbon nanotubes," *Diamond and Related Materials*, vol. 12, pp. 790 – 793, 2003.

[137] C. Müller, S. Hampel, D. Elefant, K. Biedermann, A. Leonhardt, M. Ritschel, and B. Büchner, "Iron filled carbon nanotubes grown on substrates with thin metal layers and their magnetic properties," *Carbon*, vol. 44, no. 9, pp. 1746 – 1753, 2006.

[138] K. Lipert, F. Kretzschmar, M. Ritschel, A. Leonhardt, R. Klingeler, and B. Büchner, "Nonmagnetic carbon nanotubes," *J. Appl. Phys.*, vol. 105, pp. 063906–1–4, 2009.

[139] G. E. Grechnev, V. A. Desnenko, A. V. Fedorchenko, A. S. Panfilov, Y. A. Kolesnichenko, L. Y. Matzui, M. I. Grybova, Y. I. Prylutskyy, U. Ritter, and P. Scharff, "Structure and magnetic properties of multi-walled carbon nanotubes modified with iron," *Low Temperature Physics*, vol. 36, pp. 1086–1090, Dec. 2010.

[140] U. Ritter, P. Scharff, G. E. Grechnev, V. A. Desnenko, A. V. Fedorchenko, A. S. Panfilov, Y. I. Prylutskyy, and Y. A. Kolesnichenko, "Structure and magnetic properties of multi-walled carbon nanotubes modified with cobalt," *Carbon*, vol. 49, pp. 4443–4448, Nov. 2011.

[141] D. Hisada, Y. Fujiwara, H. Sato, M. Jimbo, T. Kobayashi, and K. Hata, "Structure and magnetic properties of FeCo nanoparticles encapsulated in carbon nanotubes grown by microwave plasma enhanced chemical vapor deposition," *Journal of Magnetism and Magnetic Materials*, vol. 323, pp. 3184–3188, Dec. 2011.

[142] B. Bittova, J. P. Vejpravova, M. Kalbac, S. Burianova, A. Mantlikova, S. Danis, and S. Doyle, "Magnetic properties of iron catalyst particles in HiPco single wall carbon nanotubes," *Journal of Physical Chemistry C*, vol. 115, pp. 17303–17309, Sept. 2011.

[143] E. Borowiak-Palen, E. Mendoza, A. Bachmatiuk, M. H. Rummeli, T. Gemming, J. Nogues, V. Skumryev, R. J. Kalenczuk, T. Pichler, and S. R. P. Silva, "Iron filled single-wall carbon nanotubes - a novel ferromagnetic medium," *Chemical Physics Letters*, vol. 421, pp. 129–133, Apr. 2006.

[144] Y.-J. Kang, J. Choi, C.-Y. Moon, and K. J. Chang, "Electronic and magnetic properties of single-wall carbon nanotubes filled with iron atoms," *Phys. Rev. B*, vol. 71, no. 11, pp. 115441–1–7, 2005.

[145] J. Wang, C. Jo, and R. Wu, "Magnetic properties of Fe-5d (Os, Ir, and Pt) nanowires encapsulated in carbon nanotubes," *Applied Physics Letters*, vol. 92, no. 3, pp. 032507–1–3, 2008.

[146] H. Shinohara, "Endohedral metallofullerenes," *Reports On Progress In Physics*, vol. 63, pp. 843–892, June 2000.

[147] P. Ayala, R. Kitaura, C. Kramberger, H. Shiozawa, N. Imazu, K. Kobayashi, D. Mowbray, P. Hoffmann, H. Shinohara, and T. Pichler, "A resonant photoemission insight to the electronic structure of Gd nanowires templated in the hollow core of SWCNTs," *Materials Express*, vol. 1, no. 1, pp. 30–35, 2011.

[148] P. Ayala, R. Kitaura, R. Nakanishi, H. Shiozawa, D. Ogawa, P. Hoffmann, H. Shinohara, and T. Pichler, "Templating rare-earth hybridization via ultrahigh vacuum annealing of ErCl(3) nanowires inside carbon nanotubes," *Physical Review B*, vol. 83, p. 085407, Feb. 2011.

[149] H. Kuzmany, "Light scattering spectroscopy," in *Solid-State Spectroscopy*, pp. 183–215, Springer Berlin Heidelberg, 2009.

[150] A. Jorio, E. Kauppinen, and A. Hassanien, "Carbon-nanotube metrology," in *Carbon Nanotubes*, vol. 111, pp. 63–100, Springer Berlin Heidelberg, 2008.

[151] M. Dresselhaus, G. Dresselhaus, R. Saito, and A. Jorio, "Raman spectroscopy of carbon nanotubes," *Physics Reports*, vol. 409, no. 2, pp. 47 – 99, 2005.

[152] C. Thomsen and S. Reich, "Double resonant raman scattering in graphite," *Phys. Rev. Lett.*, vol. 85, pp. 5214–5217, Dec 2000.

[153] P. T. Araujo, S. K. Doorn, S. Kilina, S. Tretiak, E. Einarsson, S. Maruyama, H. Chacham, M. A. Pimenta, and A. Jorio, "Third and fourth optical transitions in semiconducting carbon nanotubes," *Phys. Rev. Lett.*, vol. 98, p. 067401, Feb 2007.

[154] H. Kataura, Y. Kumazawa, Y. Maniwa, I. Umezu, S. Suzuki, Y. Ohtsuka, and Y. Achiba, "Optical properties of single-wall carbon nanotubes," *Synthetic Metals*, vol. 103, pp. 2555–2558, June 1999.

[155] H. Wende and C. Antoniak, "X-ray magnetic dichroism," in *Magnetism and Synchrotron Radiation*, vol. 133, pp. 145–167, Springer Berlin Heidelberg, 2010.

[156] W. Grange, J. P. Kappler, and M. Maret, "Magnetocrystalline anisotropy of transition metals: Recent achievements in x-ray absorption spectroscopy," in *Magnetism: Molecules to Materials I*, pp. 211–234, Wiley-VCH Verlag GmbH & Co. KGaA, 2003.

[157] J. L. Erskine and E. A. Stern, "Calculation of the M_{23} magneto-optical absorption spectrum of ferromagnetic nickel," *Phys. Rev. B*, vol. 12, pp. 5016–5024, Dec 1975.

[158] G. Schütz, W. Wagner, W. Wilhelm, P. Kienle, R. Zeller, R. Frahm, and G. Materlik, "Absorption of circularly polarized x rays in iron," *Phys. Rev. Lett.*, vol. 58, pp. 737–740, Feb 1987.

[159] B. T. Thole, P. Carra, F. Sette, and G. van der Laan, "X-ray circular-dichroism as a probe of orbital magnetization," *Phys. Rev. Lett.*, vol. 68, pp. 1943–1946, Mar. 1992.

[160] P. Carra, P., B. T. Thole, B. T.Hole, M. Altarelli, and X. D. Wang, "X-ray circular-dichroism and local magnetic-fields," *Phys. Rev. Lett.*, vol. 70, pp. 694–697, Feb. 1993.

[161] G. Y. Guo, H. Ebert, W. M. Temmerman, and P. J. Durham, "First-principles calculation of magnetic x-ray dichroism in Fe and Co multilayers," *Phys. Rev. B*, vol. 50, pp. 3861–3868, Aug 1994.

[162] M. Komelj, C. Ederer, J. W. Davenport, and M. Fähnle, "From the bulk to monatomic wires: an *ab initio* study of magnetism in Co systems with various dimensionality," *Phys. Rev. B*, vol. 66, p. 140407, Oct 2002.

[163] S. Peredkov, M. Neeb, W. Eberhardt, J. Meyer, M. Tombers, H. Kampschulte, and G. Niedner-Schatteburg, "Spin and orbital magnetic moments of free nanoparticles," *Phys. Rev. Lett.*, vol. 107, p. 233401, Nov 2011.

[164] C. T. Chen, Y. U. Idzerda, H. J. Lin, N. V. Smith, G. Meigs, E. Chaban, G. H. Ho, E. Pellegrin, and F. Sette, "Experimental confirmation of the x-ray magnetic circular-dichroism sum-rules for iron and cobalt," *Phys. Rev. Lett.*, vol. 75, pp. 152–155, July 1995.

[165] A. Barron, "Theory of a superconducting quantum interference device (squid)," in *Nanomaterials and Nanotechnology*, Connexions Web site: http://cnx.org/content/col10700/1.12/, 2013.

[166] K. Yanagi, H. Udoguchi, S. Sagitani, Y. Oshima, T. Takenobu, H. Kataura, T. Ishida, K. Matsuda, and Y. Maniwa, "Transport mechanisms in metallic and semiconducting single-wall carbon nanotube networks," *Acs Nano*, vol. 4, pp. 4027–4032, July 2010.

[167] U. Holzwarth and N. Gibson, "The scherrer equation versus the 'debye-scherrer equation'," *Nature Nanotechnology*, vol. 6, pp. 534–534, Sept. 2011.

[168] M. Berd, P. Puech, A. Righi, A. Benfdila, and M. Monthioux, "Resonant laser-induced formation of double-walled carbon nanotubes from peapods under ambient conditions," *Small*, vol. 8, no. 13, pp. 2045–2052, 2012.

[169] Y. van de Burgt, Y. Bellouard, R. Mandamparambil, M. Haluska, and A. Dietzel, "Closed-loop control of laser assisted chemical vapor deposition growth of carbon nanotubes," *Journal of Applied Physics*, vol. 112, p. 034904, 2012.

[170] M. Sauer, H. Shiozawa, P. Ayala, G. Ruiz-Soria, X. Liu, A. Chernov, S. Krause, K. Yanagi, H. Kataura, and T. Pichler, "Internal charge transfer in metallicity sorted ferrocene filled carbon nanotube hybrids," *Carbon*, vol. 59, no. 0, pp. 237 – 245, 2013.

[171] A. Hitchcock, A. Wen, and E. Rühl, "Transition metal 2p excitaton of organometallic compounds studied by electron energy loss spectroscopy," *Chem. Phys.*, vol. 147, pp. 51–63, Oct. 1990.

[172] J. T. Lau, A. Fohlisch, R. Nietubyc, M. Reif, and W. Wurth, "Size-dependent magnetism of deposited small iron clusters studied by x-ray magnetic circular dichroism," *Phys. Rev. Lett.*, vol. 89, no. 5, pp. 057201/1–4, 2002.

[173] E. Duman, M. Acet, E. F. Wassermann, J. P. Itié, F. Baudelet, O. Mathon, and S. Pascarelli, "Magnetic instabilities in Fe_3C cementite particles observed with Fe k-edge x-ray circular dichroism under pressure," *Phys. Rev. Lett.*, vol. 94, p. 075502, Feb 2005.

[174] M. Niemeyer, K. Hirsch, V. Zamudio-Bayer, A. Langenberg, M. Vogel, M. Kossick, C. Ebrecht, K. Egashira, A. Terasaki, T. Moller, B. V. Issendorff, and J. T. Lau, "Spin coupling and orbital angular momentum quenching in free iron clusters," *Phys. Rev. Lett.*, vol. 108, p. 057201, Jan. 2012.

[175] Y. Maniwa, R. Fujiwara, H. Kira, H. Tou, H. Kataura, S. Suzuki, Y. Achiba, E. Nishibori, M. Takata, M. Sakata, A. Fujiwara, and H. Suematsu, "Thermal expansion of single-walled carbon nanotube (swnt) bundles: X-ray diffraction studies," *Phys. Rev. B*, vol. 64, p. 241402, Nov 2001.

[176] H. A. Mook, "Magnetic moment distribution of nickel metal," *Phys. Rev.*, vol. 148, pp. 495–501, Aug 1966.

Juan Antonio Briones León

Education

2010–Present	**PhD in Physics**, University of Vienna, Austria. "Magnetism in 1D metallic clusters grown inside single-walled carbon nanotubes" Advisor: Prof. Mag. Dr. Thomas Pichler
2007–2009	**M. Adv. Tech. in Mechatronics**, CICATA-IPN, Querétaro, Mexico. "Design, Analysis and Assembly of a Translational Parallel Robot" Advisor: Dr. Eduardo Castillo Castaeda
1999–2004	**BSc in Instrumentation and Control**, University of Querétaro, Mexico.

Professional Experience

2010–Present	**Research Assistant**, Faculty of Physics, University of Vienna, Austria.
2009–2010	**Research Assistant**, IPICYT, San Luis Potosi, Mexico.
2005–2007	**Engineering Manager**, ERAT S. A. de C. V., Querétaro, Mexico.
2003–2004	**Intern Researcher**, CIATEQ, Querétaro, Mexico.
1998–2003	**Maintenance and Software Development**, AISC S. A. de C. V., Querétaro, Mexico.

Teaching

Summer 2013	**Solid State Physics Laboratory - Advanced Materials**, University of Vienna, Austria.
Summer 2013	**Physics IV - Exercises**, University of Vienna, Austria.
Winter 2012	**Solid State Physics Laboratory - Advanced Materials**, University of Vienna, Austria.
Winter 2012	**Solid State Physics I - Exercises**, University of Vienna, Austria.
Summer 2012	**Solid State Physics Laboratory - Advanced Materials**, University of Vienna, Austria.
Summer 2011	**Physics IV - Exercises**, University of Vienna, Austria.

Professional Skills

Software:	Programming languages: C, C++, Visual Basic, Visual C++, Matlab.
	3D design: Autocad, Solidworks. Latex, Origin, Mathematica, LabVIEW.
Physics techniques:	Synthesis of nanostructures: Chemical vapor deposition (CVD), laser-assisted CVD.
	Electron Microscopy: Scanning electron microscopy (SEM) and transmission electron microscopy. (TEM)
	Spectroscopy: Raman, X-ray absorption (XAS) and X-ray circular dichroism (XMCD).
	PLCs, Ultra-high vacuum systems, synchrotron based spectroscopy techniques, functionalization of nanostructures, magnetic (SQUID) and field emission measurements.
Lenguages:	Spanish(Native), English (fluent), German(basic).

Honors and Awards

2009	Graduated with honors, CICATA, Querétaro, Mexico.
2009	Best Postgraduate Academic Performance Award, IPN, Mexico.

Research Grants

2007–2009	Postgraduate Scholarship, CONACYT, Mexico.
2008	Scholarship extension to research abroad (Cassino, It), CONACYT, Mexico.

Presentations and posters

2012	IWEPNM 2012, Poster: X-ray absorption and magnetic circular dichorism of ferrocene filled SWCNT, Kirchberg, Austria.
	SIWAN5 , Poster: Magnetic circular dichroism as probe of local magnetic moments in 1d iron-carbon nanotube hybrids, Szeged, Hungary.
2011	IWEPNM 2011, Poster: Nanochemical reactions by laser annealing of ferrocene filled SWCNT, Kirchberg, Austria.
2009	CERMA Congress, Talk: Position and force control of the CAPAMAN 2 Bis parallel robot for drilling tasks, Cuernavaca, Mexico.

Publications

2013 Antonio Briones-Leon, Paola Ayala, Xianjie Liu, Kazuhiro Yanagi, Eugen Weschke, Michael Eisterer, Hua Jiang, Hiromichi Kataura, Thomas Pichler, and Hidetsugu Shiozawa. Orbital and spin magnetic moments of transforming one-dimensional iron inside metallic and semiconducting carbon nanotubes. *Phys. Rev. B*, 87:195435, May 2013

2012 Antonio Briones-Leon, Xianjie Liu, Paola Ayala, Hiromichi Kataura, Kazuhiro Yanagi, Eugen Weschke, Thomas Pichler, and Hidetsugu Shiozawa. Orbital and spin magnetic moments of ferrocene encapsulated in metallicity sorted single-walled carbon nanotubes. *Phys. Status Solidi B*, 249(12):2424–2427, 2012

M. F. Ruiz-Torres, E. Castillo-Castaneda, and A. Briones-Leon. Design and analysis of cicabot: a novel translational parallel manipulator based on two 5-bar mechanisms. *Robotica*, 30:449–456, May 2012

2011 A. Briones-Leon, X. J. Liu, C. Kramberger, T. Saito, and T. Pichler. Nanochemical reactions by laser annealing of ferrocene filled single-walled carbon nanotubes. *Physica Status Solidi B-basic Solid State Physics*, 248(11):2488–2491, November 2011

N. Perea-Lopez, B. Rebollo-Plata, A. Briones-Leon, A. Morelos-Gomez, D. Hernandez-Cruz, G. A. Hirata, V. Meunier, A. R. Botello-Mendez, J. C. Charlier, B. Maruyama, E. Munoz-Sandoval, F. Lopez-Urias, M. Terrones, and H. Terrones. Millimeter-long carbon nanotubes: Outstanding electron-emitting sources. *Acs Nano*, 5(6):5072–5077, June 2011

2009 R. Yanez-Valdez, M. Ruiz-Torres, E. Morales-Sanchez, E. Castillo-Castaneda, and A. Briones-Leon. Resolution of a 3 rrr planar parallel mechanism. *Electromechanical and Systems Engineering*, 15:61–66, 2009

A. Briones-Leon, E. Castillo, G. Carbone, and M. Ceccarelli. Position and force control of the capaman 2 bis parallel robot for drilling tasks. *Cerma: 2009 Electronics Robotics and Automotive Mechanics Conference*, pages 181–186, 2009